QUANTITATIVE MAGNETIZATION TRANSFER IMAGING TECHNIQUES AND APPLICATIONS

By

Xiawei Ou

Dissertation

Submitted to the Faculty of the

Graduate School of Vanderbilt University

in partial fulfillment of the requirements

for the degree of

DOCTOR OF PHILOSOPHY

in

Physics

December, 2007

Nashville, Tennessee

Approved:

Professor Daniel Frank Gochberg

Professor John C. Gore

Professor Adam W. Anderson

Professor Mark D. Does

Professor Norman H. Tolk

TABLE OF CONTENTS:

Page

ACKNOWLEDGEMENTS

I would like to thank my advisor Dr. Daniel Gochberg for his guidance and support. Every part of this dissertation has his contribution and effort. Without his assistance, none of the work presented in the dissertation would have been possible. I am very grateful to his help.

I also want to thank other members of my PhD defense committee: Dr. Adam Anderson, Dr. Mark Does, Dr. John Gore, and Dr. Norman Tolk, for attending the committee meetings and evaluating my dissertation, and for their continuous guidance during my graduate research.

In addition, I would like to thank the research group in Washington University in St. Louis led by Dr. Sheng-Kwei Song, and the research group in Neurology Department of Vanderbilt University led by Dr. Subramaniam Sriram, for their collaboration and their contribution to this dissertation.

Finally, I would like to express my appreciation to Vanderbilt University Department of Physics and Astronomy and Vanderbilt University Institute of Imaging Science for providing excellent education to our graduate students, NIH grants R01 EB001452 and R01 EB000214 for providing funding for my research.

INTRODUCTION

This dissertation discusses magnetization transfer effects in magnetic resonance imaging and the development and applications of quantitative magnetization transfer imaging techniques.

Magnetization transfer effects are caused by the exchange of magnetization between water and macromolecules. Different tissues have different magnetization transfer properties, and therefore a new basis for image contrast is possible. Magnetization transfer effects can be completely quantified by the combination of proton spin relaxation and exchange parameters. These parameters quantify intrinsic physical properties of the imaged sample and provide insights into interested biological properties. The determination of these parameters, which is usually called quantitative magnetization transfer imaging, is not straightforward. Numerical or analytical modeling of magnetization evolution and non-linear fitting of measured data are required to solve for the quantitative parameters.

In spite of the complexity of quantitative magnetization transfer imaging, it is valuable for medical imaging research. The relaxation and exchange parameters provided by quantitative magnetization transfer imaging are found to be sensitive and specific to some central nervous system diseases, and this sensitivity and specificity are not available via conventional magnetic resonance imaging.

Further investigation of magnetization transfer effects, development of quantitative

magnetization transfer imaging techniques, and applications of quantitative magnetization transfer imaging on various animal models, are the three major focuses of my research during the past few years, and they are discussed in detail in this dissertation. Specifically, in this dissertation, Chapter 1 introduces the fundamental theory of MRI and QMT; Chapter 2 introduces several state-of-the-art QMT imaging techniques; Chapter 3 describes a newly discovered magnetization transfer effect in conventional single slice gradient echo imaging and its influence on T_1 measurements and MT parameters quantification; Chapters 4, 5, and 6 discuss applications of QMT imaging to three central nervous system samples designed to elucidate the sensitivity and specificity of QMT imaging to myelin; Chapter 7 concludes this dissertation and outlines possible future directions.

Three first author papers which have been either submitted or prepared are based on the contents of this dissertation. The preliminary results of an ongoing project are also included in this dissertation.

LIST OF TABLES

LIST OF FIGURES

Chapter III

Chapter IV

CHAPTER I

BACKGROUND OF MRI AND QMT

In this chapter, some background information and fundamental knowledge of my research field are introduced.

I will start with a historical introduction of magnetic resonance imaging (MRI), which is one of the most spectacular discoveries in the history of medical imaging. Five Nobel Prizes have been awarded to those who made major contributions to the discovery and development of MRI in the past 60 years. Efforts from numerous scientists have made MRI not only one of the hottest research topics but also one of the most useful clinical tools.

Then I will give an introduction to my specific research area, quantitative magnetization transfer (QMT), with an approach from basic physics theory to modern techniques. Specifically, topics in this chapter include the source of magnetization; the formation of magnetic resonance images; the properties of conventional MRI contrasts (T_1, T_2, and proton density); the recently discovered additional contrasts such as the contrast generated by magnetization transfer (MT); the simple quantity of magnetization transfer ratio (MTR) which quantifies MT; and the set of comprehensive quantitative magnetization transfer (QMT) parameters which fully characterize MT.

1.1 History of MRI

If everybody were comfortable with the word 'nuclear' as much as physicists are, MRI could have been called NMRI, which stands for nuclear magnetic resonance imaging. Nuclear magnetic resonance was discovered almost simultaneously (1946) by two independent groups, led by Professor Felix Bloch and Professor Edward Purcell, respectively (1,2). Bloch's experiments were focused on the precession of nuclear magnetization in a magnetic field which induces an electromotive force in the surrounding radiofrequency coil. Bloch named this phenomenon 'nuclear induction'. Purcell's experiments were focused on the transitions of magnetic nuclei between quantized states in a magnetic field and on resonance absorption of radiofrequency energy. Purcell named this phenomenon 'nuclear magnetic resonance'. (3) Both groups also investigated the T_1 and T_2 relaxation times, and laid the foundations for understanding these physical quantities in their subsequent research. Bloch equations, which described the behavior of nuclear magnetism and were expanded in many different forms, will be referred to many times in this dissertation. Bloch and Purcell were awarded the Nobel Prize for Physics in 1952.

NMR was originally detected by continuous wave irradiation. Professor Erwin Hahn discovered the spin echo in 1950 (4), which was the beginning of the widespread use of pulsed NMR. Professor Richard Ernst developed multiple dimensional NMR spectroscopy technique by using a sequence of high energy pulses for excitation and Fourier Transformation for spectra analysis. Ernst was the winner of Nobel Prize in

Chemistry in 1991 for his contribution to the development of the methodology of high resolution NMR Spectroscopy. His work also laid the foundation for the development of MRI.

In 1971, Professor Raymond Damadian reported that tumors and normal tissues have different NMR Spectra, and he suggested that this difference could be used to diagnose cancer (5). Damadian is credited for describing the concept of whole body NMR scanning and discovering the T_1 and T_2 relaxation differences in tissues which make MRI contrasts feasible. Convinced by the great potential of NMR in disease detection, Professor Paul Lauterbur came up with the idea of using linear magnetic field gradients to spatially localize NMR signal (6). This spatial information allows two-dimensional MRI images to be produced. Lauterbur's discovery set the foundation of broadening the applications of NMR from NMR spectroscopy to MRI imaging. Also in the early 1970's, Sir Peter Mansfield started research of MRI independently (7). Mansfield employed mathematical methods to transform MRI signal into useful images, and developed a MRI protocol named 'echo planar imaging' which reduces the scanning time and makes fast imaging possible (8). Lauterbur and Mansfield won the Nobel Prize in Physiology or Medicine in 2003 for their discoveries concerning MRI.

In the past thirty years, MRI continued on growing with an incredible speed. Scientifically, a number of important developments created new directions and sub-areas of MRI, including the discovery of magnetization transfer contrast by Wolff and Balaban in 1989 (9), the development of functional MRI by Ogawa in the early 1990's (10), the

recognition and wide utilization of diffusion MRI, and so on. Technologically, more sophisticated and powerful MRI scanning systems are available not only for research but also for clinical use, especially characterized by the improvement of magnet manufacturing (from resistive and permanent magnets to superconductive magnets, from less than 0.1 Tesla magnetic field strength to more than 10 Tesla magnetic field strength).

1.2 Fundamentals of MRI

MRI (and NMR) works because we are able to observe the response of protons in magnetic fields. Specifically, we apply a combination of magnetic fields to manipulate the proton orientation, which is measured through the interaction of the proton's magnetic field with coil detectors. Generally, all nuclei possessing a net nuclear spin are NMR active. Hydrogen ^{1}H with a single proton and 1/2 nuclear spin is stable, abundant (such as in water or lipids), and has a high gyromagnetic ratio. Therefore, ^{1}H (proton) is the nucleus studied most in MRI experiments.

Magnetic Moment and Angular Momentum

Magnetic moment is a measure of the strength of a magnetic source. It behaves analogously to an electric dipole (a positive and a negative electric charges separated by a small distance) and therefore is also called a magnetic dipole moment. A simple example of magnetic moment is a current I around a small loop of vector area $\mathbf{ds}$. The magnetic

moment $\boldsymbol{\mu}$ is then $\boldsymbol{\mu} = I\int \mathbf{ds}$.

The angular momentum of an object rotating about some reference point is the measure of the extent to which the object will continue to rotate about that point unless acted upon by an external torque. The Einstein-de Hass effect (magnetic moments induce a rotation) and the Barnett effect (rotation induces magnetic moments) both demonstrate that the magnetic moment $\boldsymbol{\mu}$ is associated with the angular momentum $\mathbf{j}$, with a direct relationship: $\boldsymbol{\mu} = \gamma \mathbf{j}$, in which γ is a constant called gyromagnetic ratio. For example, proton intrinsic angular momentum (often referred as proton spin) can be regarded as a circulating electric current, and is associated with a magnetic moment with gyromagnetic ratio $\gamma = 2.675 \times 10^8 rad/s/T$.

Spin Precession

If a proton spin with a magnetic moment $\boldsymbol{\mu}$ is placed in an external magnetic field $\mathbf{B}$, there will be a torque $\mathbf{G}$ to force the magnetic moment to lie along the magnetic field to minimize energy, and $\mathbf{G} = \boldsymbol{\mu} \times \mathbf{B}$. Since the torque is equal to the rate of change of the angular momentum, $\mathbf{G} = d\mathbf{j}/dt$, the relation between the magnetic moment and the external magnetic field can be written as:

$$\frac{d\boldsymbol{\mu}}{dt} = \gamma \boldsymbol{\mu} \times \mathbf{B} \qquad [1.1]$$

This equation is a simple version of the Bloch Equation. It characterizes the fundamental precession for a proton spin in an external magnetic field, as shown in figure 1.1.

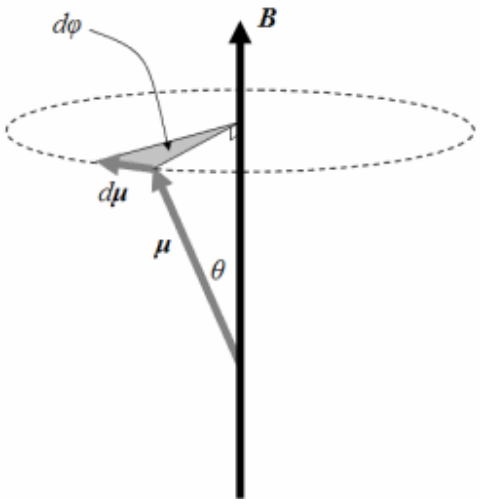

Figure 1.1: The precession of a proton spin with magnetic moment $\boldsymbol{\mu}$ in magnetic field $\mathbf{B}$. θ is the angle between the magnetic moment and the external magnetic field, and $d\varphi$ is the precession angle by the proton spin.

From the geometry in figure 1.1, the magnitude of the change in the magnetic moment is: $|d\boldsymbol{\mu}| = |\boldsymbol{\mu} \sin\theta d\varphi| = \mu \sin\theta d\varphi$. Meanwhile, from Eq. [1.1], $|d\boldsymbol{\mu}| = |\gamma \boldsymbol{\mu} \times \mathbf{B} dt| = \gamma \mu B \sin\theta dt$. Therefore, $\gamma B dt = d\varphi$. This leads to the Larmor precession formula:

$$\omega = d\varphi / dt = \gamma B \qquad [1.2]$$

in which ω is the angular frequency of the proton spin in the magnetic field, and is known as the Larmor frequency.

Spin Rotation

One of the key procedures necessary to create an MRI is manipulation of the proton spins by applying radiofrequency (RF) pulse. RF pulses are additional magnetic fields with

relatively small field strength and oscillating field direction. These magnetic fields are usually applied only for a very short time interval, and are therefore called pulses. Suppose there is a strong and constant external magnetic field $\mathbf{B}_0$. If we apply an additional field $\mathbf{B}_1$, the total magnetic field will be $\mathbf{B}_0 + \mathbf{B}_1$. We can define a rotating reference frame in which the z direction is the direction of $\mathbf{B}_0$ and the xy plane is rotating with frequency ω. If ω is the same as $\omega_0 = \gamma \mathbf{B}_0$, then the $\mathbf{B}_0$ field is inactive in the rotating frame. Meanwhile, if the $\mathbf{B}_1$ field is lying in the xy plane of the rotating frame and also oscillating in the plane with frequency $\omega = \omega_0$ (this frequency is in the radiofrequency range, and is the reason that the $\mathbf{B}_1$ field is also called an 'RF field'), then in the rotating frame the effective magnetic field has a constant magnitude $|\mathbf{B}_1|$ and a constant direction (suppose it is in the x direction): $\mathbf{B}_{eff} = |\mathbf{B}_1|\vec{x}$. In this case, a resonance condition is reached in the rotating reference frame. Even a small $|\mathbf{B}_1|$ (in the order of micro-Tesla) is able to rotate the spin toward the x axis, despite the existing large $\mathbf{B}_0$ field (in the order of Tesla). The angle of the rotation (usually called the flip angle and denoted by α) is determined by the field strength $|\mathbf{B}_1|$ and the time interval of the RF field τ: $\alpha = \gamma |\mathbf{B}_1| \tau$.

Magnetization

Magnetization is defined as the density of the magnetic moments. At equilibrium condition in an external magnetic field $\mathbf{B}_0$, all magnetic moments are either lined up along the field direction or against the field direction. The magnetic moments in the field

direction are slightly more than those in the opposite direction, generating a small amount of net magnetization in the field direction, which is the origin of the signal in MRI experiments. The magnitude of the net magnetization can be derived from the Boltzmann distribution of the protons (which have magnetic moments) in two energy states (corresponding to the magnetic moments along or against the external field direction, respectively). The Boltzmann distribution is: $N_{lower} / N_{higher} = e^{-\Delta E / KT}$, where N is the number of protons in a given state, k is the Boltzmann constant, T is the temperature, and ΔE is the energy difference between the two energy states. The energy difference can be calculated from $\Delta E = \hbar\omega = \hbar\gamma B$. At room temperature in a 1.5 Tesla magnetic field, for every one million protons, the difference in distribution between two energy states is only about 5 protons. Therefore, the measurable net magnetization is relatively small and is related to the magnetic field strength.

T_1 and T_2 Relaxations

At equilibrium in an external magnetic field $\mathbf{B}_0 = B_0 \vec{z}$, there is a slight excess of protons aligned in the z direction, causing a net longitudinal magnetization (M_z). If we apply a 90° RF pulse, the magnetization is flipped to the xy plane, causing a net transverse magnetization (M_{xy}). When the RF pulse is turned off, the magnetization will gradually return to the equilibrium: the longitudinal magnetization will recover to the initial value $M_z = M_0$ by T_1 relaxation, and the transverse magnetization M_{xy} will decay to zero by T_2 relaxation.

The T_1 relaxation is often called spin-lattice relaxation, since it reflects the process by which the spins give the energy they obtained from the RF pulse back to the surrounding lattice, thereby restoring the equilibrium state. It was found that the rate of recovery is proportional to the difference between the equilibrium (M_0) and the current (M_z) longitudinal magnetization, and the proportionality constant is called the T_1 relaxation time:

$$\frac{dM_z}{dt} = \frac{1}{T_1}(M_0 - M_z) \qquad [1.3]$$

T_2 relaxation is often called spin-spin relaxation since it reflects the interaction between spins. In addition to the external magnetic field, spins interact with the fields produced by neighboring spins. This leads to different Larmor precession frequencies for spins, and hence reduces the net transverse magnetization by dephasing. It was found that the dephasing is an exponential decay, which means:

$$\frac{dM_{xy}}{dt} = -\frac{1}{T_2}M_{xy} \qquad [1.4]$$

In which T_2 is the T_2 relaxation time. In practice, there is an additional dephasing of the transverse magnetization caused by the external field inhomogeneities. If we characterize this extra dephasing (which is assumed to be exponential as well) by T_2', then the total transverse magnetization decay can be characterized by an overall T_2^* relaxation time, in which $\frac{1}{T_2^*} = \frac{1}{T_2} + \frac{1}{T_2'}$.

Different tissues have different T_1 and T_2 relaxation times. This property provides the very first and important contrasts in MRI. Both relaxation times maps and weighted images are still widely used in diagnosis and clinic MRI.

Bloch Equation

The evolution of magnetization in the presence of a magnetic field and with the consideration of relaxations is described by the Bloch Equation:

$$\frac{d\mathbf{M}}{dt} = \gamma \mathbf{M} \times \mathbf{B}_{eff} + \frac{1}{T_1}(\mathbf{M}_0 - \mathbf{M}_z) - \frac{1}{T_2}\mathbf{M}_{xy} \qquad [1.5]$$

In which $\mathbf{B}_{eff} = \mathbf{B}_1 + \mathbf{B}_0$. If there is only a constant external magnetic field $\mathbf{B}_0$ in the z direction, the Bloch equation can be rewritten as:

$$\frac{dM_z}{dt} = \frac{M_0 - M_z}{T_1}$$

$$\frac{dM_x}{dt} = \omega_0 M_y - \frac{M_x}{T_2}$$

$$\frac{dM_y}{dt} = -\omega_0 M_x - \frac{M_y}{T_2}$$

Where $\omega_0 = \gamma B_0$ and M_0 is the equilibrium magnetization in the z direction.

Bloch equation [1.5] is the starting point for the magnetization evolution in all MRI experiments. Other terms such as RF excitation field terms, magnetization transfer (which we will talk about later in this chapter) terms, and diffusion terms, can be linearly added to this equation. The resulting magnetization measured in MRI experiments can always be predicted by either analytically solving or numerically integrating Bloch equation.

How to produce an MRI image

An MRI scanner is composed of three major components: the static magnetic field, the RF transmitter and receiver, and the gradients. In general there are three types of magnets: permanent, resistive, and superconducting. Superconducting magnets are the most widely

used type since they provides high strength and very uniform magnetic field $\mathbf{B}_0$. The shape of the magnet is usually cylindrical, with the RF system and the gradients inside. The RF transmitter consists of an RF synthesizer, power amplifier, and transmission coil. They produce an RF field $\mathbf{B}_1$ to manipulate proton spins and generate measurable signal. The RF receiver consists of a receiving coil, pre-amplifier, and signal processing system. They are used to detect the transverse magnetization and provide output signal. Sometimes the transmission coil and the receiving coil are integrated in one RF coil. Gradients are basically made by three orthogonal coils which produce linear spatially varying magnetic fields. Slice selection and spatial encoding are achieved by applying a certain sequence of these orthogonal gradients, so the information for each individual voxel of the sample inside the magnet can be acquired. The measured signal is then reconstructed by a two-dimensional discrete Fourier transform to produce an image for the selected slice.

MRI Contrasts

There are several medical imaging modalities available currently, including MRI, CT, PET, SPECT, fluoroscopy, ultrasound, optical imaging, etc. MRI is known for its high cost, but still, it is becoming one of the most popular medical imaging technologies because of its advantages in many aspects. For example, MRI is not radioactive, unlike many others; MRI provides images with better resolution than most of others do; and most of all, MRI measured signal is based on a combination of biological properties, and

therefore the image contrasts can be altered and enhanced in various ways to detect different features in different parts of the subject. The flexibility, the comprehensiveness, and the great potential of MRI contrasts motivates continued exploration and development of new MRI methods (Of course increasing resolution and decreasing scan time are also some of the driving forces, but they are not emphasized in this dissertation).

It has been mentioned before that T_1 and T_2 relaxation times are two of the properties that provide image contrast. The proton density also varies for different tissues. Therefore proton density weighted images are sometimes used. In addition, many other MRI contrasts have been found to be able to show unique information which is not available via traditional T_1, T_2 or proton density contrasts. For example, the contrast mechanisms used in diffusion MRI, functional MRI, contrast agent MRI, magnetic resonance angiography (MRA), magnetization transfer (MT) imaging, and so on. Among them, magnetization transfer contrast (MTC) is a novel MRI contrast generated by MT effects, which are the focus of this dissertation.

1.3 Introduction of Magnetization Transfer

Off-resonance MT

Magnetization Transfer (MT) is the exchange of magnetization between free water protons and macromolecular protons in biological systems. MT imaging was first implemented by Wolff and Balaban (9). They were attempting to perform a spin transfer experiment by selectively saturating a tissue sample. Instead of a small signal depression,

they found a significant loss of image intensity. This phenomenon can be well explained by a two pool system, as shown in figure 1.2. In a two pool spin-bath system, the protons are either from the free water (free pool) or from the macromolecules (restricted pool). The protons in the restricted pool are strongly coupled to each other, resulting in a very broad absorption lineshape (a wide range of resonance frequency) and a very short T_2, typically in the order of 10 μs. The transverse magnetization from the restricted pool protons is completely dephased before an MRI sequence can acquire any data. Therefore, conventional MRI techniques can only observe signal from the free water pool protons. If an off-resonance RF pulse is applied to saturate the restricted pool (the frequency of the RF pulse is off-resonance to the free pool, but still in the resonance range of the restricted pool), then the thermal equilibrium of this two-pool system is destroyed. The two pools will exchange magnetization. Specifically, the free pool will supply magnetization to the restricted pool to mitigate the loss by saturation. Therefore, although the free pool magnetization is not directly affected by the off-resonance RF pulse, the magnetization transfer effect will cause the free pool to lose magnetization. This is the reason that the measured free water signal is significantly decreased.

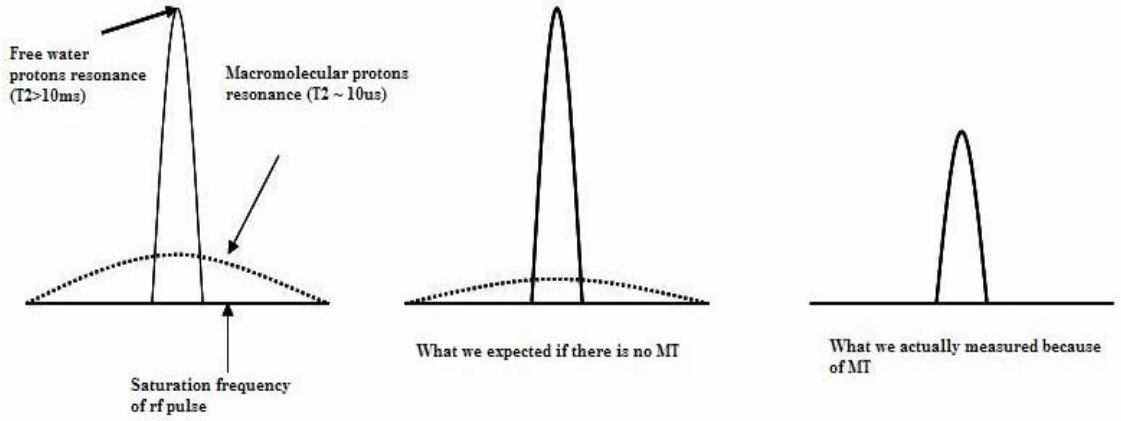

Figure 1.2: MT effect caused by off-resonance RF pulse: the measured free water pool magnetization is significantly decreased because of MT effect.

On-resonance MT

It is well known that MT occurs when applying an off-resonance RF pulse to samples with two or more biological pools. However, it is not well appreciated that MT also occurs when applying an on-resonance RF pulse. In fact, any pulse that affects the two proton pools differently (and nearly every RF pulse does) will induce MT. Off-resonance pulses saturate the restricted pool to a greater extent than the free pool; on-resonance pulses rotate the free pool while having little effect on the restricted pool (when at low power). In Both cases, the equilibrium is broken, and the two pools will exchange magnetization. Figure 1.3 shows that if we apply an on-resonance RF pulse with a relatively low power, the measured free pool signal will be slightly higher than what we expected if assuming there is no MT. Specifically, the restricted pool will supply magnetization to the free pool to mitigate the loss by the on-resonance excitation pulse,

therefore increasing the measurable free pool signal. This signal increase is usually much smaller than the signal decrease in the off-resonance MT case, and is generally ignored. We will show later in this dissertation that this on-resonance MT effect is important in some case. Furthermore, useful information can be obtained if we consider this effect.

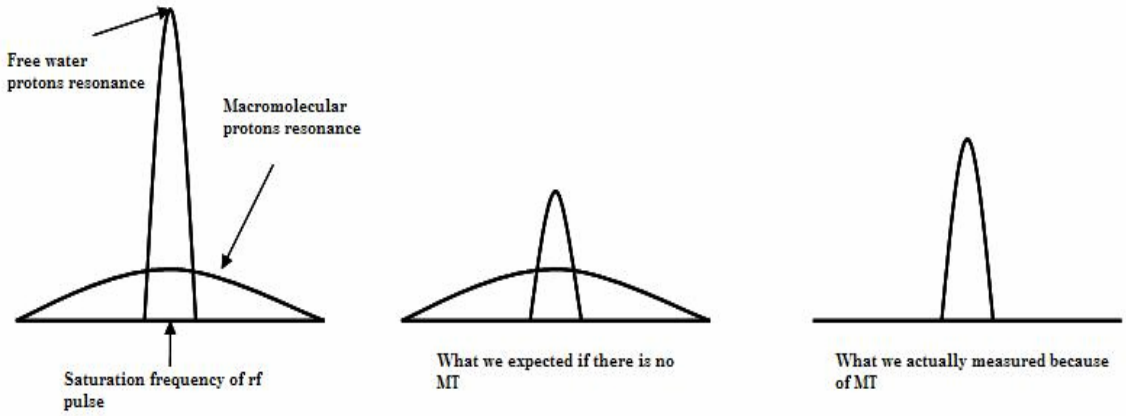

Figure 1.3: MT effect caused by on-resonance RF pulse: the measured free water pool magnetization is slightly increased because of an MT effect.

Magnetization transfer ratio (MTR)

The MTR is a quantity that describes the extent of MT. MTR is defined as:

$$MTR = (1 - M_{MT} / M_0) \times 100\% \qquad [1.6]$$

In which, M_{MT} is the signal intensity when there is MT effect, i.e., when an off-resonance RF pulse is applied; M_0 is the signal intensity when there is no MT effect, i.e., when no off-resonance RF pulse is applied (neglecting the on-resonance MT effect). MTR is a tissue dependent property which provides imaging contrast for MRI. For

example, white matter has a high MTR value (normally 10 to 60), gray matter has an intermediate MTR value (normally 5 to 40), and cerebrospinal (CSF) has a MTR value close to zero. In addition, lesions have a different MTR than normal tissues.

Effects of MT

We have shown that off-resonance RF pulses can induce MT. The magnitude of the off-resonance MT effects can be manipulated by changing the saturation frequency and power. Sometimes, off-resonance MT effects are unwanted and unavoidable. It alters the signal intensity and changes the apparent relaxation times. A common example is incidental MT effects in multi-slice MRI imaging (11,12). Different RF frequencies are used to excite different slices in a 2D multi-slice MRI experiment. However, the on-resonance frequency of one slice (e.g. the center slice) is likely within the range of MT-producing off-resonance frequencies (off by less than 5000 Hz) of the adjacent slice. Therefore, the signal intensity in the adjacent slice is not only determined by its own on-resonance excitation, but also affected by the excitation of other slice (i.e. the center slice) because of the off-resonance MT effects. Note that this MT effect is separated from slice overlapping effect in multi-slice imaging. The slice overlapping effect is caused by the imperfect slice profile (i.e. the Fourier Transform of a finite sinc pulse is a not exactly rectangular, generating a non-ideal slice profile). It can be largely reduced by increasing the slice gap and by using RF pulses that give sharp slice profiles. However, the MT effect can not be eliminated by increasing the gap or improving the slice profile. This MT

effect can lead to reduced signal intensity, image artifacts, and errors in relaxation times estimation in multi-slice imaging.

On-resonance RF pulses induce MT effects that are usually very small and therefore ignored. However, in some cases, it also causes significant effects in an MRI experiment. For example, the T_1 estimation is affected by on-resonance MT when using the multiple flip angle method. We are the first group to discover this, and the details of this inaccurate T_1 determination will be discussed in detail in Chapter 3. Another example is the on-resonance MT effect in the balanced steady state free precession (SSFP) pulse sequence (13). It was found that the measured tissue signal in the SSFP pulse sequence is significantly less than predicted. The high flip angles in combination with very short repetition times in the SSFP pulse sequence lead to a considerable saturation of macromolecular proton magnetization and therefore a decrease in the measured signal by MT effects.

Applications of MT

Since its discovery, MT has established itself as a new direction in the field of MRI. Published applications involve almost every type of tissue (14-17), and a variety of diseases (18-20). Figure 1.4 is an example of the application of MT in brain angiography (21).

Figure 1.4: The contrast between blood vessels and surrounding tissues is largely enhanced by MT effects in magnetic resonance angiography (MRA) (22). When an off-resonance RF pulse is applied, the signal from surrounding tissues will be decreased because of MT effect, while the signal from blood vessels won't be affected since blood has nearly no macromolecular protons and therefore nearly no MT effects. (Note: this figure is from reference 22)

One of the most established applications of MT is on central nervous system (CNS) diseases, such as multiple sclerosis (MS). MS is a chronic, inflammatory, and demyelinating disease that affects the central nervous system. MT effects have been suggested to be highly associated with myelin (23,24), and therefore, MT is very sensitive to demyelination, and is widely used in the study of MS. Dousset et al (19) found that the MTR in the white matter lesions of MS patients is significantly less than that in the white matter of healthy subjects; the MTR in the normal appearing white matter of MS patients is also decreased, which implies better sensitivity of MTR over

conventional T_1 and T_2 weighted images to MS. Gass et al (25) found an inverse correlation of disability with average lesion MTR in MS patients. Van Buchem et al (26) did volumetric analysis and found that the MTR histogram of MS patient is different form controls (Figure 1.5).

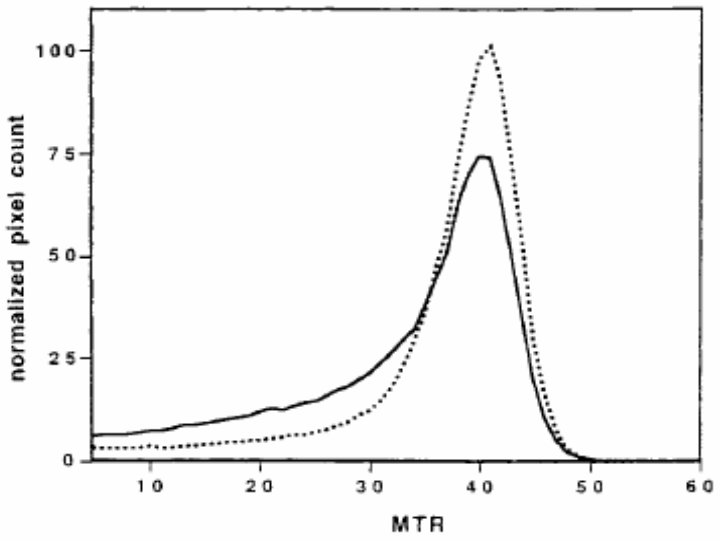

Figure 1.5: In general, MTR values in MS patients are lower than MTR values in healthy subjects. The solid line is the MTR histogram for a MS patient, the dashed line is the MTR histogram for a healthy individual. The healthy subject has more pixels in the brain with high MTR value, and less pixels in the brain with low MTR values. (Note: this figure is from reference 26)

Limitations of MTR

Numerous publications (14,19,25) have suggested that MTR is sensitive to MS. Though demyelination likely affects MTR the most, other pathologies in MS may also play a role to affect MTR. Edema, inflammation, axonal degeneration, etc, are also common pathologies in white matter diseases, and may co-existing with demyelination in MS.

Gareau et al (27) produced a chronic progressive model of experimental allergic encephalomyelitis (EAE) and manipulated inflammation by antibodies. They found that the measured MTR values were changed with the modulation of inflammatory activity, while the myelin content measured by multiple exponential T_2 experiment (Introduced in Appendix B) did not change. Does MD et al (28) studied the MTR, T_1 and T_2 properties in peripheral nerve. They found that the two short T_2 water components have different MT properties but similar MTRs. Schmierer et al (29) measured the MTR in postmortem multiple sclerosis brain with the addition of quantitative pathological studies. They found significant correlation not only between myelin content and MTR, but also between myelin content and axonal count. All of these findings suggest that a single value of MTR is not able to fully characterize the underlying pathology or even the full MT properties of the sample.

In addition, MTR is not an intrinsic property. Unlike the relaxation times T_1 and T_2, MTR is not only determined by the sample itself but also determined by the pulse sequence. Different off-resonance frequencies and different saturation powers generate different MTR values. Some research groups have attempted to standardize the acquisition parameters, the so called Euro-MT sequence (30). Even so, MTR values are difficult to reproduce at different research sites.

Introduction of QMT

Quantitative magnetization transfer (QMT) provides greater detailed information about

the MT process and possibly greater pathologies specificity than does MTR. A QMT model is still based on the magnetization transfer effects between free water proton magnetization and macromolecular proton magnetization. However, it describes the effects by a set of quantitative parameters instead of a single MTR value. These QMT parameters are independent to the pulse sequence and therefore are intrinsic properties. Figure 1.6 shows a QMT model for a two pool system with six QMT parameters (31).

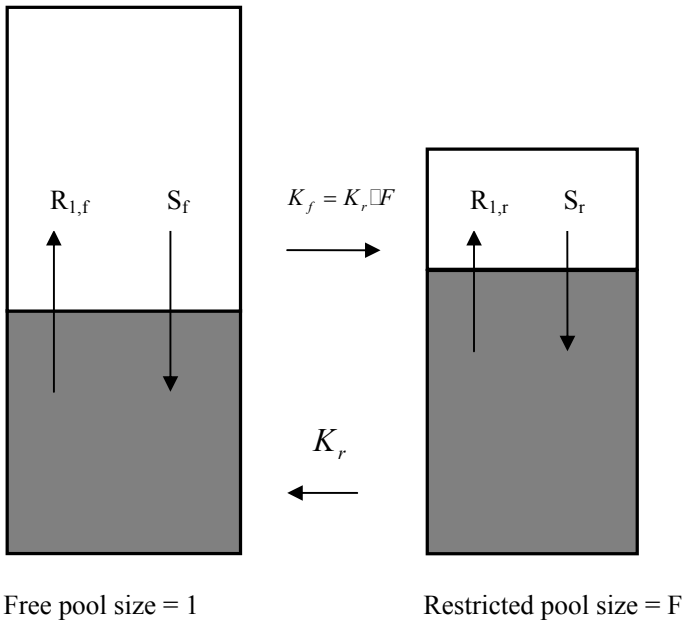

Figure 1.6: A two-pool QMT model: the shaded region in each pool represents the saturated magnetization, the unshaded region represents the remaining longitudinal magnetization. Subscripts f and r denotes free pool and restricted pool, respectively. The free pool size is normalized to one, the restricted pool size is F, giving a pool size ratio of F. R_1 is the longitudinal recovery rate (the reciprocal of the T_1 relaxation rate). S is the direct saturation rate (i.e. by an off-resonance pulse), which is determined by the saturation power, offset frequency, and the transverse decay rate T_2. K_f is the

exchange rate from the free pool to the restricted pool, and K_r is the exchange rate from the restricted pool to the free pool. $K_f = K_r \square F$.

In this two-pool QMT model, there are four relaxation parameters: $R_{1,f}, R_{1,r}, T_{2,f}, T_{2,r}$, and two exchange parameters: K_f, K_r. These six parameters are sequence-independent and they characterize the MT process completely. Together with the experimental parameters, they give all the information necessary to determine the measured magnetization after the magnetization transfer. The QMT model can be utilized in the opposite direction too: it is possible to determine the inherent QMT parameters from the measured magnetization. The relationship between measured magnetization and these QMT parameters strictly follows Bloch equations:

$$\begin{aligned}
\frac{dM_{x,f}}{dt} &= -\frac{M_{x,f}}{T_{2,f}} - \Delta M_{y,f} - \mathrm{Im}(\omega_1) M_{z,f} \\
\frac{dM_{y,f}}{dt} &= -\frac{M_{y,f}}{T_{2,f}} + \Delta M_{x,f} + \mathrm{Re}(\omega_1) M_{z,f} \\
\frac{dM_{z,f}}{dt} &= R_{1,f}(M_{0,f} - M_{z,f}) - K_f M_{z,f} + K_r M_{z,r} + \mathrm{Im}(\omega_1) M_{x,f} - \mathrm{Re}(\omega_1) M_{y,f} \\
\frac{dM_{z,r}}{dt} &= R_{1,r}(M_{0,r} - M_{z,r}) - K_r M_{z,r} + K_f M_{z,f} - W M_{z,r}
\end{aligned} \qquad [1.7]$$

where the subscripts x, y, and z denote the three components of a magnetization vector, Δ is the offset frequency of the applied RF pulse, ω_1 is the RF pulse field strength, and W is the saturation rate for the restricted pool from RF irradiation, which can be solved with the information of the absorption line-shape and T_2.

Applications of QMT Imaging

A primary application of QMT imaging is to provide novel information for clinical imaging studies that cannot be obtained via conventional MR or MTR imaging. QMT imaging increases the specificity of the dependence on the spin exchange mechanism in comparison to MTR imaging. Therefore, QMT has the advantage of better describing the intrinsic biological and pathological properties. For example, Sled and Pike (32) used their pulse saturation QMT technique to determine QMT parameters from both healthy and MS subjects. They found that the pool size ratio F is a more specific measurement of pathology in young lesions than MTR is, and the changes in lesions by age are more easily measured by the pool size ratio than by MTR. Tozer et al. (33) measured both the pool size ratio and MTR in MS lesions, NAWM in MS patients, and NAWM in healthy subjects. They found that when distinguishing MS lesion and NAWM in MS patients, pool size ratio has a much greater percentage difference than MTR does; when distinguishing NAWM in MS patients and NAWM in healthy subjects, pool size ratio has a clear difference while MTR value is less distinguishable. These research results suggest that QMT imaging may provide unique information on MS pathology which is not available via MTR measurements.

CHAPTER II

QMT IMAGING TECHNIQUES

There are several groups in the world developing and optimizing QMT techniques to determine QMT parameters (31,34-42). Their methods are similar in approach: measure the signal from a particular pulse sequence, develop a signal equation to characterize the magnetization evolution, and finally fit the measured signal to the signal equation to solve for the QMT parameters. Their pulse sequences differ in both saturation techniques and data acquisition. In general, these techniques can be categorized by their on-resonance or off-resonance saturation; they can also be categorized by their data acquisition during the transitory or steady-state periods of the magnetization evolution. In this chapter, a number of QMT techniques will be introduced. Their advantages and disadvantages will be discussed as well.

2.1. Data Analysis in QMT Imaging

Before discussing the QMT imaging methods, we first discuss the approaches used to analyze the resulting measured signals. In every QMT model, the magnetization evolution is dictated by the Bloch equations. However, due to the differences in the pulse sequence used, the measured magnetization varies. The magnetization can be predicted by either one of these two methods: numerically simulating the Bloch equations to derive

the magnetization evolution during a particular time interval, or analytically solving the Bloch equations to calculate the measured magnetization at the end point. The first method is accurate and straightforward, however, it is very time consuming due to the fourth and fifth order integration (ODE45) of differential equations (Bloch equations). The second one requires an analytical solution. Typically, deriving an analytical solution requires approximations. However, once the analytical solution is available, the computation of predicted magnetization is extremely fast. In general, the analytical solution is tested by numerical integrations to confirm the legitimacy of the approximations made.

The primary use of QMT models lies in the inverted direction: knowing the end-point magnetization (by measurements), how do we determine the intrinsic QMT parameters that describes the physical properties of the sample? This requires fitting the measured signal to a mathematical signal equation, where this signal equation is derived from the Bloch equations by numerical simulation, or analytical solution, or a combination of the two.

2.2. Off-Resonance Continuous Wave Irradiation Method

Henkelman et al. (31) is one of the first groups to determine all the QMT parameters from a steady state signal equation of the two-pool system. They performed off-resonance Continuous Wave (CW) irradiation MT experiments on agar gel. Figure 2.1 illustrated the pulse sequence used in their experiments.

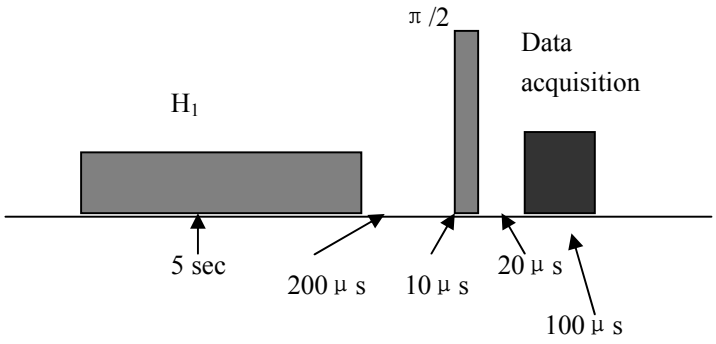

Figure 2.1: The pulse sequence for the CW experiment. A very long (5 seconds) irradiation time was used to ensure steady state had been reached. (Note: this figure is from reference 30)

For a steady state to exist, all the time derivatives in the Bloch equations of a coupled two-pool system must be equal to zero. The free pool is modeled by a Lorentzian absorption lineshape, the restricted pool is modeled by a Gaussian absorption lineshape. By noting that direct saturation of the free pool is small for large offset frequencies, the steady state signal equation can be solved:

$$M_{z,f,ss} = \frac{R_{1,r}\frac{K_f}{R_{1,f}} + S_r + R_{1,r} + \frac{K_f}{F}}{\frac{K_f}{R_{1,f}}\left(R_{1,r} + S_r\right) + \left(1 + \left(\frac{\omega_1}{2\pi\Delta}\right)^2\left(\frac{1}{R_{1,f}T_{2,f}}\right)\right)\left(S_r + R_{1,r} + \frac{K_f}{F}\right)} \qquad [2.1]$$

There are five independent model parameters in Eq. [2.1]: $R_{1,r}$, $T_{2,r}$, K_f / F, $K_f / R_{1,f}$, and $1/R_{1,f}T_{2,f}$. By performing the experiment at a number of different RF powers and different irradiation frequencies, and measuring the remaining free pool longitudinal magnetization, the five model parameters can be determined by fitting the measured data to Eq. [2.1]. Figure 2.2 shows an example data fitting.

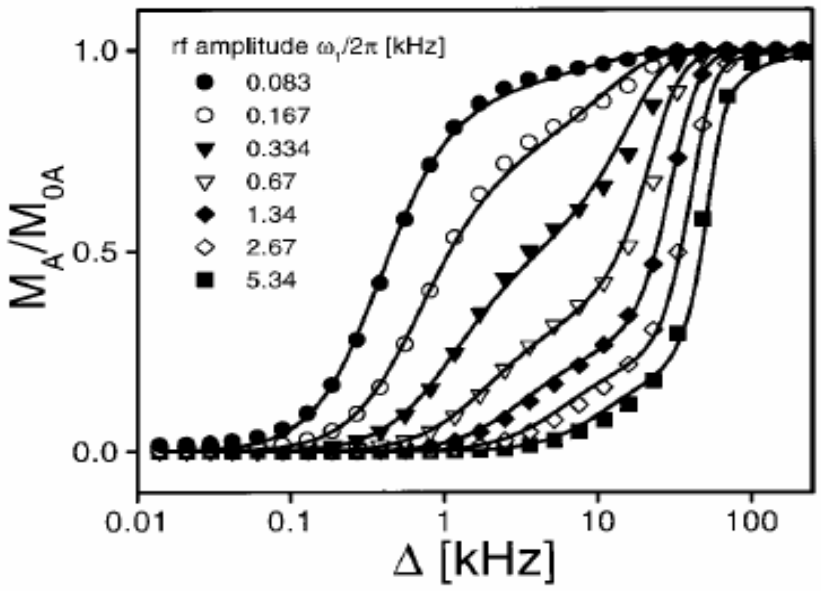

Figure 2.2: Measured data for 4% agar gel. Seven different RF amplitudes and 26 different offset frequencies were used. Solid lines are the fitting lines to Eq. [2.1]. (Note: this figure is from reference 30)

To get all of the six intrinsic QMT parameters from the obtained five model parameters, additional information is needed. An inversion recovery (IR) R_1 measurement was made, and a relationship between the observed recovery rate (R_1^{obs}) and the true R_1 of the free pool ($R_{1,f}$) was derived:

$$R_{1,f} = \frac{R_1^{obs}}{\left(1+\left(\frac{\left[\frac{K_f}{R_{1,f}}\right]\left(R_{1,r}-R_1^{obs}\right)}{\left(R_{1,r}-R_1^{obs}\right)+K_f/F}\right)\right)} \qquad [2.2]$$

With the measured R_1^{obs}, all of the six QMT parameters were able to be determined ($R_{1,r}$ is usually set to 1 Hz).

Off-resonance continuous wave irradiation QMT experiments have been extensively applied in non-imaging NMR studies of tissues and biopolymers. However, the Specific Absorption Rate (SAR) restrictions, and the inability to generate CW irradiation on most clinical scanners have limited the implementation of this technique on in vivo human studies.

2.3. Off-Resonance Pulse Saturation Method

Sled and Pike proposed a pulse saturation QMT method (32,41) that yields five of the six QMT parameters, and is able to estimate them in a clinically feasible scan time. The method is similar to Henkelman's, but with the long (in the order of seconds) RF application replaced by a series of short (in the order of 10 ms) RF pulses. We applied and tested this method on several concentrations of agar gel. An off-resonance MT pulse was applied, followed by a short, small angle excitation RF pulse (as illustrated in figure 2.3) and the sequence was repeated until a steady-state was reached. Strong spoiler gradients and RF spoiling techniques were used to eliminate residue transverse magnetization. Data were normalized by another scan without the saturation pulse, but otherwise identical.

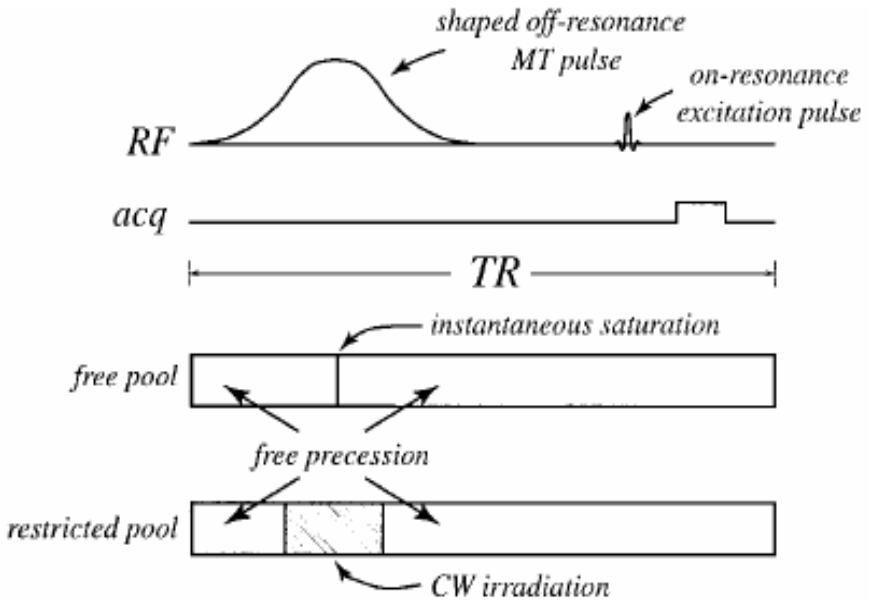

Figure 2.3: The spoiled gradient echo pulse sequence. The pulse sequence is decomposed into free precession, instantaneous saturation for the free pool, and rectangular pulse approximated CW irradiation for the restricted pool. Note that the instantaneous saturation of the free pool for the MT pulse and the excitation pulse has been combined. (Note: figure is from reference 32)

We modeled the behavior of the free pool longitudinal magnetization via the Bloch equations [1.7]. The pulse sequence was decomposed and the resulting magnetization was solved step by step with appropriate approximations. To increase the efficiency of data fitting, the direct saturation of the free pool (S_f) was computed in advance by numerically solving Bloch equations in the absence of magnetization exchange and T_1 relaxation. A three-dimensional saturation fraction lookup table was generated, with three factors: offset frequency, T_2 relaxation time of the free pool, and MT pulse power. Though it takes considerable computation time to numerically simulate S_f for a large size table, it only needs to be done once. During the data fitting, the saturation fraction

S_f can be looked up from this table instead of being repeatedly calculated. The direct saturation of the free pool by the excitation pulse was modeled by a simple rotation $\cos\theta$, in which θ is the excitation flip angle. The saturation effect on the restricted pool by the MT pulse was approximated by a rectangular pulse with the same offset frequency and average power. A Gaussian absorption line-shape was used for agar gel samples. The saturation effect on the restricted pool by the excitation pulse was neglected, due to the pulse's small flip angle and low power. After all of these approximations, the free pool magnetization is able to be solved under the steady state condition. Though the steady state signal equation is cumbersome and not shown here, it is able to be computed very quickly since it involves only matrix multiplication and not numerical integration.

Before actually fitting the data, the effects of non-uniform excitation field strength (B_1 inhomogeneity) and main magnetic field variation (B_0 inhomogenity) were considered. The effect of B_1 inhomogenity on the excitation pulse iss canceled by normalizing the data with respect to another scan without the saturation pulse but with the same excitation pulse. The effect on the saturation pulse was determined and corrected by mapping B_1 at every pixel via the modified stimulated echo method (43). The main magnetic field inhomogenity B_0 across the sample was also measured via a three-point Dixon method (44). This B_0 inhomogeneity corresponded to a frequency inhomogenity of around 60Hz on a 400MHz scanner, and this information was used to correct the offset frequency pixel-by-pixel.

We acquired two sets of MT weighted data for each agar gel sample. Set 1: $TR = 25ms$,

excitation angle $\theta = 7^{\circ}$, MT pulse length $= 10ms$, MT pulse power $= 200^{\circ}, 400^{\circ}, 600^{\circ}$, for 26 different offset frequencies varying from 800Hz to 100000Hz; set 2: $TR = 50ms$, $\theta = 10^{\circ}$, MT pulse length $= 30ms$, MT pulse power $= 400^{\circ}, 800^{\circ}, 1200^{\circ}$, for 26 different offset frequencies varying from 800Hz to 100000Hz. Both sets of data were used in the data fitting. Figure 2.4 shows the fitting results.

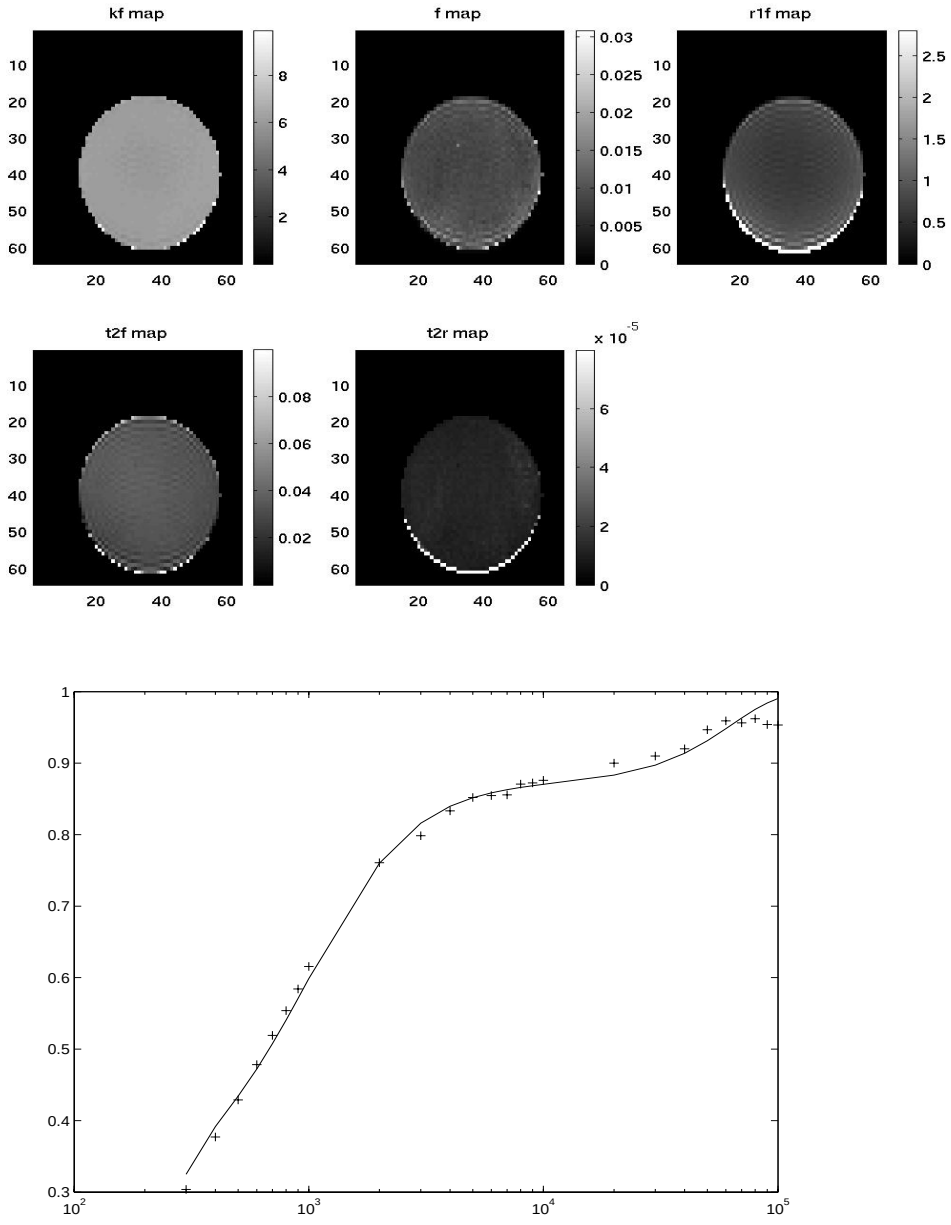

Figure 2.4: Top figure shows the MT parameters map for k_f, f, $R_{1,f}$, $T_{2,f}$, and $T_{2,r}$. ($R_{1,r}$ was set to 1). Bottom figure shows the least-squares fitting for one pixel at one MT power and 26 offset frequencies. The measured QMT parameters of agar gel samples are consistent with Henkelmen et al's results.

The results in figure 2.4 are based on our experiments when reproducing Sled & Pike's technique. They used an inversion recovery experiment to determine the observed recovery rate in order to provide information for $R_{1,f}$, and only fit their pulsed saturation data for four QMT parameters ($R_{1,r}$ was set to 1). We did our experiment both with and without an additional inversion recovery measurement, and analyzed the pulsed saturation data by both four and five parameters fitting. Our fitting results show that fitting to either four or five parameters gives accurate values for the agar gel sample. There is a trade off between five parameters fitting and four parameters fitting: the former doesn't need an extra inversion recovery measurement and thereby reduces the scan time; the latter takes more time to scan, but less time to analyze the data. Sled and Pike limit themselves to four parameters fittings to ensure robust and accurate least squared fitting.

Sled and Pike's method is by far the most comprehensive method for QMT parameters determination. However, this method has yet to be optimized. For example, the best choice of offset frequencies, saturation powers, repetition times, inter-pulse delays, etc, has yet to be determined.

2.4. Selective Inversion Recovery Method

A new QMT method called Selective Inversion Recovery Fast Spin Echo (SIR-FSE) method has been developed recently by Gochberg, et al (35,36), and it was used for the work presented in chapters 4,5, and 6. An inversion recovery pulse sequence with a fast spin echo readout is used in this method. The length of the inversion pulse is much longer

than $T_{2,r}$ and much shorter than $T_{2,f}$ and $1/K_r$. The inversion pulse affects the free pool and the restricted pool magnetization to different degrees. Specifically, the free pool magnetization is completely inverted if assuming an ideal 180° inversion pulse; the restricted pool magnetization is saturated to a degree depending on $T_{2,r}$. After the inversion pulse, magnetization transfer between the two pools will occur while the free pool magnetization recovers due to T_1 relaxation. The result of MT competing with relaxation is that the recovery rate is not determined solely by the relaxation rate but instead by a combination of relaxation and MT rates. At the beginning of the recovery (between 0 and ~ 20 milliseconds after the inversion pulse), the MT effect takes the lead; after that (~ 100 ms after the inversion pulse), the relaxation effect dominates. Therefore, the recovery of the free pool magnetization after the inversion pulse can be regarded as having two different rates: a slow recovery rate for long inversion times and a fast recovery rate for short inversion times.

The pulse sequence used in the SIR-FSE method and the corresponding magnetization evolution are shown in figure 2.5.

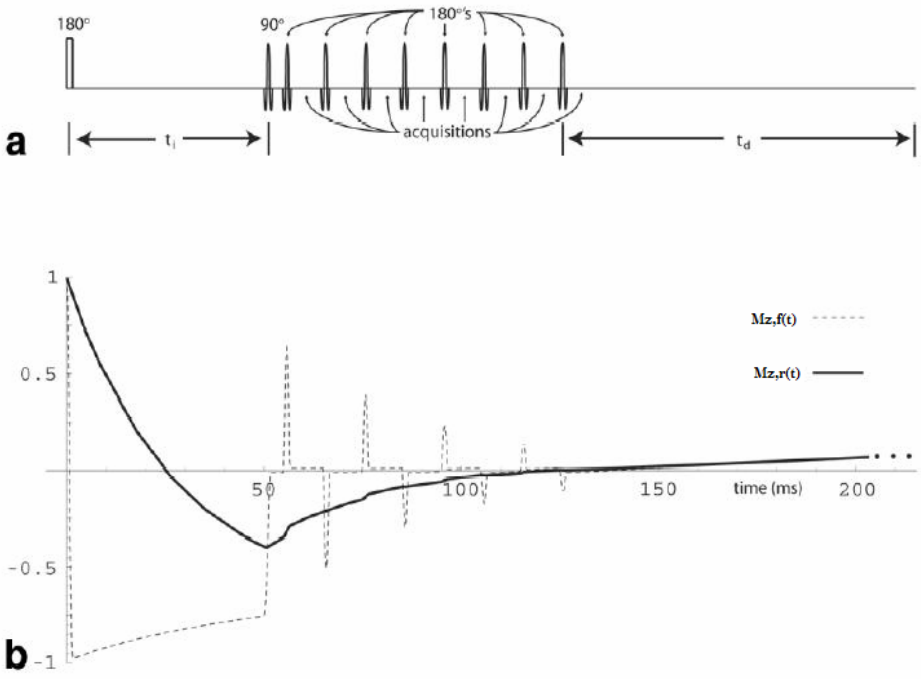

Figure 2.5: a) the pulse sequence; b) the simulated evolution of longitudinal magnetization. Note that after the series of 180° pulses in the FSE acquisition, both the free pool and restricted pool longitudinal magnetization will be zero: $M_{z,f}$ is flipped to transverse plane by the 90° pulse and any attempt to recover is inverted by the series of 180° pulses; $M_{z,r}$ is gradually pulled toward to zero by the saturation of $M_{z,f}$. After a constant time delay t_d, both the free pool and restricted pool magnetization evolve as $(1-e^{-t_d R_1^{obs}})$ towards their equilibrium values (right before the inversion pulse). (Note: this figure is from reference 36)

The bi-exponential recovery in the inversion recovery pulse sequence follows the Bloch equations. When there is no RF field applied, the evolution of the free pool and restricted pool magnetization after a disturbance is given by:

$$\frac{d}{dt}M_{z,f} = R_{1,f}(M_{0,f} - M_{z,f}) - K_f M_{z,f} + K_r M_{z,r}$$

$$\frac{d}{dt}M_{z,r} = R_{1,r}(M_{0,r} - M_{z,r}) + K_f M_{z,f} - K_r M_{z,r} \quad [2.3]$$

The solution of these equations is:

$$M_{z,f}(t) = M_{0,f} + C_1 e^{-\lambda_1 t} + C_2 e^{-\lambda_2 t} \quad [2.4]$$

Where

$$C_1 = -\frac{R_{1,f} + k_f - \lambda_2}{\lambda_2 - \lambda_1}(M_{z,f}(0) - M_{0,f}) + \frac{k_r}{\lambda_2 - \lambda_1}(M_{z,r}(0) - M_{0,r}) \quad [2.5]$$

$$C_2 = \frac{R_{1,f} + k_f - \lambda_1}{\lambda_2 - \lambda_1}(M_{z,f}(0) - M_{0,f}) - \frac{k_r}{\lambda_2 - \lambda_1}(M_{z,r}(0) - M_{0,r}) \quad [2.6]$$

And $\lambda_{1,2} = \frac{1}{2}(R_{1,f} + k_f + R_{1,r} + k_r) \mp \frac{1}{2}\sqrt{(R_{1,f} + k_f + R_{1,r} + k_r)^2 - 4(R_{1,f}R_{1,r} + R_{1,f}k_r + R_{1,r}k_f)}$

[2.7]

Equation [2.4] shows that the recovery of the free pool magnetization is bi-exponential, with a slow recovery rate λ_1 (which equals the observed recovery rate R_1^{obs}), and a fast recovery rate λ_2. If the SIR-FSE experiment is performed with an array of inversion times, the measured free pool magnetization can be fitted to Eq. [2.4] to determine $M_{0,f}, C_1, C_2, \lambda_1, \lambda_2$. It follows, after taking a Taylor expansion in the small parameter λ_1 / λ_2, that one of the QMT parameters, the pool size ratio, is calculated by: (36)

$$F = \frac{C_1}{C_1 + C_2 + 1 - S_r(1 - e^{-t_d R_1^{obs}})}, \text{ and } K_r = \lambda_2 \quad [2.8]$$

In which S_r is the direct saturation of the restricted pool magnetization by the 180° inversion pulse. It can be calculated by numerical simulation with a knowledge of an

estimated $T_{2,r}$.

Figure 2.6 illustrates a typical bi-exponential fit to the data from a SIR-FSE experiment, in this case to data from a single pixel of a bovine serum albumin (BSA) sample. The measured pool size ratio is consistent with literature values.

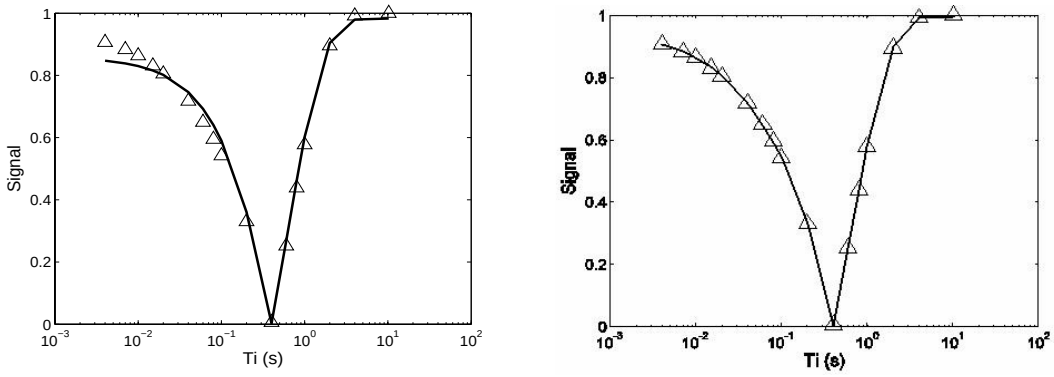

Figure 2.6: The figure on the left shows that the inversion recovery data can not be modeled by a single-exponential fitting; the figure on the right shows that the same data set fits well to a bi-exponential function, Eq [2.4].

The SIR-FSE method only yields a subset of MT parameters: The slow and fast recovery rates are determined by fitting data to a bi-exponential function; the pool size ratio is determined by Eq. [2.8]; the magnetization exchange rate K_r is found to be approximately equal to the fast recovery rate λ_2 by a first order Taylor expansion (37,38). However, SIR-FSE doesn't need strong assumptions on the restricted pool line-shape and doesn't need complicated gradient pulses to eliminate residue transverse magnetization. SIR-FSE is also relatively easy to implement in clinical MRI settings, and

the data analysis is straightforward.

2.5. Stimulated Echo Spin Labeling Method

Ropele et al (40) developed a new QMT method to measure the pool size ratio by a stimulated echo pulse sequence. The origin of their idea comes from the indicator dilution theory, as shown in figure 2.7.

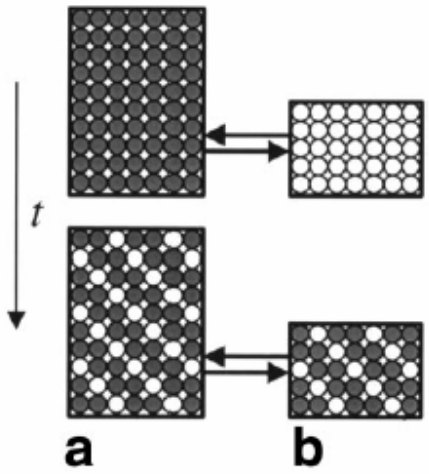

Figure 2.7: Principle of indicator dilution theory: suppose there are two exchangeable pools (a) and (b). Pool (a) is labeled with shaded circle as an indicator at the beginning. At time t, exchange process mixes pool (b) with pool (a), dilute the indicator. The fractional size of pool (b) then can be calculated from the change in indicator concentration. For example, if pool (a) is the free pool, pool (b) is the restricted pool, F is the pool size ratio, initial free water spins are labeled as an indicator, and C is the concentration of this indicator, then: $C_{afterMT} = C_{beforeMT} \frac{1}{F+1}$. (Note: this figure is from reference 40)

Phase distribution labeling provides an indicator for free pool magnetizations. It can be

accomplished by a stimulated echo pulse sequence with appropriate modulation and demodulation gradients, as shown in Figure 2.8.

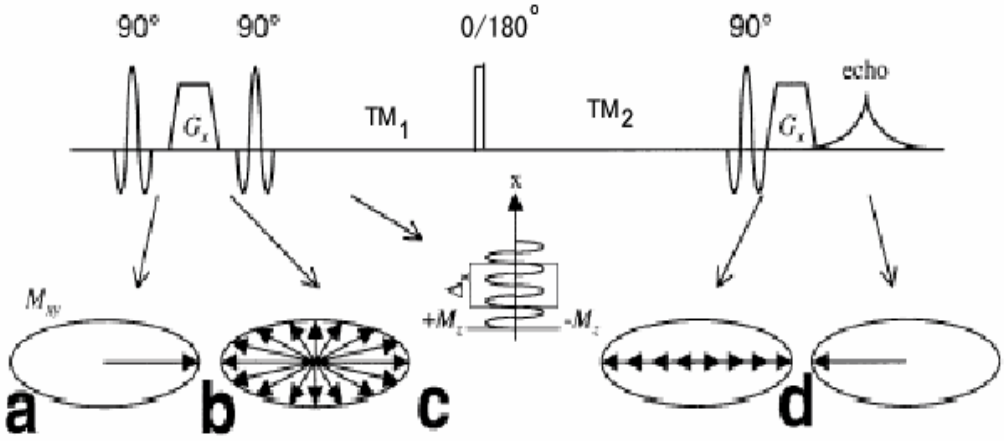

Figure 2.8: Using a stimulated echo preparation for labeling spins. (**a):** The first 90° pulse flips the longitudinal magnetization to the transverse plane. (**b):** The subsequent application of a modulation gradient *Gx* induces a phase shift of the individual spins depending on their position x along the modulation gradient. (**c):** The second 90° pulse flips the transverse magnetization back to the longitudinal direction and the individual phase shifts will be lost. However, the phase modulations turns into a spatial modulation of the longitudinal magnetization with the modulation frequency preserved during the mixing period despite transverse relaxation. (**d):** Following demodulation only spins which experienced the initial modulation will contribute to the echo provided that the modulation frequency is high enough to spoil the FID and signals from unwanted echoes. (Note: this figure is from reference 40)

The approximate solution of Eq. [2.3] at a time t after the second 90° pulse is (40):

$$M_{z,f}(t) \approx M_{0,f} \frac{1}{F+1}(e^{-\lambda_1 t} + Fe^{-\lambda_2 t}) \qquad [2.9]$$

For $t > 1/\lambda_2$, the above equation can be rewritten as:

$$M_{z,f}(t) \approx M_{0,f} \frac{1}{F+1} e^{-\lambda_1 t} \qquad [2.10]$$

Two stimulated echo scans are performed, one with a 180° hard inversion pulse during the mixing time, one without the 180° pulse. For the scan without the inversion pulse, the free pool magnetization at the end of the mixing time is:

$$M_1 = M_0 \frac{1}{F+1} e^{-\lambda_1 (TM_1 + TM_2)} \quad [2.11]$$

For the scan with the inversion pulse, the free pool magnetization right before the pulse is:

$$M' = M_0 \frac{1}{F+1} e^{-\lambda_1 TM_1} \quad [2.12]$$

The 180° inversion pulse changes the sign of the phase of the free pool spins but not the restricted pool spins. Meanwhile, the imbalance dilutes the originally labeled free water spins. Therefore, for the scan with the inversion pulse, the free pool magnetization at the end of the mixing time is:

$$M_2 = -M' \frac{1}{F+1} e^{-\lambda_2 TM_2} + S_r M' \frac{F}{F+1} e^{-\lambda_2 TM_2} \quad [2.13]$$

In which S_r is the direct saturation of the restricted pool magnetization by the 180° inversion pulse. By comparing the measured signal intensity of these two scans, the pool size ratio can be calculated as:

$$F = \frac{M_1 - M_2}{S_r M_1 + M_2} \quad [2.14]$$

Additional B_1 mapping and T_1 relaxation measurements are not required by this method. Power intensive RF pulse and complex data fitting are avoided. However, only one QMT parameter, the pool size ratio, is determined. This method has been applied to a BSA sample and in vivo subject. The measured pool size ratio is consistent with published

results; the requirement of only two scans makes this method very applicable for in vivo QMT study.

2.6. Other QMT Methods

In addition to the two off-resonance and two on-resonance QMT methods discussed above, some other methods have been developed using different approaches.

Like Sled and Pike, Yarnykh (45) also used off-resonance pulse saturation to quantify MT parameters. However, only frequencies far from resonance ($\geq 4kHz$) were investigated. They assumed that there was no direct saturation, after additional approximations, they proposed a simple signal equation:

$$MTR \approx \frac{sW^B}{P + QsW^B} \qquad [2.15]$$

where s is the ratio of the MT pulse length to the repetition time, P and Q are both functions of K_f, F, R_1^{obs}, and the pulse sequence parameters. W^B is the average saturation rate of the restricted pool, which is a function of $T_{2,r}$. By measuring MTR for different offset frequencies and MT powers, P, Q, W^B can be determined by fitting data to equation [2.15]. With an additional measurement of R_1^{obs}, the MT parameters K_f, F, and $T_{2,r}$ can be determined.

This method requires less scan time and is relatively simple for data analysis. However, it only yields three MT parameters, and the strong assumption of no direct saturation limits the accuracy of MT parameter estimation.

Tyler et al (46) proposed a QMT technique based on a chain of off-resonance pulses and Echo Planer Imaging (EPI). By numerical simulation of the magnetization evolution to steady state, they obtained a signal equation to determine MT parameters. They measured the apparent longitudinal recovery rate R_1^{obs}, assumed $R_{1,r}$ and K_r to be known constants. By that they obtained a simple relation to get $R_{1,f}$ directly from $R_{1,obs}$ and F. Also they measured the apparent relaxation rate T_2^{obs} and assumed that $T_{2,f}$ includes both the relaxation and exchange terms of the transverse magnetization, i.e. $T_{2,f} = T_2^{obs}$. After all of these preliminary measurements and approximations, they were able to simplify their signal equation so that it contains only two free QMT parameters, $T_{2,r}$ and F, which are convenient to be determined by data fitting. Their fitting results for the pool size ratio F show a linear increasing relationship with the increasing concentration of agar gel samples. However, their results for $T_{2,r}$ are inconsistent with the literature results.

Chai et al (34), Lee et al (47) also proposed new QMT methods which are capable for QMT parameters determination but either limited by long scan time or restricted to a subset of parameters only. Many other QMT measurements are made by Graham et al (48), Ramani et al (39), and Tozer et al (33), etc. More or less, their methods are based on the method by Henkelman et al (31).

In summary, many QMT imaging techniques have been developed and implemented in medical imaging research by scientists. Most of those techniques give accurate estimation of some QMT parameters, such as the pool size ratio. However, the optimization of each

QMT model, the direct comparison of different QMT methods, and the ultimate choice of the best QMT imaging technique are still open topics.

CHAPTER III

MT EFFECTS IN SINGLE SLICE SPOILED GRADIENT ECHO IMAGING

We have previously mentioned MT effects in some cases, such as the multi-slice imaging, steady state free precession imaging, etc. In this chapter, we will introduce another MT effect which is ignored by most people but still very important. We will discuss the origin of this MT effect, the role it plays in MRI imaging, and how to take advantage of this MT effect.

Specifically, We investigated magnetization transfer (MT) effects on the steady state MR signal for a sample subjected to a series of identical on-resonance RF pulses, such as would be experienced while imaging a single slice using a spoiled gradient echo sequence. The MT coupling terms for a two-pool system were added to the Bloch Equations, and we derived the resulting steady state signal equation and compared this result to the conventional signal equation without MT effects. The steady state signal is increased by a small amount because of MT. Consequences of this MT effect include 1) inaccuracies in T_1 values determined via conventional steady state gradient echo methods and 2) the ability to quantify the relaxation and MT parameters by fitting the gradient echo steady state signal to the signal equation appropriately modified to include MT effects.

3.1. Signal Equation and Numerical Simulation

It is well known that MT occurs when applying an off-resonance RF pulse to samples with two biological pools. The thermal equilibrium between the pools is broken after an off-resonance RF pulse, resulting in spin exchange between these pools. It is not well appreciated that MT also occurs when applying an on-resonance RF pulse. In fact, any pulse that affects the two proton pools differently (and nearly every RF pulse does) will induce MT. Off-resonance pulses saturate the restricted pool to a greater extent than the free pool; on-resonance pulses rotate the free pool while having little effect on the restricted pool (when at low power).

Steady state signal equation for gradient echo sequence

We consider a simple gradient echo pulse sequence with the excitation pulse set on resonance. Bloch Equations are used to predict the steady state signal of this sequence. For samples with only one biological pool, the transverse steady state signal derived from the Bloch Equations is (49):

$$M_{xy,f,ss} = M_{0,f} \sin\alpha \frac{1-E_1}{1-E_1\cos\alpha} \qquad [3.1]$$

Where $M_{0,f}$ is the equilibrium longitudinal magnetization for the biological pool, α is the excitation pulse flip angle, $E_1 = e^{-TR*R_1}$, and R_1 is the longitudinal recovery rate. (The T_2^* relaxation term is normalized to 1 since constant TE is assumed).

For samples that have two biological pools, coupling terms have to be added to the Bloch Equations in order to accurately model the underlying magnetization transfer, as shown in Eq. [2.3]:

$$\frac{d}{dt}M_{z,f} = R_{1,f}(M_{0,f} - M_{z,f}) - K_f M_{z,f} + K_r M_{z,r}$$

$$\frac{d}{dt}M_{z,r} = R_{1,r}(M_{0,r} - M_{z,r}) + K_f M_{z,f} - K_r M_{z,r}$$

We have presented the solutions of these equations earlier:

$$M_{z,f}(t) = M_{0,f} + C_1 e^{-\lambda_1 t} + C_2 e^{-\lambda_2 t}$$

$$M_{z,r}(t) = M_{0,r} + C_1 \frac{R_{1,f} + K_f - \lambda_1}{K_r} e^{-\lambda_1 t} + C_2 \frac{R_{1,f} + K_f - \lambda_2}{K_r} e^{-\lambda_2 t}$$

In which

$$C_1 = -\frac{R_{1,f} + K_f - \lambda_2}{\lambda_2 - \lambda_1}(M_{z,f}(0) - M_{0,f}) + \frac{K_r}{\lambda_2 - \lambda_1}(M_{z,r}(0) - M_{0,r})$$

$$C_2 = \frac{R_{1,f} + K_f - \lambda_1}{\lambda_2 - \lambda_1}(M_{z,f}(0) - M_{0,f}) - \frac{K_r}{\lambda_2 - \lambda_1}(M_{z,r}(0) - M_{0,r})$$

And

$$\lambda_{1,2} = \frac{1}{2}(R_{1,f} + K_f + R_{1,r} + K_r) \mp \frac{1}{2}\sqrt{(R_{1,f} + K_f + R_{1,r} + K_r)^2 - 4(R_{1,f}R_{1,r} + R_{1,f}K_r + R_{1,r}K_f)}$$

With the addition of the excitation pulse at the beginning of each repetition (we treat the RF pulses as simple rotations of the free pool magnetization, with no relaxation and magnetization transfer effects during the relative short pulse), the steady state signal is obtained by solving the equations:

$$M_{z,f}(t) = M_{z,f}(t + TR)$$

$$M_{z,r}(t) = M_{z,r}(t + TR)$$

The resulting transverse steady state signal for the free pool is:

$$M_{xy,f,MTss} = \sin\alpha M_{z,f,MTss} = M_{0,f}\sin\alpha \frac{(1-E_1)(1-E_2S_r)+A(1-S_r)(E_1-E_2)-\frac{K_f}{\lambda_2-\lambda_1}(1-S_r)(E_1-E_2)}{(1-E_1S_f)(1-E_2S_r)+A(S_f-S_r)(E_1-E_2)} \quad [3.2]$$

where

$$A = \frac{R_{1,f}+K_f-\lambda_1}{\lambda_2-\lambda_1}$$

$$E_1 = e^{-\lambda_1 \cdot TR} = e^{-R_1^{obs} \cdot TR}$$

$$E_2 = e^{-\lambda_2 \cdot TR}.$$

$S_f = \cos\alpha$ is the direct rotation of the free pool magnetization by the RF pulse, and S_r is the direct saturation of the restricted pool magnetization by the RF pulse. S_r can be calculated from numerically simulating the magnetization before and after the pulse, where

$$M_{z,r}(after \cdot pulse) = S_r \cdot M_{z,r}(before \cdot pulse).$$

Equation [3.2] is an exact solution of the steady state signal equation with the only assumption that there are no relaxation and MT effects during the RF pulse. We can make two more approximations to simplify Eq. [3.2].

First, for gel samples and biological tissues, K_r is much greater than other rates (37,38,40), such as $K_f, R_{1,f}$ and $R_{1,r}$. To first order in $1/K_r$: $\lambda_2 \approx K_r$, $A \approx F/(1+F)$, and $A - \frac{K_f}{\lambda_2-\lambda_1} \approx 0$.

Second, we set $E_2 = 0$ in the calculation of $M_{xy,f,MTss}$, recognizing that for typical parameter values, E_2 is non-zero only for short TR's, where E_1 is close to 1; and when E_1 is 1, $M_{xy,f,MTss}$ is independent of E_2. Therefore, we will take $E_2 = 0$ for all TR values.

After these two approximations, Eq. [3.2] is simplified to:

$$M_{xy,f,MTss} = \sin\alpha M_{z,f,MTss} = M_{0,f}\sin\alpha\frac{1-E_1}{(1-E_1S_f)+A(S_f-S_r)E_1} \quad [3.3]$$

Numerical simulations to test the signal equation

Numerical integration of the complete Bloch Equations (Eq. [1.7]) was performed to generate numerical steady state data. MT parameters for white matter (32) and a series of repetition times and flip angles were used in the numerical data generation. To test the accuracy of our signal equation and the legitimacy of the approximations we made during the signal equation derivation, we generated numerical data by two steps.

In the first step, relaxation and exchange during the RF pulse were not considered in the numerical integration. For each repetition time and flip angle, the integration was continued until signal change for consecutive repetitions was less than 0.001%. We found that the numerical data match the data calculated by Eq. [3.2] very well (the signal difference, which is due to the finite step size in the integration, is less than 0.01% of the equilibrium magnetization, as shown in figure 3.1). The coincidence of the numerical data and the Eq. [3.2] data indicates that our signal equation accurately describes the steady state signal if we ignore the relaxation and exchange effects during the RF pulse.

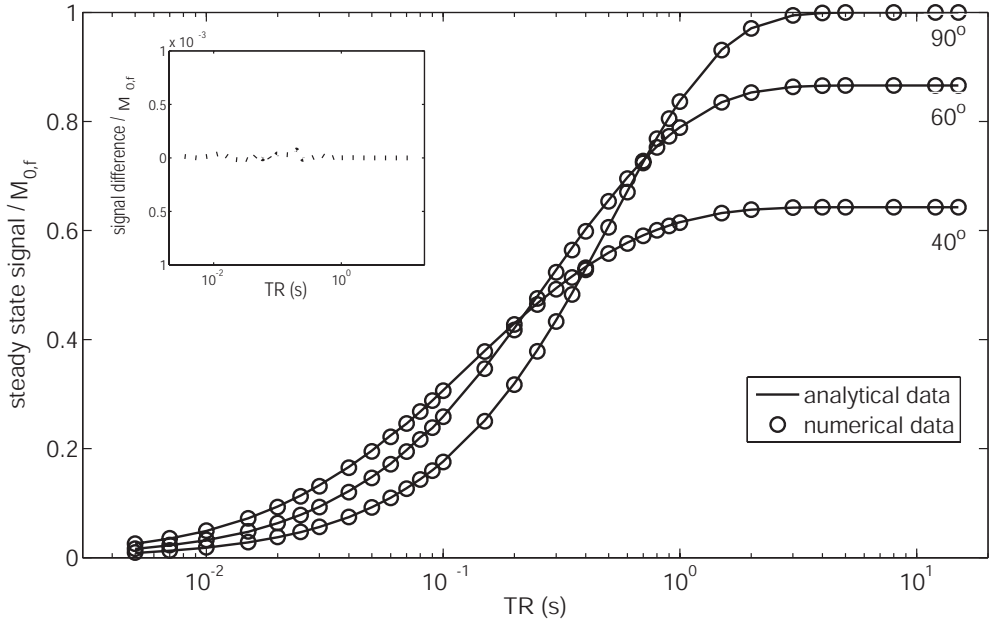

Figure 3.1: Transverse steady state signal generated from numerical methods for 32 different repetition times and 3 different excitation angles, comparing to the signal calculated from signal Eq. [3.2]. All data are normalized to $M_{0,f}$. The small figure is an example to show the small difference between the analytical data ($\alpha = 90^{\circ}$) and the numerical data. MT parameters for white matter (32) were used in the numerical data generation: $K_r = 30.26s^{-1}, F = 0.152, R_{1,f} = 1.8s^{-1}, R_{1,r} = 1s^{-1}$, $T_{2,f} = 0.038s, T_{2,r} = 1.14 \times 10^{-5} s$. (Unless specially noted, all of the numerical and analytical data in this chapter were generated by these QMT parameter values)

In the next step, we evaluated the relaxation and exchange effects during the RF pulse by numerical simulation. During the RF pulse, we added (a) MT exchange terms only; (b) R_1 relaxation terms only; (c) T_2 relaxation terms only; and (d) with all exchange and relaxation terms to the Bloch Equations. In all cases, all relaxation and exchange terms were included in the Bloch Equations after the RF pulse. Figure 3.2 compares these

four sets of numerical data to the analytical data generated by Eq. [3.2]. It was found that the magnetization exchange effect during the RF pulse is very small (on the order of $10^{-5} \times M_{0,f}$); the R_1 and $T_{2,f}$ relaxation effects during the RF pulse are also small but noticeable (on the order of a few parts per thousand).

These small differences between Eq. [3.2] and the numerical simulations including exchange and relaxation during the RF pulse can be minimized by modification of TR and S_f in Eq. [3.2]. By using TR = interpulse delay + pulse width / 2, instead of TR = interpulse delay + pulse width, in Eq. [3.2], the effect of R_1 during the pulse can be largely compensated (data not shown). Difference originating in T_2 effects during the RF pulse can be mitigated by using $S_f = \cos(factor * \alpha)$, instead of $S_f = \cos(\alpha)$, in Eq. [3.2], where the factor is determined by numerical simulation of a single RF pulse ignoring exchange (data not shown). Figure 3.2, line (e) illustrates that modifying TR and S_f reduces the difference between Eq. [3.2] and numerical simulation to $< 10^{-3} M_{0,f}$ (and the difference is almost two orders of magnitude less than MT effects after the RF pulse, as will be shown below).

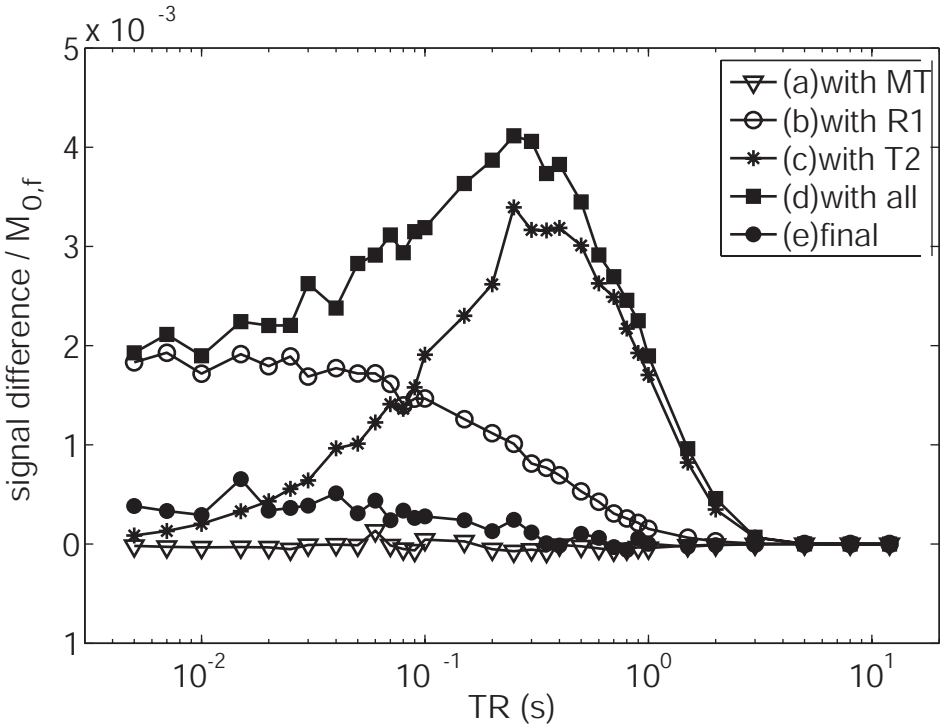

Figure 3.2: The difference between the analytical data generated from Eq. [3.2] and the numerical data generated with consideration of (a) MT, (b) R1 relaxation, (c) T2 relaxation, (d) all relaxation and exchange terms, and (e) all terms (but with the repetition time starting from the center of the RF pulse and a numerically determined factor of 0.9921 multiplied to S_f) during a 1.5 ms hard (square) RF pulse. Modifications in part (e) reduce the discrepancy between the numerical and analytical solutions by an order of magnitude. Note that the repetition time after modification is actually a better reflection of true TR since the RF pulse can not be instant in real experiments; also the modification of S_f does not require additional numerical determination of the correcting factor when modeling experimental data, since a b_1 compensation factor will be implemented in experiments, as discussed in the Experimental Methods section of this paper. Flip angle $\alpha = 90^\circ$ is used in this figure.

To test the accuracy of the simplified signal Eq. [3.3], we compared the analytical solution results from Eq. [3.3] to the results from Eq. [3.2]. Figure 3.3 shows that the steady state data deviation is less than 0.1% of the equilibrium magnetization $M_{0,f}$, and Eq. [3.3] is an excellent approximation of Eq. [3.2].

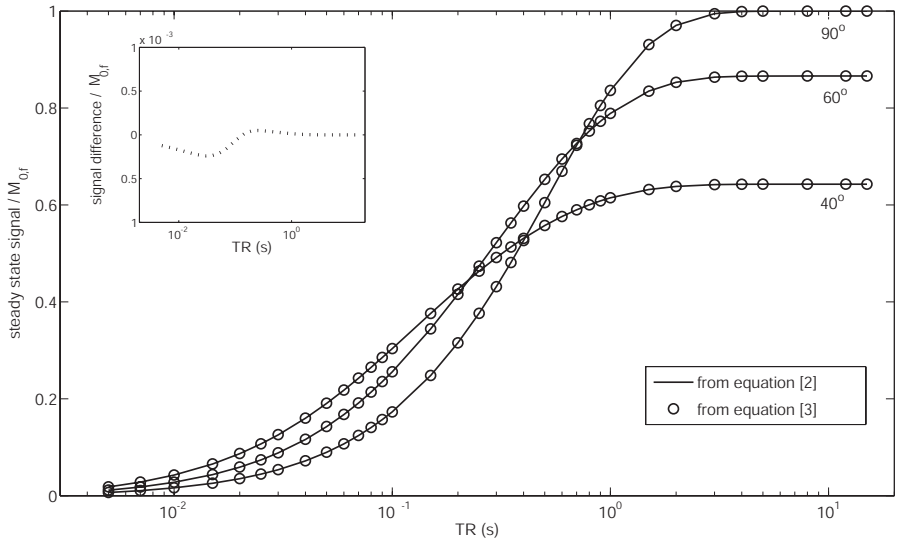

Figure 3.3: The comparison of analytically calculated steady state signal from Eq. [3.2] and Eq. [3.3] for different repetition times and flip angles. The small figure is an example ($\alpha = 90^{\circ}$) to show that the difference between them is much less than 0.1% of the equilibrium magnetization.

3.2. MT Effects in Gradient Echo Imaging

MT effects increase the steady state signal

Figure 3.4 show that MT effects always increase the steady state signal. The relative signal increase (comparing to signal without MT effects) can be as high as 14%; the

absolute signal increase (normalized to the equilibrium magnetization $M_{0,f}$) is up to about 3%, roughly two orders of magnitude greater than any systematic errors due to our analytical approximations (see figure 3.2, line (e)).

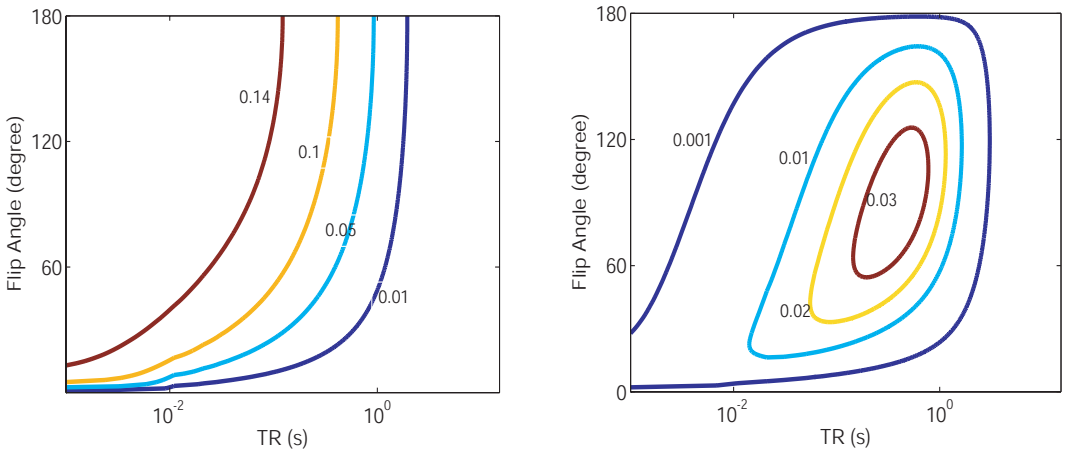

Figure 3.4: Left: The contour plot for (signal with MT – Signal without MT) / (signal without MT) for different repetition times and flip angles. Right: The contour plot for (signal with MT – Signal without MT)/ $M_{0,f}$ for those repetition times and flip angles. The signal with and without MT are from Eq. [3.2] and Eq. [3.1], respectively, and sample parameters are for white matter (32).

Optimization of gray/white matter contrast

Another application of MT effects on gradient echo imaging is white matter/gray matter contrast. A specific range of flip angle is required to enhance the white matter/gray matter contrast when using Gradient Echo sequences. MT effects may shift this flip angle range. Figure 3.5 indicates that the crossing angle (at which there is no contrast between white matter and gray matter) has a small change due to MT effects.

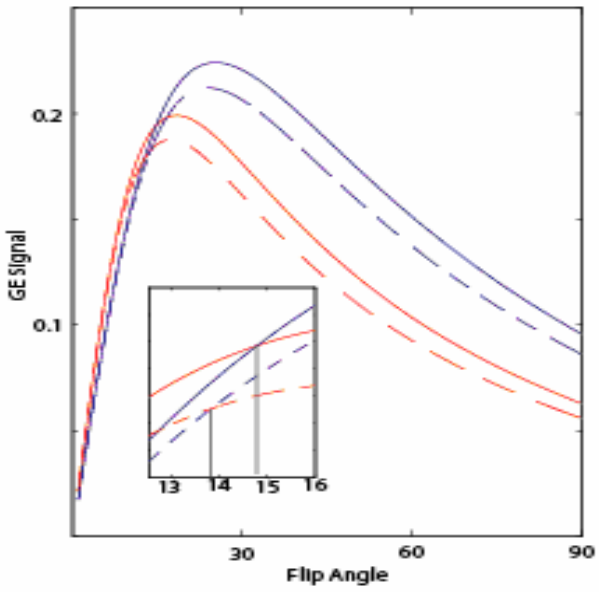

Figure 3.5: Red lines show gray matter signal, blue lines show white matter signal. Dashed lines are the signal without MT effects (from Eq. [3.1]), Solid lines are the signal with MT effects (from Eq. [3.2]). MT parameters for normal white matter and gray matter (32) were used to calculate steady state signal. The crossing angle shifts by about one degree; the maximum contrast flip angle for each matter also shifts by about one degree.

T_1 quantification by gradient echo is inaccurate if MT is ignored

T_1 is often measured by setting a TR, varying the flip angle α, and fitting the gradient echo signal to Eq. [3.1]. However, the increased steady state signal caused by MT will affect the estimation of T_1. If we ignore the MT effects and fit the data to Eq. [3.1], while the actual signal is described by Eq. [3.2], we will end up with a T_1 rate that is a function of TR, S_f, and S_r:

$$R_1 = \frac{1}{TR}\ln\frac{(1-S_f)(1-E_2S_r - AE_1S_r + AE_2S_r) + K_f S_f / \lambda_2 - \lambda_1 (1-S_r)(E_1 - E_2)}{(1-S_f)(E_1 - AE_1 + AE_2 - E_1E_2S_r) + K_f / \lambda_2 - \lambda_1 (1-S_r)(E_1 - E_2)} \quad [3.4]$$

Therefore, the measurement of the recovery rate R_1 (the reciprocal of the T_1 relaxation time) in white matter will be affected to a degree depending on TR and α if we ignore MT effects. If we instead consider MT effects and fit the data to Eq. [3.2], the measured R_1 is the true value. (Note that for samples with zero pool size ratio, Eq. [3.4] is reduced to $R_1 = \frac{1}{TR}\ln\frac{1}{E_1}$, matching the conventional case)

This inaccurate T_1 quantification is not negligible for *in vivo* experiments. For example, the QMT parameters for frontal white matter and cortical gray matter in the brain of a healthy subject (32) were used to generate gradient echo steady state data from Eq. [3.2]. If we choose a constant TR, vary the flip angle α, and fit the gradient echo data to Eq. [3.1], the fitted R_1 can be up to 15% higher than the true R_1^{obs} value for the frontal white matter, and 7% higher for the cortical gray matter, as shown in figure 3.6.

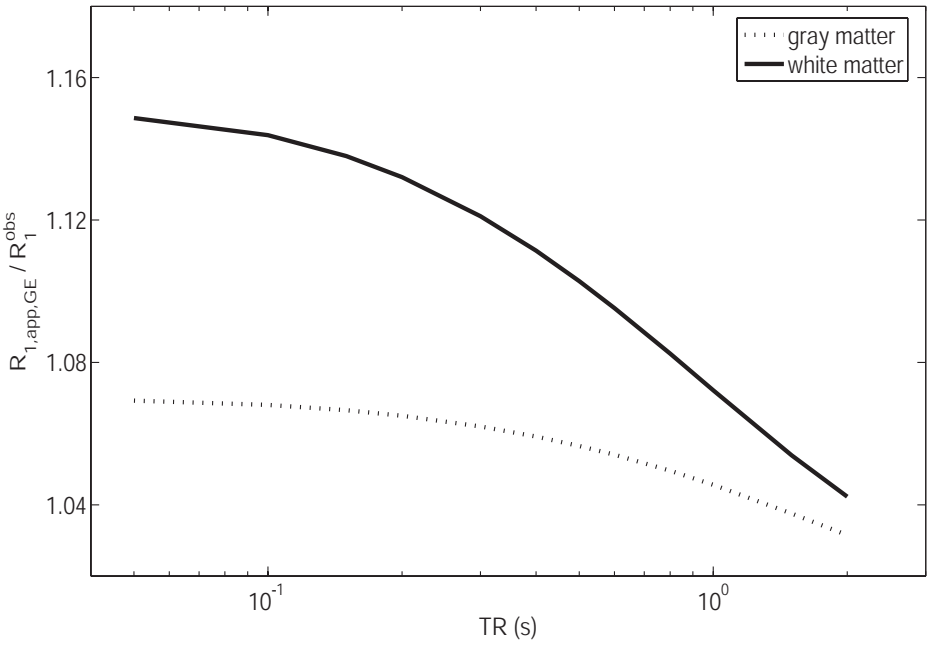

Figure 3.6: The fitted apparent R_1 ($R_{1,app,GE}$) values depend on the choices of TR for white matter and gray matter when choosing a TR, varying the flip angle α, and fitting the analytically generated spoiled gradient echo steady state data to Eq. [3.1] instead of Eq. [3.2].

Experiments were performed on a 4.7T Varian system to test the multiple flip angle T_1 measurements by gradient echo sequence. 3 uniform samples were measured: sample 1 is 0.1mM $MnCl_2$ ($T_1 \approx 400ms, F = 0$), sample 2 is cross-linked 15% BSA ($T_1 \approx 1750ms, F \approx 0.1$), and sample 3 is cross-linked 15% BSA mixed with 0.1mM $MnCl_2$ ($T_1 \approx 720ms, F \approx 0.1$). Each sample was put in a nmr tube of 8 mm diameter and 32mm length. 3 tubes were tied together parallelly and placed at the center of a 63mm diameter quad coil. In all of the gradient echo pulse sequences, TE was set to 5 ms. 32x32 data points in the k space were acquired for each scan. 32 Dummy scans were performed before each data

acquisition in order to ensure a steady state condition. To destroy spin and stimulated echoes, spoiler gradients with linearly changing magnitudes were placed after the data acquisition, and a phase step of 84° was set to the excitation pulse for RF spoiling. Gradient echo steady state data were acquired with 12 repetition times ($TR = 0.05, 0.1, 0.15, 0.2, 0.3, 0.4, 0.5, 0.6, 0.8, 1, 1.5, 2s$), 15 flip angles ($\alpha_{input} = 20^\circ, 30^\circ, 40^\circ, 50^\circ, 60^\circ, 70^\circ, 80^\circ, 90^\circ, 100^\circ, 110^\circ, 120^\circ, 130^\circ, 140^\circ, 150^\circ, 160^\circ$), and a 600 μs hard excitation pulse. No slice selection gradient was applied in this experiment. The data is fit to Eq. [3.1] with $\alpha = \alpha_{input} * b_1$, where b_1 accounts for linear RF field errors due to amplifier miscalibration and B_1 spatial variation. That is, we fit the signal at each pixel to Eq. [3.5] to determine $M_{0,f}, R_1$, and b_1.

$$M_{xy,f,ss} = M_{0,f} \sin(b_1 * \alpha_{input}) \frac{1 - e^{-TR*R_1}}{1 - e^{-TR*R_1} \cos(b_1 * \alpha_{input})} \qquad [3.5]$$

Figure 3.7 shows the fitted recovery rate when ignoring MT (and therefore fitting the data to Eq. [3.5]). The fitted R_1 is a constant value and roughly equal to (R_1^{obs}) for samples with zero pool size ratio ($MnCl_2$), but it is a function of TR for samples with non-zero pool size ratio ($BSA + MnCl_2$ and BSA), as expected in Eq. [3.4]. The measured recovery rates R_1 approach R_1^{obs} as TR increases. Figure 3.7 confirms the theoretical results in figure 3.6.

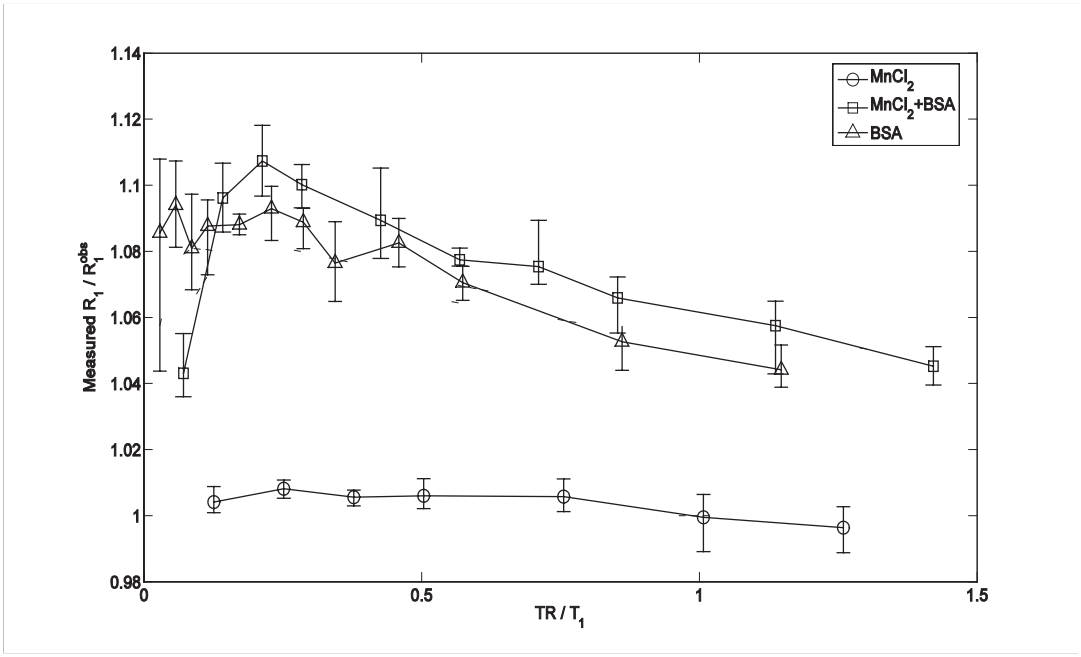

Figure 3.7: The fitted recovery rate when ignoring MT by using a gradient echo imaging sequence (without slice selection) and fitting the data to Eq. [3.5] for $MnCl_2$ (O), $MnCl_2 + BSA$ (□), and BSA (△) .The referential $T_1 = 1/R_1^{obs}$ is obtained from a separate inversion recovery experiment that used inversion times > 100 ms. The uncertainties were obtained by repeating the measurements three times.

3.3. QMT Parameters Determination by Gradient Echo Sequence

QMT parameters determination for numerical/analytical data

From Eq. [3.2], the spoiled gradient echo steady state signal equation including MT effects has the form: $M_{xy,f,MTss} = M_{xy,f,MTss}(\alpha, TR, M_{0,f}, \lambda_1, \lambda_2, A, K_f)$. It is a function of two experimental parameters (TR, α) and five MT parameters ($M_{0,f}, \lambda_1, \lambda_2, A, K_f$). We fitted the analytically generated steady state data (with white Gaussian noise) to this function to

determine the MT parameters $M_{0,f}, \lambda_1, \lambda_2, A, K_f$, and found that these five parameters can be determined by least-squared non-linear fitting. However, the robustness of the fitting results varies for each parameter. A Monte Carlo method was used to determine the standard deviation of the fitted parameters for different signal noise ratio values. The results are plotted in figure 3.8 and shown in table 3.1. Note that some parameters have grossly non-Gaussian histograms. Such parameter fittings far from the input value indicate a lack of robustness in the fitting procedure, i.e. they indicate the chances of the fitting going off to "left field". These misfittings are not due to fitting to a local, as opposed to a global minimum. Refitting these misfitted Gaussian noise sets by taking the minimum residue starting at 1000 randomly distributed initial parameter guesses did not significantly alter the fitted parameter histogram (data not shown).

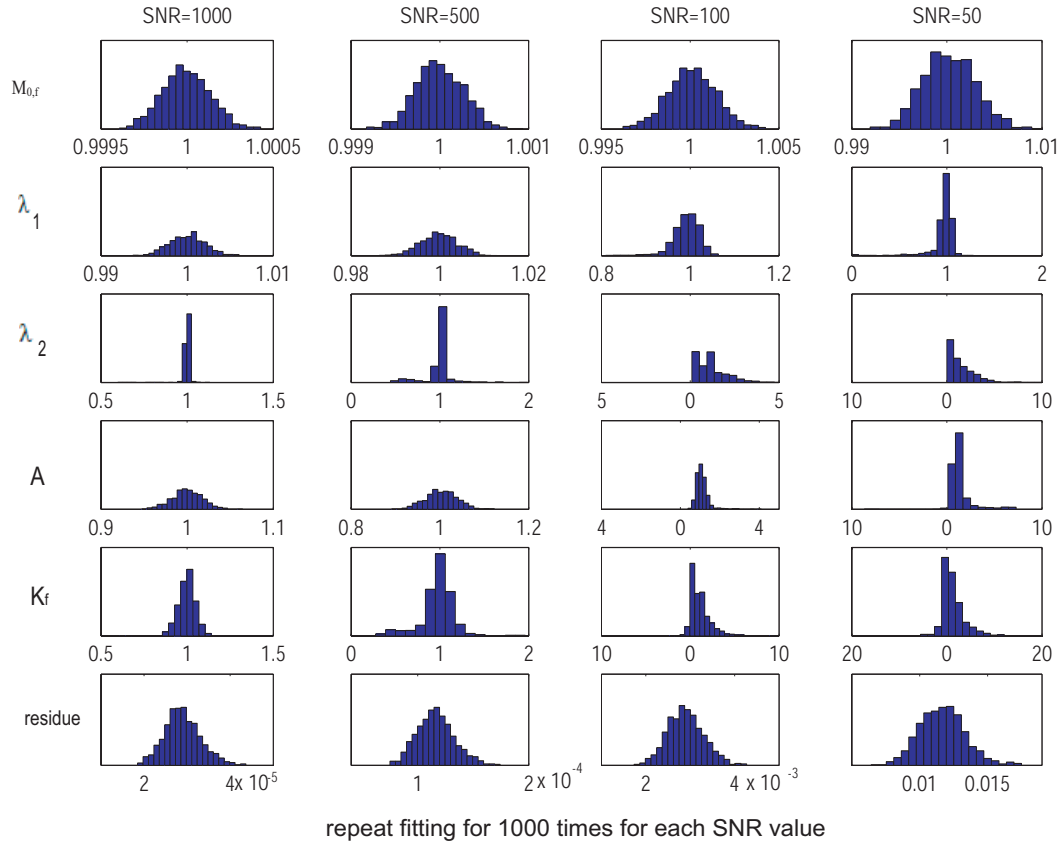

Figure 3.8: The histograms of 1000 least-squared fittings to Eq. [3.2] with different Gaussian noise sets (from left to right: SNR=1000, 500, 100, 50). For each histogram, Y axis is the count; X axis is either the residue of the fitting or the fitted QMT parameter value normalized by its true value. Acquisition parameters are 32 repetition times exponentially distributed between $TR = 5ms$ and $TR = 15s$, and three flip angles $\alpha = 40^\circ, 60^\circ, 90^\circ$. The choice of TR and α is not optimized. The mean and standard deviation for each fitted parameter for each SNR is listed in table 3.1. $M_{0,f}$ has a roughly Gaussian distribution at all SNR. The other parameters, however, have increasingly non-Gaussian distribution as the SNR drops. λ_2 is especially non-Gaussian.

Table 3.1: The mean and standard deviation of the fitted QMT parameters for five parameters fitting. When SNR=1000, all MT parameters can be determined with a relative small deviation; when SNR=500, $M_{0,f}, \lambda_1, A$ are able to be determined. When SNR<100, λ_2, A, and K_f are hard to accurately determine, but $M_{0,f}$ and λ_1 are still able to be determined.

	SNR=1000	SNR=500	SNR=100	SNR=50
$M_{0,f}(\frac{\text{fitted}}{\text{true}})$	1.0000±0.0001	1.0000±0.0003	1.000±0.001	1.000±0.003
$\lambda_1(\frac{\text{fitted}}{\text{true}})$	1.000±0.002	1.000±0.004	0.99±0.03	0.96±0.14
$\lambda_2(\frac{\text{fitted}}{\text{true}})$	1.00±0.03	0.98±0.16	1.17±0.78	1.45±1.00
$A(\frac{\text{fitted}}{\text{true}})$	1.00±0.02	1.00±0.04	1.10±0.31	1.38±0.91
$K_f(\frac{\text{fitted}}{\text{true}})$	1.00±0.06	0.98±0.21	1.11±1.04	1.39±1.77

As we demonstrated in the numerical testing, signal Eq. [3.2] can be simplified to Eq. [3.3] with appropriate approximations. The steady state signal calculated by Eq. [3.3] is almost the same as the signal calculated by Eq. [3.2] with the difference smaller than 0.1% of the equilibrium magnetization when calculated with parameters typical of white matter. Equation [3.3] is a function of two experimental parameters (TR, α) and three MT parameters ($M_{0,f}, \lambda_1, A$). Therefore, we can also use Eq. [3.3] to determine $M_{0,f}$, $R_1^{obs}(=\lambda_1)$ and A. The analytically generated steady state data (with white Gaussian noise) from Eq. [3.2] was also fitted to Eq. [3.3]. The results are plotted in figure 3.9 and shown in table 3.2.

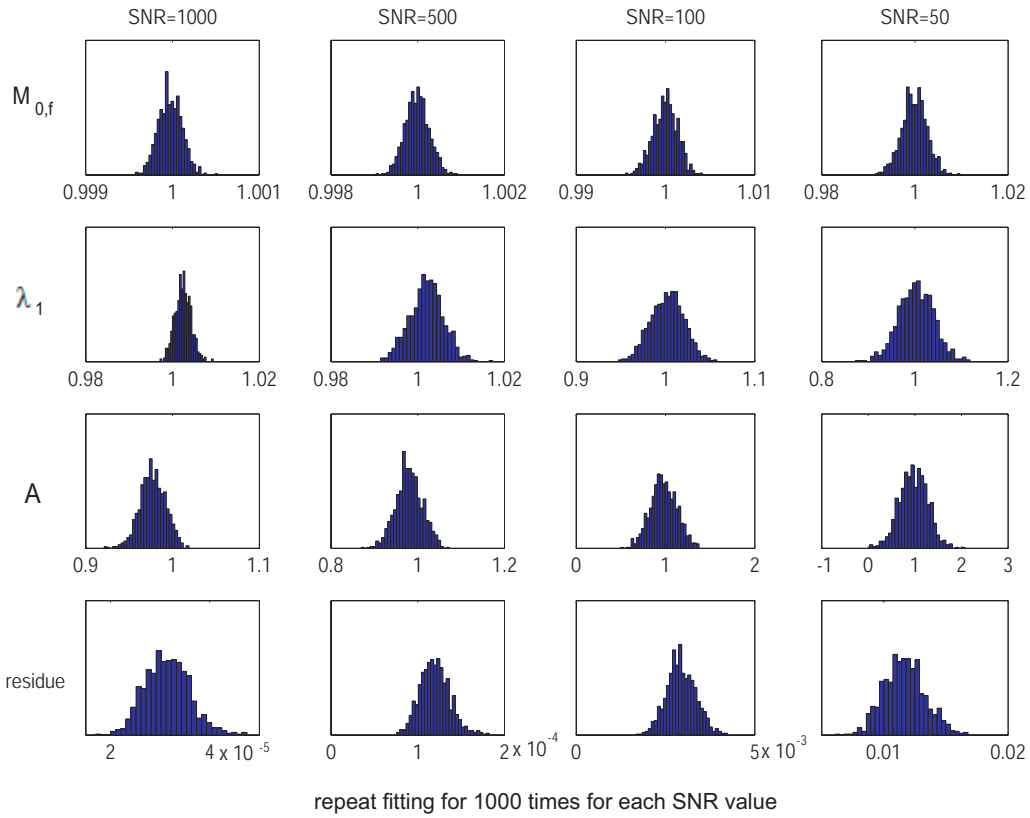

Figure 3.9: The histograms of 1000 least-squared fittings to Eq. [3.3] with different Gaussian noise sets (from left to right: SNR=1000, 500, 100, 50). For each histogram, Y axis is the count; X axis is either the residue of the fitting or the fitted QMT parameter value normalized by its true value. Acquisition parameters are the same as five parameters fitting: 32 repetition times exponentially distributed between $TR = 5ms$ and $TR = 15s$, and three flip angles $\alpha = 40^{\circ}, 60^{\circ}, 90^{\circ}$. The mean and standard deviation for each fitted parameter for each SNR is listed in table 3.2. All of the resulting fitted parameters have a roughly Gaussian distribution, reflecting the greater robustness in fitting those data to Eq. [3.3] in comparison to Eq. [3.2].

Table 3.2: The mean and standard deviation of the fitted QMT parameters for three parameters fitting. It was found that $M_{0,f}$ and λ_1 can be reasonably determined for any case when SNR is not less than 50; A can be reasonably determined when SNR is around 500 or more. The systematic error on the parameters estimation caused by the approximation from Eq. [3.3] to Eq. [3.2] is very small: the resulting A is about 2% smaller than the true value, and the resulting λ_1 is about 0.2% higher than the true value.

	SNR=1000	SNR=500	SNR=100	SNR=50
$M_{0,f}(\frac{\text{fitted}}{\text{true}})$	1.0000±0.0001	1.0000±0.0003	1.000±0.001	1.000±0.003
$\lambda_1(\frac{\text{fitted}}{\text{true}})$	1.002±0.002	1.002±0.004	1.00±0.02	1.00±0.04
$A(\frac{\text{fitted}}{\text{true}})$	0.98±0.02	0.98±0.03	0.98±0.15	0.97±0.31

In summary, fitting gradient echo steady state data to either Eq. [3.2] or Eq. [3.3] can potentially determine MT parameters; the preciseness of the fitting results depends on the sample parameters, the repetition times and flip angles chosen, and the signal to noise ratio of the data. For the work in this chapter, we are limiting ourselves to sample parameters typical for white matter, and to non-optimized acquisition parameters. Under these conditions, if we are only interested in the determination of the equilibrium magnetization $M_{0,f}$ and the slow recovery rate λ_1 (equals the observed recovery rate R_1^{obs}), then SNR=50 is good enough for determining the parameters with uncertainty less than 5%, when fitting data to Eq. [3.3], an approximation with fewer free parameters; if we are also interested in the determination of A to the same level of uncertainty, then SNR~500 is required, and we can choose either Eq. [3.2] or Eq. [3.3] as the fitting

function; if we want to accurately determine every QMT parameter including the fast recovery rate λ_2 and the exchange rate K_f, then SNR>1000 is required, and Eq. [3.2] is the fitting function.

QMT parameters determination for experimental data

To test the applicability of fitting measured gradient echo steady state data to our signal equations to determine QMT parameters, the same three samples and gradient echo pulse sequence were used to acquire data. 42 steady state gradient echo images were acquired with three excitation angles $\alpha = 40^\circ, 60^\circ, 90^\circ$ and 14 repetition times:

$TR = 0.06, 0.08, 0.1, 0.2, 0.3, 0.5, 0.6, 0.8, 1, 2, 4, 5, 8, 15s$ (The choice of TR and α is not optimized)

In this experiment, we employed a 1.5 ms sinc pulse to excite a 2mm slice. Since the sinc pulse does not have an infinite width, the resulting slice profile is not an ideal rectangle, and Eq. [3.2] is modified to include signal variation:

$$M_{xy,f,MTss} = \int M_{0,f} \frac{(1-E_1)(1-E_2S_r) + A(1-S_r)(E_1-E_2) - \frac{K_f}{\lambda_2-\lambda_1}(1-S_r)(E_1-E_2)}{(1-E_1\Psi_{\cos}(z,b_1,\alpha_{input}))(1-E_2S_r) + A(\Psi_{\cos}(z,b_1,\alpha_{input})-S_r)(E_1-E_2)} \Psi_{\sin}(z,b_1,\alpha_{input})dz \quad [3.6]$$

Where $\Psi_{\cos}$ and $\Psi_{\sin}$ are functions yield by the slice position in the z direction, the b_1 correction factor, and the input excitation angle. $\Psi_{\cos}$ and $\Psi_{\sin}$ are M_z and M_y, respectively, after a single pulse as determined by numerically simulating the Bloch Equations with the appropriate RF pulse shape and gradients and smoothing the effects of the discrete definition of pulse shape. We performed the numerical simulation and

created a $\Psi_{\cos}$ lookup table and a $\Psi_{\sin}$ lookup table. During the least-squared fitting, $\Psi_{\cos}$ and $\Psi_{\sin}$ values were interpolated from a pre-calculated table of 101 z (uniformly distributed in the 2mm thick slice with $20\mu m$ intervals) and 501 α values (uniformly distributed between 10° and 110° with 0.2° intervals). We fit the signal at each pixel to Eq. [3.6] to determine $M_{0,f}, \lambda_1, \lambda_2, A, K_f$, and b_1.

With the same approach, we rewrote signal Eq. [3.3] to:

$$M_{xy,f,MTss} = \int M_{0,f} \frac{1-E_1}{(1-E_1\Psi_{\cos}(z,b_1,\alpha_{input}))+A(\Psi_{\cos}(z,b_1,\alpha_{input})-S_r)E_1}\Psi_{\sin}(z,b_1,\alpha_{input})dz \qquad [3.7]$$

The experimental data were also fitted to Eq. [3.7] to determine $M_{0,f}, \lambda_1, A$, and b_1.

To provide a separate measure of the observed recovery rate R_1^{obs} and the pool size ratio F, we also performed a selective inversion recovery experiment. A 180^o inversion pulse followed by a conventional spin echo pulse sequence with TR = 10 s, TE = 10 ms, and TI ranging from 6 ms to 9.8 s was used. The measured data was fitted to a bi-exponential function to determine MT parameters (36).

The signal to noise ratio for each pixel in our MT parameters determination experiment was about 500. We fitted the steady state signal to Eq. [3.6] pixel by pixel. The fitted λ_2 and K_f values were inconsistent from pixel to pixel and the averages were skewed by outlying results. This lack of fitting robustness is qualitatively consistent with the simulation results (figure 3.8). In distinction, the fits to Eq. [3.6] for $M_{0,f}, A$, and R_1^{obs} were robust, also in agreement with the simulations. Figure 3.10 shows the fit to Eq. [3.6] for data from one pixel in the $BSA + MnCl_2$ sample. Figure 3.11 shows the resulting map of A. The pool size ratio was calculated pixel by pixel from $F = A/(1-A)$. As an

alternative approach, we also fitted the experimental data to Eq. [3.7] to determine the parameters $M_{0,f}$, A, and R_1^{obs}. Table 3.3 compares the measured parameters for the two fitting methods for the three samples. The MT parameters measured from the separate selective inversion recovery experiment are also listed for comparison.

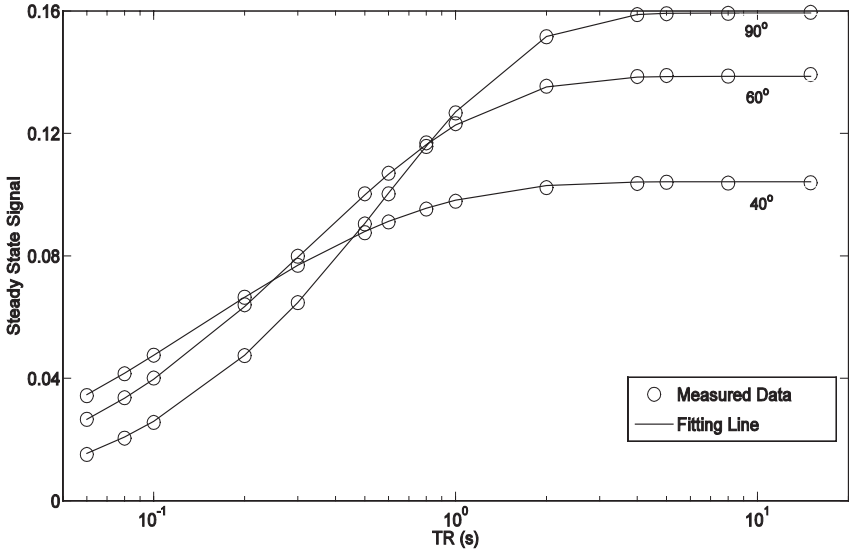

Figure 3.10: Fit the experimental data to Eq. [3.6] for one pixel in the $BSA + MnCl_2$ sample: the fitting lines match well with the gradient echo steady state data.

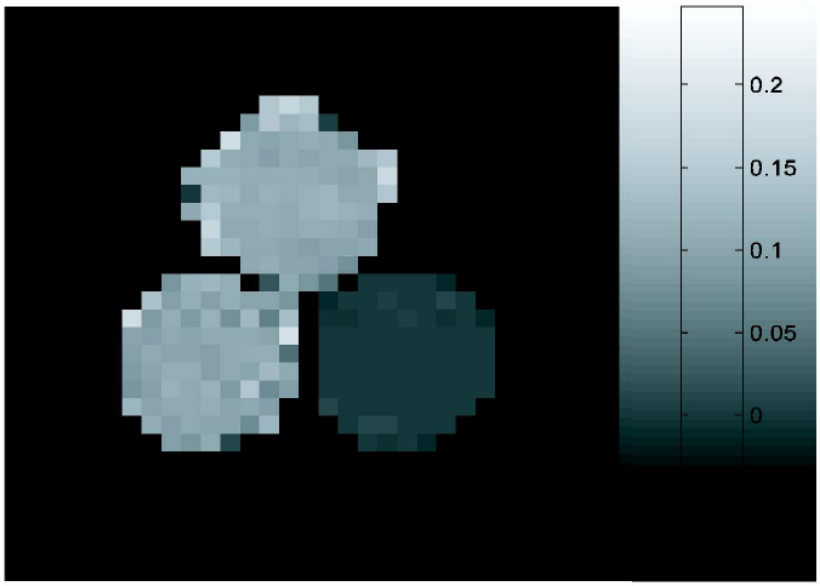

Figure 3.11: The parameter A map for $MnCl_2 + BSA$ (top), BSA (left bottom), and $MnCl_2$ (right bottom).

Table 3.3: The measured slow recovery rate and pool size ratio from the gradient echo method (both five parameters and three parameters fittings) and the selective inversion recovery method. The mean and standard deviation of each parameter are determined by averaging all non-edge pixels in the sample.

		five parameters fitting	three parameters fitting	Inversion recovery method
BSA+ $MnCl_2$	F	0.11±0.01	0.09±0.03	0.09±0.01
	$R_1^{obs}\ (s^{-1})$	1.41±0.03	1.43±0.04	1.38±0.03
BSA	F	0.11±0.02	0.10±0.04	0.09±0.01
	$R_1^{obs}\ (s^{-1})$	0.57±0.01	0.58±0.01	0.57±0.01
$MnCl_2$	F	0.000±0.001	0.02±0.02	-0.005±0.005
	$R_1^{obs}\ (s^{-1})$	2.56±0.04	2.52±0.06	2.46±0.03

From the gradient echo experiment results, the $MnCl_2$ sample has a zero pool size ratio, the 15% $BSA+MnCl_2$ and 15% BSA sample have different recovery rates but similar pool size ratios. These results confirm that our gradient echo method is able to separate MT from relaxation effects.

For the BSA and $BSA+MnCl_2$ samples, the pool size ratios measured by the gradient echo method are slightly different from the pool size ratios measured by the selective inversion recovery method. This is not surprising, since both methods determine the pool size ratio only to first order in $1/K_r$. For the $MnCl_2$ sample, the measured pool size ratios from both methods are the same: $F \approx 0$, which is expected for samples with no MT effects.

The slow recovery rates (R_1^{obs}) determined via the gradient echo steady state signal when including the effects of MT agree with those derived from the selective inversion recovery experiment. The standard deviations of R_1^{obs} measured by gradient echo experiments are also similar to those measured by the selective inversion recovery experiment (35,36), though since neither method was optimized, such comparisons are not very meaningful. The total acquisition time (not optimized) for the QMT parameters determination is about 2 hours. However, if we are only interested in the determination of R_1^{obs}, it may be possible to make the measurement more time efficient by optimizing the choices of TR and α, and minimizing the number of dummy scans.

While we correct for spatial variations in the flip angle and for imperfections in the slice profile, one systematic error that we ignore is RF power variations that are nonlinear with

the programmed flip angle. The nonlinear RF field effect can not be corrected by the linear b_1 correction factor. The magnitude and region of this problem are very system dependent. In our experiments, we chose the flip angles and pulse durations such that the nonlinearity is minimized, as determined by additional system performance test (data not shown). Another possible source of error is miscalibration of the slice select refocusing gradient. While the refocusing gradient is tuned separately for each flip angle, the uncertainty of this tuning may cause an error in some resulting MT parameters. For example, we found that a 1% deviation of the tuned refocusing gradient (which roughly equals the uncertainty in our experiments) results in almost no deviation on the fitted λ_1 but approximately 10% deviation on the fitted A.

3.4. Conclusions

As a summary for the experiments we have done to investigate MT effects in single slice gradient echo imaging, we used a 600 μs hard pulse for non slice-selective pulse sequences, a 1.5 ms sinc pulse with flip angles not larger than 90° for slice-selective pulse sequences. In both cases, the power of the RF pulses were in a region that was very linear for the amplifier. We also used a b_1 correction factor to compensate for power miscalibration and the B_1 variation between pixels. Furthermore, for slice-selective pulse sequences, we included slice profile effects in our analysis. The combination of these techniques allows us to accurately model the gradient echo steady state data as a function of the sequence repetition time and RF flip angle. By doing that, we were able to

show that T_1 quantification is incorrect if MT effects are ignored, and that, for BSA, this error is on the order of 10%. On the other hand, after including MT effects in the data analysis, we were able to accurately quantify T_1 via the gradient echo method. In addition, we were able to obtain a quantitative MT parameter, the pool size ratio, for each sample. The use of this QMT method in vivo needs further investigation, which includes the optimization of the choice of TR and α to maximize the MT effects and to perform the experiment in a clinically applicable time. Though the requirements of high SNR make it difficult to accurately determine the pool size ratio in clinical studies, this method may prove well suited for accurate T_1 determination in vivo.

CHAPTER IV

APPLICATIONS OF QMT IMAGING: SENSITIVITY TO MYELIN AS REVEALED BY IMAGING SHIVERER MICE

We have discussed the determination of QMT parameters by a various approaches in Chapter 2 and Chapter 3, now this question arises: how can we take use of these QMT parameters? Specifically, why not save all of those efforts in the QMT model building and parameters determination, but just use conventional and much easier MRI methods, such as T_1, T_2, or proton density weighted imaging? Part of the answer can be found in previous chapters where the application of QMT is briefly addressed. In this chapter and the following two chapters, a few projects to reveal the uniqueness and importance of QMT method in pre-clinical small animal central nervous system (CNS) imaging will be discussed.

Unlike the wide aspects of MT applications, the applications of QMT are extensively focused on myelin imaging. The great sensitivity and specificity of QMT to myelin have been realized by more and more scientists. A myelin imaging conference was held in Feb 2006 at Vancouver, Canada. The importance of developing an efficient myelin marker, and the current status of myelin imaging were extensively discussed. It was suggested by most attendees that the magnetization transfer imaging (including quantitative magnetization transfer), the diffusion tensor imaging (DTI), and the multiple exponential T2 spectrums technique (MET2) are probably three of the best myelin imaging methods.

(The basic theory for the last two methods is briefly introduced in the appendix of this dissertation.) Specifically speaking, the pool size ratio in the QMT method, the radial diffusivity in the DTI method, and the myelin water fraction in the MET2 method, are suggested to be the three of the best non-invasive myelin markers currently.

This chapter will begin with an introduction of myelin and myelin related diseases, then the sensitivity of QMT measurements to myelin will be discussed with a detailed example: shiverer mice brain imaging. DTI and histological studies will also be performed and correlated to show that the QMT measured pool size ratio is a non-invasive marker with great sensitivity to myelin.

4.1. Myelin and Myelin Related Diseases

Brain and Spinal cord consist of human's central nervous system (CNS). In CNS, Neuron is the most important types of cells, which processes and transmits neural information. The major components of a neuron include a long axon fiber and its surrounding myelin sheath. Figure 4.1 is a picture from Wikipedia to show the structure of a typical neuron. Figure 4.2 is a transmission electron micrograph of myelinated neuron generated at Trinity College, Hartford, CT.

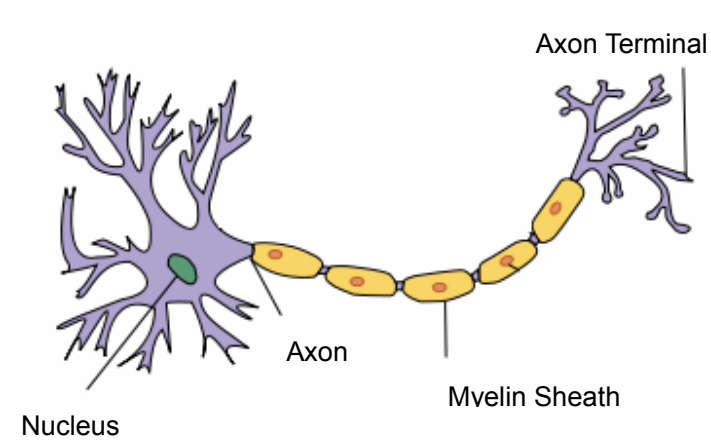

Figure 4.1: The structure of a typical neuron.

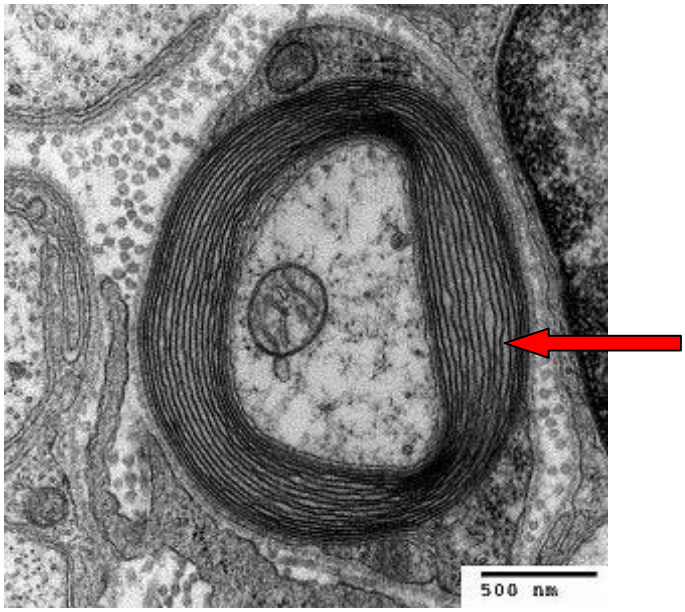

Figure 4.2: Transmission electron micrograph of myelin.

The main consequence of myelin sheath is an increase in the speed at which impulses propagate along the axon fiber. Myelin sheath also helps prevent the electrical current from leaving the axon. The loss or absence of myelin may cause the slowing down of

neural signal transfer and therefore cause various symptoms. Myelin related diseases including demyelination diseases and dysmyelination diseases. Demyelination is the act of demyelinating, or the loss of the myelin sheath insulating the nerves. It is the hallmark of many white matter diseases. The most common example is Multiple Sclerosis (MS). Dysmyelination is characterized by defective structure and function of myelin sheaths, usually arise from genetic mutations. Examples include leukodystrophies and schizophrenia.

4.2. Myelin Imaging on Shiverer and Control Mice

Introduction

QMT parameters have been measured in normal brains and different disease models to investigate the sensitivity to myelin. QMT measurements showed that pool size ratios are greater in white matter than in gray matter (50), and smaller in MS lesions than in normal white matter (32), suggesting that pool size ratio is capable of reflecting myelin contents. In addition, normal appearing white matter (NAWM) in MS patients were studied by both MTR and QMT, and the results indicate that QMT measured pool size ratio has a greater sensitivity in detecting myelin loss (33). Diffusion tensor imaging is also widely used in white matter diseases studies. While the summary parameters such as the apparent diffusion coefficient, the relative anisotropy, and the fractional anisotropy are reported to be different between MS lesions and normal white matter regions (51-53), none of these measures are capable of differentiating between the underlying axonal injury and

demyelinantion. In contrast, the DTI derived directional diffusivities have demonstrated much improved specificity. For example, DTI on mouse central nervous system have shown that the radial diffusivity (perpendicular to the axon fibers) is capable of detecting the presence of damage to myelin sheath in white matter, and the axial diffusivity (parallel to the axon fibers) detects the presence of injured axons in white matter (54-58). Since both QMT and DTI may be capable of detecting myelin damage, imaging using both modalities on the same sample would provide confirmation of the myelin sensitivity, allow comparisons between the methods, and is potentially beneficial for the development of optimized myelin marker.

In this study, myelin pathology was generated by a dysmyelination animal model, the genetically myelin shiverer mouse, which lacks the myelin basic protein (MBP). Shiverer mouse is characterized by the absence of the major dense line (MDL). The myelin sheath in the central nervous system is very thin, loose, or completely absent in most cases (59,60). On the other hand, there is no axon degeneration or inflammation in shiverer mouse (61). Therefore, shiverer mouse comparing with control mouse provides an excellent model to estimate the sensitivity of MR techniques on myelin. Previous studies have used this animal model to asses the sensitivity and specificity of DTI (56). This work will perform a similar analysis of the SIR-FSE QMT method and compare the results with DTI.

Theory

SIR-FSE QMT pulse sequence is used for QMT studies. The details of this method are discussed in Chapter 2. In general, SIR-FSE uses a fast spin echo pulse sequence with a preceding 180 degree inversion pulse. A series of inversion times are used to model the transient signal of the magnetization recovery after the inversion pulse. A constant pre-delay time t_d (the time delay after the fast spin echo acquisition in each repetition), instead of a constant repetition time *TR*, is used to maximize the efficiency of SIR-FSE (36). By fitting the measured transit signal of magnetization recovery for different inversion times to Eq. [2.4], the slow and fast recovery rates can be obtained, and the pool size ratio can be calculated from Eq. [2.8].

The derivation of DTI parameters are discussed in Appendix A. In general, Diffusion tensor (**D**) can be derived according to Eq. [A.2], where S is the diffusion-weighted signal, S_0 is signal with diffusion weighting factor $b = 0$, and **n** is the encoding directions (62). The resulting tensor element maps are used to derive eigenvalues ($\lambda_1, \lambda_2, \lambda_3$) of the diffusion tensor by matrix diagonalization. The quantitative indices including axial diffusivity ($\lambda_{\square}$), radial diffusivity ($\lambda_{\perp}$), and relative anisotropy (RA), can be derived from equations [A.3]-[A.5].

Methods

Six shiverer and six control mice were euthanized and perfused with phosphate-buffered saline (PBS) followed by 10% formalin/PBS solution through the left cardiac ventricle.

The mice were decapitated and their heads were kept in 10% formalin/PBS solution and stored at 4^{o}C for one week. Before imaging, each mouse head was transferred to a 10mm diameter cylinder filled with PBS solution.

Cylinders with fixed mouse head were placed in a 1cm inner diameter solenoid coil which serves as both RF transmitter and receiver. The mid-sagittal slice of each brain was acquired in a 4.7T Varian UNITY INOVA spectrometer with an actively shielded Magnex gradient coil (10 cm inner diameter, 60 G/cm, 100 μs rise time). A fast spin echo sequence with a 1 ms sinc inversion pulse was used for the QMT experiments. 18 images with the inversion times ranging from 5 ms to 7.9 s were obtained with 2 s constant pre-delay t_d, 8 averages, 16 echoes, 10 ms echo spacing time, 25 mm by 25 mm field of view, 0.8 mm thick slice, and 256x256 data matrix. The total imaging time was 2 hours. Data were fitted to the bi-exponential function of the inversion times (Eq. [2.4]) to determine QMT parameters pixel by pixel. Diffusion tensor imaging was performed on the same selected slices with the same spatial resolution with 1 s repetition time, 4 averages, 38 ms echo time, 13 ms time between gradient pulses, 4 ms diffusion gradient duration, b value of 1.879 ms/μm^2, diffusion sensitizing gradients along six directions, plus a normalizing image with no diffusion gradients. The DTI scan time was 2 hours. DTI parameters were calculated from the eigenvectors pixel-by-pixel.

For each QMT and DTI parameter, statistically significant difference between control mice and shiverer mice was evaluated by student t-test. The t value was calculated by the means and standard deviations of each parameter in control/shiverer mice. With the

t-value and the known degree of freedom (6 control mice and 6 shiver mice gave a degree of freedom equals 10), the probability (p-value) that each parameter is the same in control mice as in shiverer mice was determined.

For examining myelin integrity, the slices matching the DTI and QMT images were cut from paraffin embedded tissue and cleared in xylene. The primary antibody detecting myelin basic protein (MBP, 1:100; Zymed laboratories Inc., South San Francisco, CA) was revealed by avidin-biotin-peroxidase method (Vector Laboratories, Inc. Burlingame, CA 94010). The distribution of axons was stained using a primary antibody to phosphorylated neurofilament (pNF, SMI-31, 1:500; Sternberger Monoclonals, Lutherville, MA) with reactivity revealed by the avidin-biotin-peroxidase method (Zymed Laboratories). Images were captured with a Photometrics CCD digital camera using MetaMorph image acquisition software (Universal Imaging Corporation, Downington, PA) on a Nikon Eclipse 80i microscope. The histology study was performed by the collaborating research group led by Dr. Sheng-Kwei Song in Washington University in St. Louis.

Results

Representative QMT, DTI, and immunohistochemistry maps for a mid-sagittal slice of one control and one shiverer mice are presented to demonstrate the consistent findings among different methods (Fig. 4.3). Significantly reduced intensity in pool size ratio map and the markedly reduced contrast in radial diffusivity map are in close agreement with

the loss of the intensity of red immunohistochemical staining of MBP when comparing the corpus callosum from the shiverer with that of the control mice.

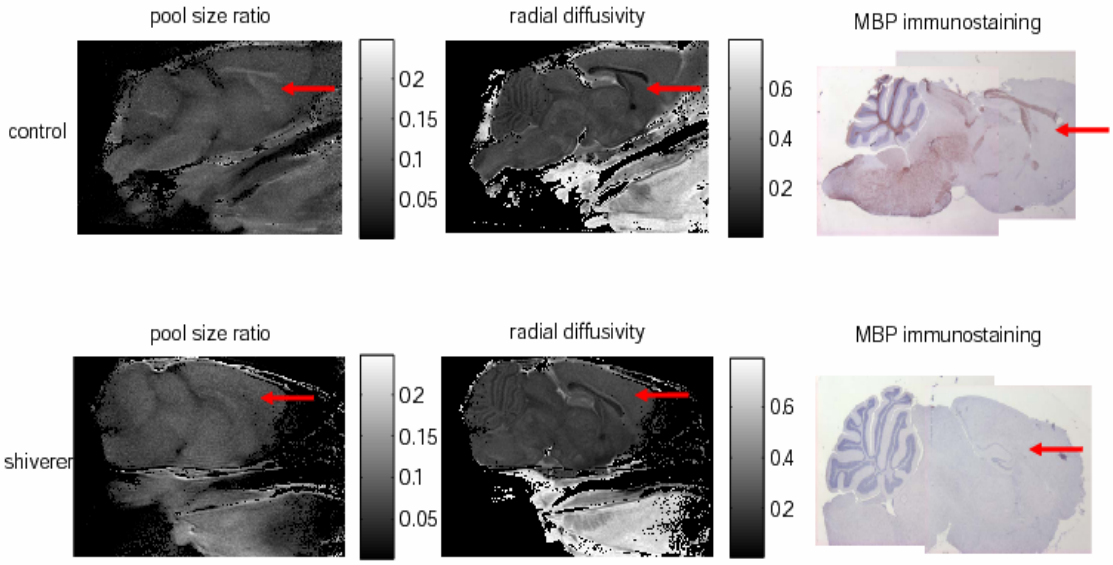

Figure 4.3: The pool size ratio (left), the radial diffusivity (center), and the MBP staining (right) for the control (top row) and shiverer mice (bottom row) are compared. The red arrow inside each image points to the corpus callosum in the mouse brain. Also generated but not showing above are the relative anisotropy maps, which have the most contrast between the corpus callosum and the surrounding gray matter, and were used to choose the white/gray matter ROIs. In the QMT and MBP maps, the corpus callosum is visible for the control, but not for the shiverer mouse.

Data from the SIR-FSE pulse sequence were fitted to the bi-exponential Eq. [2.4] and QMT parameters were calculated pixel-by-pixel from Eq. [2.8]. The resulting pool size ratio, fast recovery rate, and slow recovery rate of both white and gray matter ROIs of each individual mouse were averaged and listed in table 4.1.

Figure 4.4 shows the comparison of the pool size ratio between the white and gray matter

for the six control and six shiverer mice. The pool size ratio of control mice white matter is about 30% higher than that of gray matter; the pool size ratio of shiverer mice white matter is almost the same as that of gray matter. In addition, as shown in figure 4.5, the white matter pool size ratio of control mice is about 25% higher than the white matter pool size ratio of shiverer mice ($p=0.002$); the pool size ratio of gray matter is roughly the same (~5% difference, smaller than the uncertainty scale; $p=0.14$) for both control and shiverer mice.

There is nearly no difference ($p=0.58$) for the white matter fast rates when comparing the control and shiverer mice. No gray matter fast rates difference ($p=0.98$) between the control and shiverer mice as well. The white matter slow rate is slightly higher than the gray matter slow rate for the control mice, while the slow rate is higher in the gray matter and lower in the white matter for the shiverer mice. There is about 8% difference ($p=0.0002$) of slow rates between control and shiverer mice white matter, and no difference ($p=0.52$) of slow rates between control and shiverer mice gray matter.

Table 4.1: Calculated QMT and DTI parameters for respective ROIs. We chose the whole corpus callosum (50-70 pixels, without boundary pixels) as the ROI of white matter, and chose a rectangle (about 50-70 pixels) in the cortical gray matter superior to the corpus callosum as the ROI of gray matter (The positioning of those ROIs were based on the relative anisotropy maps which have the most contrast between white and gray matter). The p -value represents the statistically significant difference calculated by t-test.

			Control Mice (mean ± SD)	**Shiverer Mice (mean ± SD)**	**p-value**
QMT	Pool Size Ratio	White matter	0.099±0.011	0.076±0.008	0.002
		Gray matter	0.071±0.005	0.076±0.007	0.14
	Fast Rate (s^{-1})	White matter	27±4	29±8	0.58
		Gray matter	29±8	28±6	0.98
	Slow Rate (s^{-1})	White matter	1.10±0.03	1.02±0.02	0.0002
		Gray matter	1.05±0.04	1.07±0.05	0.52
DTI	Radial Diffusivity ($\mu m^2 / ms$)	White matter	0.09±0.01	0.12±0.02	0.01
		Gray matter	0.23±0.01	0.24±0.02	0.78
	Axial Diffusivity ($\mu m^2 / ms$)	White matter	0.40±0.03	0.42±0.04	0.27
		Gray matter	0.31±0.02	0.31±0.03	0.91

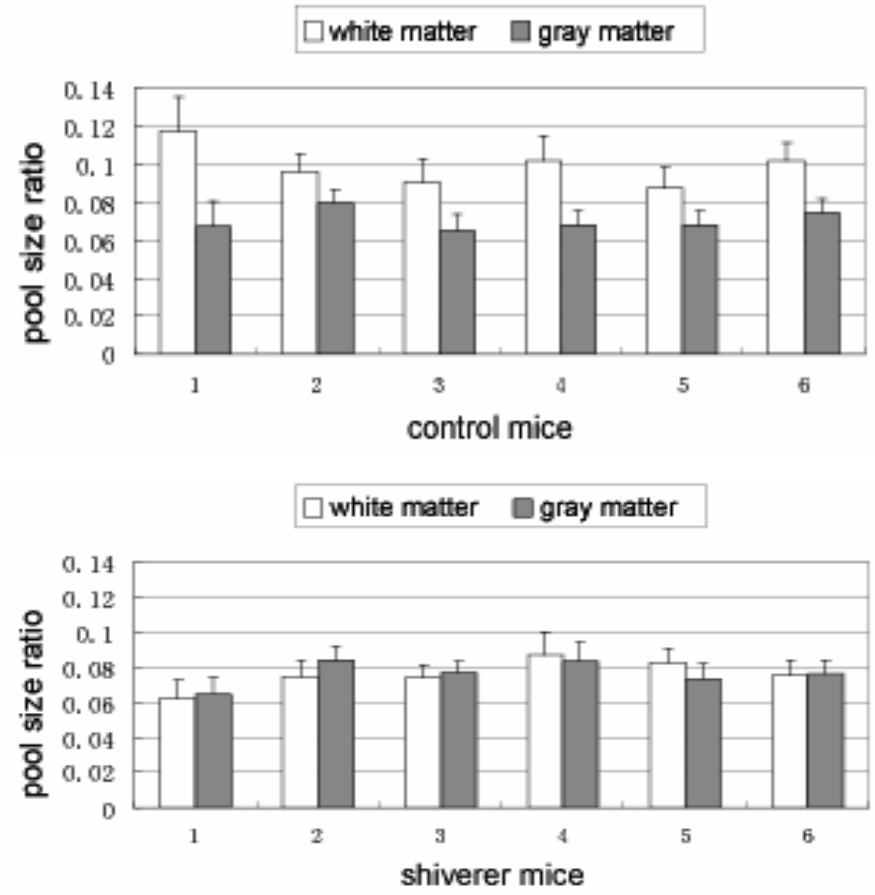

Figure 4.4: The comparison of the pool size ratio in the white matter to that in the gray matter. The plot on the top is for control mice, the plot on the bottom is for shiverer mice.

Diffusion weighted images data were analyzed to derive the relative anisotropy and directional diffusivity maps. The RA maps were used to choose ROIs manually for all diffusion and quantitative magnetization transfer parameters determination. The resulting radial diffusivities and axial diffusivities are listed in table 4.1. As shown in figure 4.5, the radial diffusivity in the control mice white matter is about 25% less than that in the shiverer mice white matter ($p=0.01$); The axial diffusivity in the control mice white matter is almost indistinguishable (about 5% difference, smaller than the uncertainty

scale; p=0.27) from that in the shiverer mice white matter; The diffusivities in the gray matter is always about the same for control and shiverer mice (radial: p=0.78; axial: p=0.91).

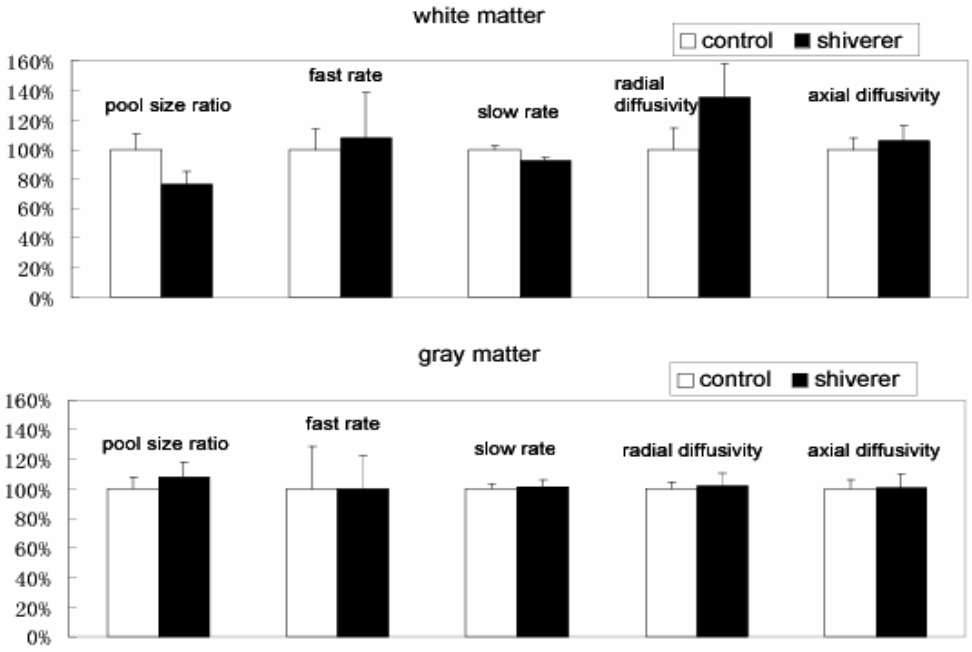

Figure 4.5: The percentage difference of QMT and DTI parameters between control mice and shiverer mice. The parameters for control mice were set to 100%.

Quantitative analysis of immunohistochemistry studies are shown in figure 4.6. The MBP positive axons were counted for each white matter tract in a blinded fashion. Specifically, images were magnified 4 times (zoom-in) using MetaMorph, and the positively stained axons were counted through the whole image (about $150\mu m \times 110\mu m$). Significantly myelinated axon count is found in control mice but not in shiverer mice.

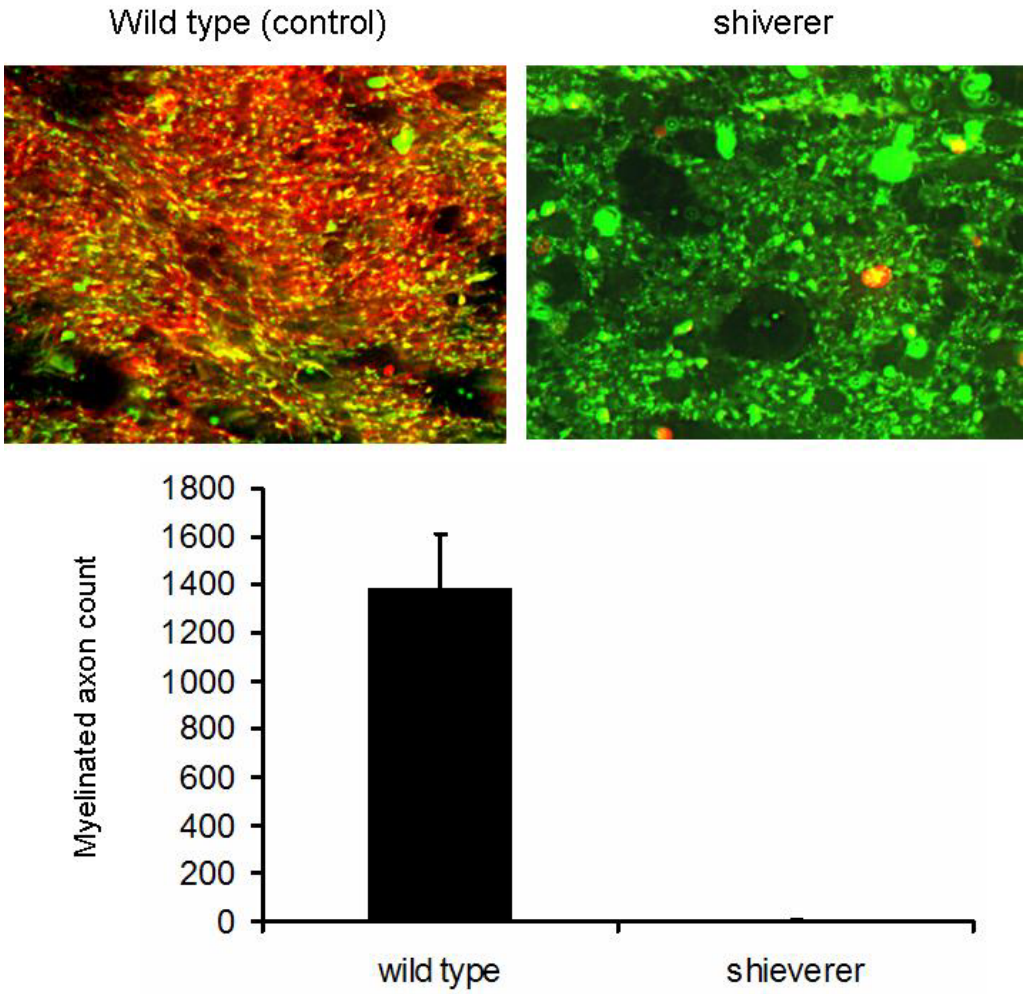

Figure 4.6: Quantitative analysis of immunohistochemistry (for 3 control mice and 3 shiverer mice). Top two images show the MBP (red) and pNF (green) staining results for mice corpus callosum, bottom plot show that the myelinated axon count in the shiver mice corpus callosum is nearly absent.

Discussions

Shiverer mouse is a known model of dysmyelination (59,60). It was found that our QMT measured pool size ratio is a valid maker for non-invasive evaluation of myelin in shiverer mouse brain. The measured pool size ratio in the control mice white matter (corpus callosum) is much higher (about 25%) than that in the shiverer mice white matter,

while the pool size ratio in the control mice gray matter is similar to the pool size ratio in the shiverer mice gray matter, indicating that the difference in the pool size ratio is caused by the difference of myelin integrity. Likewise, the resistance of water diffusion in the perpendicular direction of axon fibers is strongly affected by the surrounding myelin sheath, and published results (55,56) suggest that the radial direction diffusivity is capable of myelin detection. In our experiments, we found that the radial diffusivity in the control mice white matter is much less (about 25%) than the radial diffusivity in the shiverer mice white matter, and there is no difference for the radial diffusivity in the gray matter. These DTI results correlate very well with the QMT results. Note that the similar percentage difference in the pool size ratio and radial diffusivity between control and shiverer mice white matter suggests that both parameters are linearly sensitive to the same underlying phenomenon, in this case, dysmyelination. The difference (about 8%) in the observed recovery rate (slow recovery rate, the reciprocal of conventional T_1) between control and shiverer mice white matter is much smaller than the difference we observed in QMT and DTI parameters, suggesting that both QMT and DTI are superior to T_1 weighted images or T_1 maps in terms of sensitivity to myelin. While we don't have a quantitative estimation of myelin in the histological studies, the MBP immunostaining images showing the myelin presence in control mice white matter but not in shiverer mice white matter support our QMT and DTI results.

While the lipids in myelin are a conduit for spin exchange between the free water and macromolecules (23,24), myelin is not the only microstructure in the mouse brain that

contributes to the pool size ratio. Gray matter does not have significant myelin, but still has a non zero pool size ratio. However, the lack of gray/white matter contrast in the pool size ratio map of the shiverer mouse in figure 4.3, and the corresponding values listed in table 4.1, support the view that it is myelin alone that accounts for the pool size ratio difference between gray and white matter in normal mice. That is, our findings indicate that microstructures other than myelin (ie. Axon fibers) in the white matter have similar QMT properties as microstructures in gray matter. On the other hand, myelin is not the only reason that gray and white matter have different radial diffusivities. Shiver mice white matter has no myelin but only has half the radial diffusivity of gray matter (Table 4.1). That is, even without myelin, white matter and gray matter are differentiated by radial diffusivity, but not the pool size ratio. One possible practical benefit of this effect is that a pool size ratio map may indicate demyelinated white matter regions without requiring knowledge of normal white matter values.

The fast recovery rate and the slow recovery rate of mice brains were also obtained from QMT results (table 4.1). The fast recovery rate, which is approximately equal to the MT exchange rate from the macromolecular protons to free water protons, is not differentiated between the control and shiverer mice. This result is similar to the result of a QMT study of demyelinated sciatic nerve (63), in which the exchange rate appeared to be independent of demyelination. The slow recovery rate, which is the reciprocal of the apparent T_1 relaxation time, is higher in control mice white matter than that in the dysmyelinated shiverer mice white matter, also in agreements with previous results in

peripheral nerves (63). However, the differences in these parameters between white and gray matter are relatively small, likely due to the relative insensitivity of these parameters to myelin and possibly fixation effects as discussed below. The axial diffusivity in white matter is not changed between control and shiverer mice, which agrees well with previous results (55,56), and indicates that axon fibers are still intact in shiverer mice. Furthermore, both axial and radial diffusivities in gray matter are also very similar in control and shiverer mice. These results are expected for our animal model, since the only difference between control and shiverer mice is the myelin sheath in white matter, and there is no substantial structural difference for gray matter.

We have demonstrated that both QMT and DTI are capable of characterizing myelin content in mice brain. Also determined but not shown is that these results do not change when we measured the same sample at two weeks after perfusion (comparing to measurements at one week after perfusion), indicating that our one week formalin/PBS fixation procedure was sufficient to reach a steady-state condition. Published results suggest that the directional diffusivities *ex vivo* are smaller than those *in vivo*, but measures of anisotropy do not change (64). Our DTI results are consistent with these *ex vivo* results. Exclusive comparisons of QMT parameters on the same sample before and after fixation are not available in published literatures. We also do not have a direct comparison of *ex vivo* and *in vivo* QMT parameters on the same animal model. Nevertheless, our *ex vivo* QMT results in this study differ from *in vivo* measurements in ferret brain acquired using the same pulse sequence (36). The *ex vivo* results for white

matter have a larger fast recovery rate, a smaller pool size ratio, and a larger slow recovery rate. The results for gray matter show no change in the fast recovery rate, a larger pool size ratio, and a larger slow recovery rate. The increasing of slow recovery rates (which are the reciprocals of the T_1 relaxation times) in both white matter and gray matter agrees with published results of fixation effects (65,66). In all cases, the *ex vivo* QMT results have smaller parameter difference between gray and white matter than their *in vivo* counterparts, likely due to fixation effects overwhelming inherent tissue characteristics. Changes due to field difference (4.7T vs 9.4T) and animal difference (mice vs ferrets) may also play a role.

Many quantitative measurements by MRI are sensitive to myelin. However, other biological microstructures (such as axon fibers) also affect most of those measurements. Multiple contrast MRI experiments were used by many researchers to investigate the specificity of certain MRI parameters to myelin. For example, multi-component T_1 and T_2 measurements were performed together with MTR measurements to show that the change of MTR cannot be attributed solely to the change of myelination (27,28). On the other hand, the combination of T1, T2, and magnetization transfer contrast does increase the myelin specificity in a cuprizone mouse model which has selective and reversible demyelination with little or no axonal damage. The combination of these contrasts can separate normal, demyelinated, and remyelinated white matter 95% of the time, better than individual measurements (67).

When comparing to MTR, QMT parameters increase the specificity to myelin by

characterizing the underlying biological process of MT. However, the specificity of QMT parameters to demyelination still needs further investigation. The roles of axonal degeneration, inflammation, and edema in the pool size ratio measurements were not addressed in this study. Those pathologies may affect the QMT demyelination measurements, as indicated by some multiple contrast quantitative MRI methods. For example, the pool size ratio in QMT has been correlated to the myelin water fraction in multiple component T_2 measurement (68,69) to investigate its specificity to myelin. It was found that both parameters reflect the same thing (most likely myelin) to a great extent, but inflammation (69) may be difficult to distinguish from demyelination by pool size ratio measurements alone.

In this paper, we correlated the pool size ratio in QMT with the radial diffusivity in DTI to demonstrate the sensitivity of the pool size ratio to myelin by choosing two kinds of animals (shiverer and control mice) which are only differentiated by myelin content, without the involvement of other white matter disease pathologies, such as axonal degeneration, inflammation, and edema. Our results indicate a similar sensitivity for the radial diffusivity and the pool size ratio to changes in myelin between control and shiverer mice. While these measurements are both sensitive to myelin content, the mechanism of this sensitivity varies and may therefore reflect differently on subtle changes in pathology. The pool size ratio is determined by the lipids in myelin which are a conduit for spin exchange between the free water and macromolecules; the radial diffusivity is directly affected by the myelin sheath inhibition of water diffusion. Not

addressed in this study, the short T_2 spectrum from multiple exponential T_2 (MET2) method, is also likely caused by myelin lipids increasing the associated water relaxation rate. The relative merits, sensitivities, and specificities of these three measures are interesting topics for further quantitative MRI studies on myelin.

Conclusion

We applied a QMT imaging technique on ex vivo shiverer mouse brain, and compared these results with DTI and histology. Our results show that the pool size ratio and the radial diffusivity are potential non-invasive biomarkers for myelin detection. This is the first time that a QMT technique has been applied on the control/shiver mouse model, and it is also the first time that the pool size ratio has been correlated with the radial diffusivity to investigate the properties of myelin.

CHAPTER V

APPLICATIONS OF QMT IMAGING: SPECIFICITY TO MYELIN AS REVEALED BY IMAGING MICE OPTIC NERVES

In the previous chapter, the sensitivity of QMT measurements is tested by control/shiverer mice. The results correlate very well with histological studies and DTI studies. The significant difference in the pool size ratio map between dysmyelinated shiverer mouse brain and normal control mouse brain confirms that QMT is capable for myelin detection.

However, though demyelination is the major target of QMT study, central nervous system diseases are usually a combination of demyelination and other pathologies, such as edema, gliosis, inflammation, and axon degeneration. It is important to know the specificity of QMT to each of these pathologies.

In this chapter, another project of QMT applications is discussed. Optic nerves from mice that have undergone retinal ischemia were examined using SIR-FSE QMT technique. Previously published results indicate that the optic nerve from retinal ischemia mice suffers significant axon degeneration without detectable myelin injury at three days after reperfusion. At this time point, we acquired ex vivo QMT parameters in fixed brain tissue samples from both shiverer mice and control mice that have undergone retinal ischemia, and these QMT measures were also compared with diffusion tensor imaging (DTI) results. Our findings suggest that the QMT estimated ratio of the pool sizes of the

bound and free water protons reflects the different myelin contents in the optic nerves between the shiverer and control mice. This pool size ratio is specific to myelin content only and is not affected by the presence of axon injury in mouse optic nerve three days after transient retinal ischemia. This study in this particular animal model reveals the great specificity of QMT to myelin.

5.1 Introduction

Determining the specificity of the sensitivity of MT parameters to the underlying biophysical conditions is complicated by the typical coupling of pathological features. For example, though demyelination is the dominating pathology which affects the QMT parameters, the role of other pathologies such as inflammation on QMT measurements needs to be considered. Stanisz et al (69) examined the QMT properties on inflamed exercised neural tissues, and found that the pool size ratio is not the best indicator of demyelination when inflammation is also present, not only due to the increasing of the extra-myelin water protons by inflammation, but also due to the change of MT properties caused by the PH change in the inflamed sample. Odrobina et al (63) measured the QMT parameters for ex vivo demyelinated rats sciatic nerve, confirmed the correlation between myelin fraction and the pool size ratio, but also addressed the difficulty of separating demyelination with inflammation by QMT alone. Tozer et al (68) also correlated the pool size ratio in the QMT measurements with the myelin water fraction in the multiple component T2 measurements for human subjects. They suggested that it is still valuable

to perform both measurements to increase the specificity of those parameters on demyelination when there is existing inflammation.

Changes in axon integrity may also influence QMT measurements of demyelination. However, most current studies are limited to the relation of axonal damage to MTR, not to QMT parameters. For example, Schmierer et al measured the MTR in postmortem multiple sclerosis brain with the addition of quantitative pathological studies(29). They found significant correlation not only between myelin content and MTR, but also between myelin content and axonal count. However, it was not clear how axon count changes and myelin content changes separately affect the semi-quantitative MTR measurement, nor is it addressed how the axon count changes affect the quantitative MT measurements. Post mortem studies of the spinal cord of multiple sclerosis patients by Mottershead et al also revealed strong correlations of reduced myelin content and axonal loss to reduced MTR(70), but again without separating the effects of demyelination and both demyelination and axonal loss. Contradictorily, Blerzer et al investigated the quantitative MRI and pathology correlations of brain white matter lesions in experimental autoimmune encephalomyelitis (EAE) non-human primates, and their results showed that the correlation of axonal density with MTR was insignificant (71). Hickman et al (72) performed MT imaging in acute optic neuritis patients and found that MTR values were not changed at the onset when visual impairment was at its worst, proposed that it was possibly due to the acute axonal degeneration transiently increasing MTR and other pathologies decreasing MTR. Their suggested possibility of conflicting pathologies

shows the need for animal studies with separated and controlled pathologies. In summary, both appropriately specific animal models and more specific MR measures (i.e. the QMT measured pool size ratio) may be necessary to evaluate the correlations between demyelination measurements and changes of axonal pathology.

Mice optic nerves with transient retinal ischemia (which has both axonal damage and myelin degeneration during the time course) were examined by DTI(54,58). It was found that at three days after the retinal ischemia, the axial diffusivity of the injured optic nerve was significantly decreased, while the radial diffusivity of the injured optic nerve remained unchanged, and the correlated histology results indicated axonal damage but no demyelination. Therefore, mice optic nerves undergoing transient retinal ischemia is an excellent animal model to investigate the specificity of MRI techniques on the detection of demyelination while axonal damage is present. In the project discussed in this chapter, we utilized ex vivo mice optic nerve at three days after transient retinal ischemia (54,58), to test the dependency of the pool size ratio measured by QMT on the existing axonal degeneration. We acquired data on both shiverer and control mice, and both normal and injured optic nerves to investigate both the sensitivity and specificity of the pool size ratio on demyelination as separated from axonal degeneration. DTI and histology studies were also performed to provide a separate measure of the pathology.

5.2 Theory and Experimental Methods

QMT and DTI Methods

We chose the SIR-FSE method (36) to perform the QMT measurements. As discussed before, this technique uses a fast spin echo pulse sequence with a preceding 180 degree inversion pulse. Unlike the widely used pulsed saturation method (41), which manipulates the restricted macromoelucar spins, SIR-FSE selectively inverts the free liquid spins. As a result of MT, the free recovery of the liquid spins after the inversion pulse is bi-exponential (with fast and slow recovery rates on the order of magnitude of 25 Hz and 1 Hz, respectively) instead of single exponential (73). A series of inversion times are used to model the transient signal of the bi-exponential recovery after the inversion pulse. A constant pre-delay time t_d (the time delay after the fast spin echo acquisition in each repetition), instead of a constant repetition time *TR*, allows a determination of the QMT parameters when starting from non-equilibrium conditions and resulting in greater SNR efficiency (36). By fitting the measured transit signal of magnetization recovery for different inversion times to Eq. [2.4], the slow and fast recovery rates can be obtained, and the pool size ratio can be calculated from Eq. [2.8].

The derivation of DTI parameters are discussed in Appendix A. With the same approach of that in Chapter 4, Diffusion tensor (**D**) is derived according to Eq. [A.2], where S is the diffusion-weighted signal, S_0 is signal with diffusion weighting factor $b = 0$, and **n** is the encoding directions (62). The resulting tensor element maps are used to derive eigenvalues ($\lambda_1, \lambda_2, \lambda_3$) of the diffusion tensor by matrix diagonalization. The quantitative

indices including axial diffusivity ($\lambda_{\parallel}$), radial diffusivity ($\lambda_{\perp}$), and relative anisotropy (RA), are derived from equations [A.3]-[A.5].

Animal preparation

Unilateral retinal ischemia was induced in five shiverer and six control mice by raising the intraocular pressure (IOP) of the left eye above the systemic arterial pressure for 1 hour followed by reperfusion. At three days after the retina ischemia, all mice were euthanized and perfused with phosphate-buffered saline (PBS) followed by 10% formalin/PBS solution. The mice were decapitated and their heads were kept in 10% formalin/PBS solution and stored at 4^{o}C for one week. Before imaging, each mouse head was transferred to a 10mm diameter cylinder filled with PBS solution. As discussed in the previous chapter, this fixation increases SNR and eliminates motion issues while likely not affecting our ability to determine the sensitivity of QMT and DTI to myelination.

Data Acquisition

Cylinders with fixed mouse head were placed in a 1cm inner diameter solenoid coil which serves as both RF transmitter and receiver, and data from one coronal slice which contains both optic nerves were acquired in a 4.7T Varian UNITY INOVA spectrometer with an actively shielded Magnex gradient coil (10cm inner diameter, 60G/cm, 100 μs rise time). A fast spin echo sequence with a 1ms sinc inversion pulse was used for the

QMT experiments. 18 images with the inversion times ranging from 5ms to 7.9s were obtained with 2s constant pre-delay, 8 averages, 16 echoes, 10ms echo spacing time, 25mm by 25mm field of view, 0.8mm thick slice, and 256x256 data matrix zero-filled to 512x512. The total imaging time was 2 hours. Data were fitted to the bi-exponential function of the inversion times (equation [2.4]) to determine QMT parameters pixel by pixel.

A diffusion weighted spin echo pulse sequence with 1s repetition time, 4 averages, 38ms echo time, 13ms time between gradient pulses, 4ms diffusion gradient duration, b value of 1.879 $ms/\mu m^2$, diffusion sensitizing gradients along six directions (1,1,0)(0,1,1)(1,0,1)(-1,1,0)(0,-1,1)(1,0,-1), plus a normalizing image with no diffusion gradients, and the same spatial resolution as in the QMT experiments was used to acquire data (the scan time was 2 hours). On a pixel-by-pixel basis, the axial diffusivity ($\lambda_{\square}$), radial diffusivity ($\lambda_{\perp}$), and relative anisotropy (RA) were derived using software written in Matlab (MathWorks, Natick, MA, USA).

Statistical Analysis

For each QMT and DTI parameter, statistically significant difference between the injured and uninjured optic nerves was evaluated by a two-tailed student t-test. The t value was calculated by the means and standard deviations of each parameter in control/shiverer mice optic nerves. With the t-value and the known degree of freedom (6 control mice and 5 shiver mice gave a degree of freedom equals 9, the probability (p-value) that each

parameter being the same between the control and the injured optic nerves was determined.

Histology Study

After MRI studies, 4 mm thick coronal tissue blocks were obtained from each control and shiverer mouse brain and embedded in paraffin. 3 μs thick slices matching the MRI imaging slices were cut and deparaffinized in xylene for immunohistochemical examinations. The integrity of myelin was assessed by using a primary antibody against myelin basics protein (MBP, 1:250; Zymed Laboratories Inc., South San Francisco, CA). The integrity of axon was assessed by using a primary antibody against phosphorylated neurofilament (pNF, SMI-31, 1:1000; Sternberger Monoclonals, Lutherville, MD) with reactivity revealed by the avidin-biotion-peroxidase method (Zymed Laboratories). Following 15 minutes wash in PBS, slices were incubated in fluorescent secondary antibodies for one hour at room temperature (1:200, anti-rabbit conjugated to Texas Red for MBP, 1:200, anti-mouse conjugated to Alexa 488 for SMI-31; Molecular Probes). Histological sections were examined with a Nikon Eclipse 80i microscope equipped with a 60x oil objective, and digital images were captured with a Photometrics CCD digital camera using MetaMorph image acquisition software (Universal Imaging Corporation, Downington, PA). The MBP and SMI-31 positive axons were counted in a blinded fashion. Images captured from the center of each optic nerve were displayed using MetaMorph. Both the red MBP positive staining ring representing the myelinated axon

and the green SMI-31 positive staining dot representing the normal axon were counted. The axon counting was conducted through the entire captured image ($150\,\mu m \times 110\,\mu m$). The histology study was performed by the collaborating research group led by Dr. Sheng-Kwei Song in Washington University in St. Louis.

5.3 QMT, DTI, and Histological Results

Figure 5.1 shows the calculated relative anisotropy map from DTI experiments. The resulting QMT and DTI parameters are listed in table 5.1.

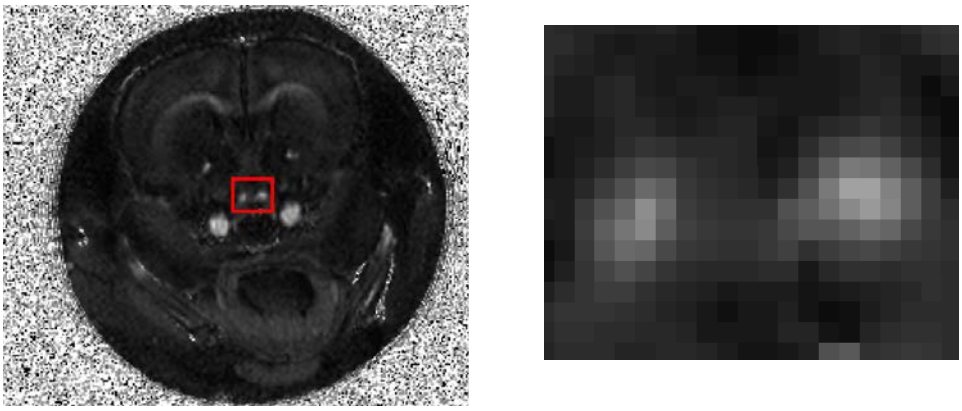

Figure 5.1: Left: the relative anisotropy (RA) map of one coronal slice of a control mouse. Optic nerves are located inside the red rectangle. Right: magnified RA map inside the red rectangle. RA maps have the best contrast between the optic nerve and surrounding tissues, therefore they were used to determine the position of the optic nerves and choosing ROIs for each mouse.

Table 5.1: Calculated QMT and DTI parameters for respective ROIs. We chose the whole optic nerve (excluding boundary pixels), which contains 12-20 pixels, as the ROI for each injured and uninjured optic nerve. The positioning of those ROIs were based on the relative anisotropy maps which have the most contrast between optic nerve and surrounding tissues, as shown in figure 5.1. The p value represents the statistically significant difference calculated by t-test.

			left (injured)	Right (uninjured)	p value
QMT	pool size ratio	control	0.102±0.011	0.099±0.014	0.70
		shiverer	0.069±0.004	0.076±0.007	0.07
	fast rate (s^{-1})	control	24±8	24±9	0.94
		shiverer	25±3	27±10	0.82
	slow rate (s^{-1})	control	0.92±0.09	0.92±0.08	0.90
		shiverer	0.89±0.04	0.87±0.05	0.50
DTI	radial diffusivity ($\mu m^2/ms$)	control	0.17±0.03	0.17±0.03	0.90
		shiverer	0.22±0.02	0.22±0.04	0.84
	axial diffusivity ($\mu m^2/ms$)	control	0.49±0.09	0.67±0.07	0.006
		shiverer	0.53±0.05	0.73±0.06	0.0002
	relative anisotropy	control	0.53±0.06	0.67±0.04	0.0011
		shiverer	0.49±0.04	0.63±0.05	0.0005

QMT and DTI results

The pool size ratios in the control mice optic nerves are much higher than those in the shiverer mice optic nerves (30% difference for the injured optic nerves, p=0.0001; 24% difference for the uninjured optic nerves, p=0.008). There is nearly no pool size ratio difference (3%, p=0.70) between the left (injured) and right (uninjured) optic nerves in the control mice, while there is insignificant difference (10%, p=0.07) in the shiverer

mice. The slow rates (the reciprocal of T1) and fast rates in all mice are similar between the injured and uninjured optic nerves.

The radial diffusivities are the same between the injured and uninjured optic nerves (no difference, p=0.90 for the control mice; no difference, p=0.84 for the shiverer mice). Meanwhile, the radial diffusivities in the shiverer mice are much higher than those in the control mice (23% difference for the injured optic nerves, p=0.03; 23% difference for the uninjured optic nerves, p=0.06). For the axial diffusivities, there are significant differences (33% for the control mice, p=0.006; 26% for the shiverer mice, p=0.0002) between the injured optic nerves and the uninjured optic nerves. Meanwhile, the axial diffusivities in the shiverer mice optic nerves are slightly and insignificantly higher than those in the control mice optic nerves (9% difference for the injured nerves, p=0.35; 8% difference for the uninjured nerves, p=0.17). For the relative anisotropy, there are significant differences (27% for the control mice, p=0.0011; 27% for the shiverer mice, p=0.0005) between the injured and uninjured optic nerves, while there are small differences (8% for the injured nerves, p=0.16; 6% for the uninjured nerves, p=0.17) between the control and shiverer mice.

Histological results

The myelin basic protein (MBP) and phosphorylated neurofilament (pNF, SMI-31) results are shown in figure 5.2. The counts of axons for normal and injured optic nerves in the control and shiverer mice are plotted in figure 5.3.

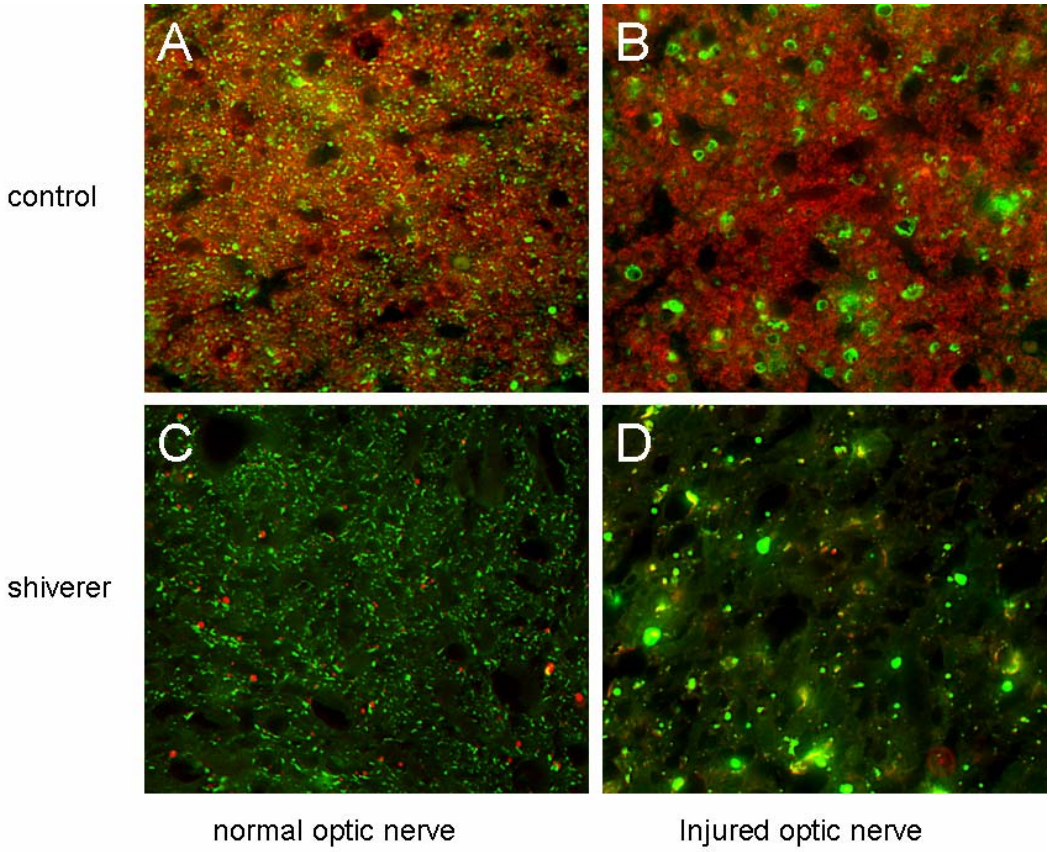

Figure 5.2: Immunohistochemical results for A) uninjured optic nerve of a control mouse B) injured optic nerve of a control mouse C) uninjured optic nerve of a shiverer mouse and D) injured optic nerve of a shiverer mouse. A and B show the axonal degeneration (the green color SMI-31 labeling) and no demyelination (the red color MBP labeling) at three days after the transient retinal ischemia in a control mouse optic nerve; C and D show the axonal degeneration at three days after the transient retinal ischemia in a shiverer mouse optic nerve; both A comparing to C and B comparing to D show the dysmyelination in the shiverer mouse optic nerve.

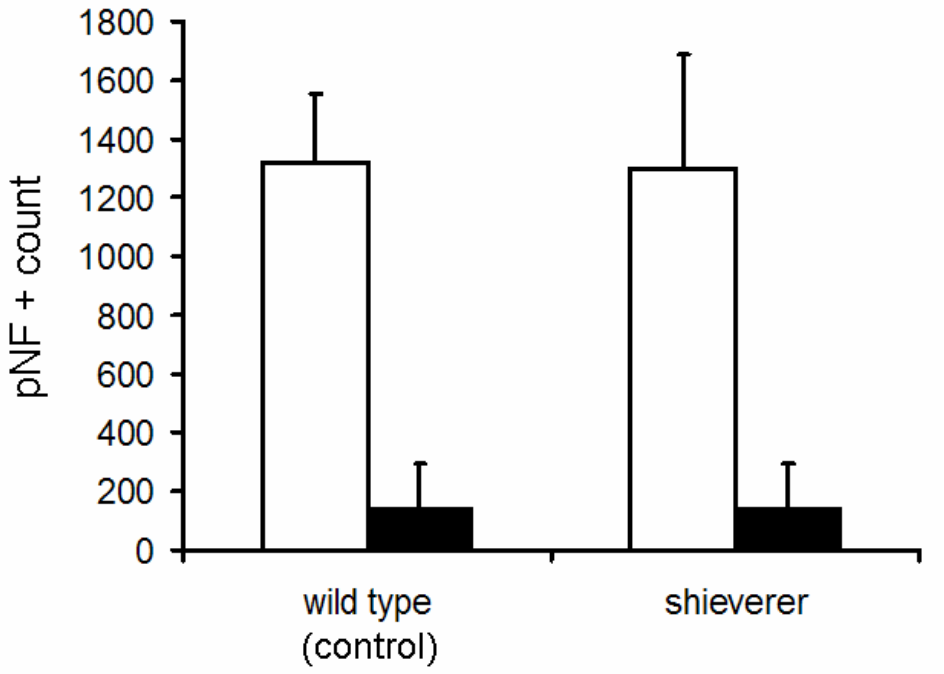

Figure 5.3: Quantitative analysis of immunohistochemistry in normal (white bars) and injured (black bars) optic nerves (N = 4 for each bar). The counts of axons (pNF stained) showed that the axonal density is comparable between shieverer and control mice optic nerves. Both mice showed significant loss of normal axons in injured optic nerves at 3 days after the transit retinal ischemia.

5.4 Discussions

It has been shown that white matter abnormalities may cause increased T_1 and T_2, decreased MTR, and changes of diffusion properties including RA, FA, and ADC (52,53,74). Those parameters are sensitive to both of the myelin and axon pathologies, and they are not able to differentiate the effects of demyelination and axonal degeneration. Though both pathologies usually accompany each other, they might develop at different stage and have different consequences. For example, it has been suggested that demyelination is the dominating pathology for the relapsing-remitting multiple sclerosis,

while axonal degeneration is the dominating factor for the irreversible chronic-progressive multiple sclerosis (75). Therefore, to seek MRI techniques to distinguish demyelination with axonal degeneration is essential for diagnosis and clinic applications.

Radial diffusivity and axonal diffusivity are suggested to reflect the integrity of myelin sheath and axon tracts, respectively (54-58,64). Meanwhile, the pool size ratio in QMT measurements is suggested to be highly related to myelin contents (76), and it is also a possible marker to differentiate the pathological changes in myelin sheath/axon tracts. QMT and DTI studies have been performed on control/shiverer mice corpus callosum. Both the pool size ratio and the radial diffusivity are sensitive to the myelin sheath of axonal fibers, and these two parameters correlate to each other very well (76). In this study, our findings on mice optic nerves support theses previous results. The pool size ratios in the control mice optic nerves (both the injured and uninjured nerves) are significantly higher than those in the shiverer mice optic nerves, correlating with the lack of myelin in the shiverer mice optic nerves. On the other hand, the radial diffusivities in the control mice optic nerves (both the injured and uninjured nerves) are significantly lower than those in the shiverer mice optic nerves, also indicating the lack of myelin in the shiverer mice optic nerves. Furthermore, the changes of pool size ratio and radial diffusivity are of a similar percentage, which is also consistent with our previous results on mice corpus callosum. Our results confirm that both the pool size ratio and radial diffusivity correlate with the integrity of myelin in mice optic nerves.

For QMT parameters other than the pool size ratio, the slow rates in the optic nerves are lower than the slow rates in the corpus callosum we measured previously (76). However, the slow rates in the control mice optic nerves are slightly higher than those in the shiverer mice optic nerves, consistent with previous corpus callosum results. The slow rate difference between the control and shiverer mice optic nerves is small, indicating that T1 is not an optimal marker for myelin. Nor is the fast recovery rate, since it is not differentiated between the control and shiverer mice optic nerves. For DTI parameters, we did not see any obvious change of axial diffusivities in the corpus callosum between the control and shiverer mice previously, but we did see small changes (8-9%) of axial diffusivities in the optic nerves between the control and shiverer mice. This may be due to the partial volume effects and the limited size of the ROI. In any case, the p values for the axial diffusivity in the optic nerves range from 0.17 to 0.35, indicating no significant difference. These values are also comparable to the p value ($p=0.27$) previously calculated from the corpus callosum axial diffusivities between the control and shiverer mice (76). The relative anisotropies in control mice optic nerves are higher than those in shiverer mice optic nerves, which is consistent with previous mice brain results, though more significant difference was observed in mice corpus callosum. In general, the QMT and DTI analysis on the dysmyelinated shiverer and the myelinated control mice optic nerves agrees well with our previous analysis on the shiverer/control mice corpus callosums.

Optic nerve contains dense packed myelin sheath around the axonal fibers and has no

crossing fiber tracts. After the transient retinal ischemia surgery, the degenerations of myelin and axon fiber start at different time points and proceed at different rates. In general, at three days after the transient ischemia, axonal degeneration is significant, but demyelination is absent (54,58). The separation of these two pathologies provides an excellent model to evaluate the specificity of QMT and DTI parameters to myelin. From our DTI results, the radial diffusivity, which previous results (55,56,58,76) indicate may reflect the myelin sheath integrity, is the same in the injured optic nerves and the uninjured optic nerves, and for both control and shiverer mice. These similar radial diffusivities indicate the lack of demyelination, which is confirmed by the MBP immunostaining results. On the other hand, the axial diffusivity, which may reflect the axonal fiber integrity (54,57,58), is significantly different between the injured and uninjured optic nerves, indicating that noticeable axonal degeneration is present in the injured optic nerves, which is in agreement with the neurofilament (pNF) labeling results. There is also significant difference for the relative anisotropy between the injured and uninjured optic nerves, mostly due to the difference of the axial diffusivity since the radial diffusivity is unchanged.

With the confirmation of Histology and DTI results that there is axonal degeneration but no demyelination, QMT measurements were performed on this animal model to check if there is any effect on the QMT parameters determination caused by the presence of axonal degeneration. We did not see any significant difference of the measured pool size ratios between the injured and the uninjured optic nerves for the control mice, which

suggests that axonal degeneration did not play a role in the detection of demyelination in the control mice by QMT measurements. For the shiverer mice, the uninjured optic nerves have slightly higher pool size ratio than the injured optic nerves. Since shiverer mice have nearly no myelin in their optic nerves, the source of this difference is from the contribution to the pool size ratio by pathologies other than demyelination. While our results indicate that changes in the pool size ratio principally reflect myelin changes, some dependence on non-myelin bio-structures is likely. For example, the pool size ratio of gray matter is not zero, and it is also not zero for the dysmyelinated shiverer mice white matter (76). However, any pool size ratio dependence on changes in non-myelin bio-structures in this model is small (9% difference between the injured and uninjured optic nerves of the shiverer mice) and of relatively low significance ($p=0.07$). Furthermore, our results also show that the slow and fast rates remain the same for the injured optic nerves when comparing to the uninjured optic nerves. Therefore, in general, the QMT measurements on demyelination are not affected by the presence of axonal degeneration.

Yarnykh et al produced QMT maps of healthy subjects in vivo (45). They were able to show the appearance of the major fiber tracts on the pool size ratio map, and therefore to show that pool size ratio is associated with the density of fiber tracts. Their results are not contradictory to ours, as the myelin sheath density also increases with increases in the fiber tract density. We were not able to see fiber tracts in the white matter of our pool size ratio maps due to the small size of mice brain and the relatively large voxel size for

microstructures imaging, but we were able to show that the pool size ratio measurement generally won't be affected by the axonal damage in the injured optic nerves. We believe that the density change of axonal fibers will affect QMT measurements because of the consequent myelin sheath density change, but the axonal degeneration caused by fiber transection won't affect QMT measurements.

Narayanan et al measured the pool size ratio in normal appearing white matter (NAWM) of MS patients via the pulse saturation technique (77). In addition to myelin detection by QMT, they also measured the resonance intensities of N-acetylaspartate (NAA) relative to creatine (Cr) to investigate the axonal injury. They found no correlation between the pool size ratio (putative myelin marker) and the NAA/Cr ratio (putative axonal intensity marker). Their results are consistent with axonal injury in the NAWM (i.e. the Wallerian degeneration of transected axons) not paralleling demyelination. The variation of the measured pool size ratio in the NAWM was small in their experiments, also implying that the existing axonal degeneration does not affect the pool size ratio measurement.

While our results are consistent with these human *in vivo* measurements, a full knowledge of the specificity of diffusion tensor and QMT imaging methods will require a range of animal studies where the relative degrees of demyelination, axonal loss, gliosis, and edema are varied. This study fills in a data point by comparing QMT and diffusion tensor results in an animal model separating the effects of demyelination and axonal degeneration. In general, the pathological specificity of a particular method in a particular animal model will depend on the concurrent biophysical changes, and modeling such

changes may provide insight into expected correlations. Diffusion tensor imaging is fundamentally about barriers, and will reflect pathologies only to the degree to which they affect water transport. While there have been a few studies modeling diffusion of myelin associated water (78-80), this water component, with its short T_2, likely plays only a small direct role in diffusion measurements of white matter, and instead myelin plays the role of a diffusion barrier. A third leading method for myelin specific imaging not included in this study is multi-exponential T_2 (MET2) and, like QMT, it is affected by the strong water-macromolecular coupling via the cholesterol in the lipid bilayers of myelin in white matter (23), and, therefore, these two methods may be expected to show similar sensitivity and specificity to various pathologies. Four pool modeling studies of white matter (81,82), however, have given conflicting results on whether there is an underlying biophysical basis for QMT-MET2 correlation.

5.5 Conclusions

We implemented selective inversion recovery fast spin echo (SIR-FSE) quantitative magnetization transfer (QMT) imaging technique to investigate the integrity of myelin in optic nerves after transient retinal ischemia in control and shiverer mice. We found that at three days after the ischemia there was significant axonal degeneration in mice optic nerves, but no detectable demyelination. Our QMT measurements sensitivity to myelin was not affected by the axonal injury, as indicated by the control versus shiverer QMT results. In addition, QMT parameters were similar between the injured optic nerves and

uninjured optic nerves. Our results suggest that the key QMT parameter, the pool size ratio, is not only sensitive but also specific to demyelination even when axonal injury is co-existing.

CHAPTER VI

APPLICATIONS OF QMT IMAGING: COMPARISONS OF QMT, DTI, AND MET2 IMAGING IN LPS INDUCED WHITE MATTER PATHOLOGY IN RATS

In Chapter 4 and Chapter 5, the sensitivity and specificity to myelin by QMT measurements are discussed. It was found that in shiverer mice brain and optic nerves the QMT measured pool size ratio may be an accurate non-invasive marker for myelin. However, the effects from pathologies other than demyelination need to be considered. Study on mice optic nerves undergoing transit retinal ischemia suggests that existing axonal degeneration does not affect the myelin measurements by QMT; on the other hand, published results suggest that QMT measurements need to be correlated with MET2 measurements to differentiate inflammation with demyelination (69). Considering that most central nervous system (CNS) diseases are a combination of pathologies including demyelination, inflammation, edema, gliosis, and axon degeneration, further investigation of the specificities of quantitative MRI methods is warranted. In this chapter, a new animal model, rats after lipopolysacharride (LPS) injection in the brain, is introduced. QMT, DTI, and MET2 methods are applied to this animal model to study the pathological changes of rat brain after LPS injection. The correlation of these three quantitative MRI methods with the underlying pathologies as revealed by histology is expected to provide valuable information for the understanding of this animal model and for the relative specificity of different myelin imaging methods.

6.1 Introduction

The most common target of myelin imaging is multiple sclerosis (MS). MS lesions are suggested to be heterogeneous and can be categorized to four types (83,84). Type Ⅰ and type Ⅱ lesions are inflammatory in nature and resemble that seen in autoimmune models of CNS demyelination, such as experimental allergic encephalitis (EAE) (85). Extensive studies have been performed to investigate EAE animal models, including many magnetic resonance imaging studies (27,86,87). However, EAE does not provide a model of oligodendracyte loss that can occur in the absence of cellular inflammation. The degeneration and apoptosis of oliogodendrocytes in the absence of inflammatory cellular infiltrate (primary oligodendrogliopathy) are suggested to be pathologies of type Ⅲ and type Ⅳ MS lesions (83), and may be responsible for the progressive phase of MS, which show no improvement with immunosuppressive therapy (88-90). Therefore, halting the progression of MS may require novel strategies for identifying primary oligodendrogliopathy and novel therapeutic approaches directed at slowing and reversing non-inflammatory demyelination. To achieve that, studies on appropriate animal models with generated non-inflammatory demyelination are essential.

Recently, lipopolysacharride (LPS) has been injected to different animal models to induce inflammatory injury and experimental demyelination (91-93). For example, a primary CNS demyelination animal model has been induced by injecting LPS into the spinal cord of rats (94). It was found that the intraspinal injection of LPS results in inflammation and subsequently in prominent demyelination. Based on those published results, it is

speculated that inflammatory and later non-inflammatory demyelination will also occur in the corpus callosum of rats after LPS injection in the brain.

In the current work presented in this chapter, both *in vivo* quantitative MRI methods and ex vivo immunohistological methods have been applied to LPS injected rats at different end points (7 days, 14 days, 28 days after the injection) to measure the pathological changes in the brain. Ideally, there are two goals for this study: first, to further develop a novel rat model that demonstrates phases of inflammatory and later non-inflammatory CNS demyelination by multiple MRI methods and immunohistological methods. The potential use of this animal model is drug evaluation of the remyelination of MS lesions. The second goal is to further investigate the specificity and correlation of these three quantitative MRI methods (QMT, DTI, and MET2) in imaging myelin by studies on this assumed multi-phase LPS rats demyelination model. Currently, there are no other research groups applying all three of these quantitative MRI methods on the same animal model. Unique information might be obtained by side-by-side comparisons of these three techniques.

6.2 Materials and Methods

Animal Preparation

Nine rats (6 weeks old, weights about 200 g) were used for this study. Three of them were injected with saline in one side of the brain, and the remaining six were injected with LPS in one side of the brain. Each rat was anesthetized by 2% isoflurane and positioned in a

small animal stereotaxic frame to confirm with a brain atlas. The hair on top of the brain region was shaved, and the skin was cleaned by alcohol and iodine solution before incised to expose the skull. The injection site was measured by 1 mm posterior and 1 mm lateral to the bregma (the junction point of the sagittal and coronal sutures of the skull). A high speed drill was used to penetrate the skull by drilling a hole with 1 mm diameter. Microinjection was performed with a 32-gauge needle inserting through the hole on the skull. Saline/LPS was injected at 3 mm to 3.2 mm beneath the dura mater with a rate of 0.5 μl /min by a 5 μl Hamilton Syringe operated by the microinjection pump. The needle stayed inside the brain for 10 minutes before pulled out. In total 5 μg /5 μl LPS or saline solution was injected into each rat. After injection, the needle was pulled out gently and the skin incision was carefully sutured. Bitter apple and topical lidocaine were applied to the wound and the animal was allowed to gradually recover from anesthesia before returned to cage.

Other than those nine rats, there were 11 other control and LPS rats with different injection procedures. Specifically, the injection was made less than 1 minute and the needle was pulled out from the rat brain immediately after the injection, which might have caused incomplete injection because the needle might suck out the injected LPS/saline solution before it diffuses. Results from these rats will also be presented in this chapter for reference but will be analyzed separately.

MRI Experiments

All MRI experiments were performed on a Varian Inova 7 Tesla scanner with a 16 cm bore, actively shielded gradients of 27 G/cm, rise time to full amplitude of 100 μs. At three different end points (7 days, 14 days, and 28 days after the injection), at least one control rat (injected with saline) and two LPS rats (injected with LPS) were scanned. A 38 mm coil quadrature volume coil was used as both transmit and receive coil. Each rat was anesthetized by 2% isoflurane and its temperature was kept at 37° by supplying hot air flow. The respiration of the rat was also monitored and controlled at about 50 breathes per minute by slight adjusting of the isoflurane level.

The theory of selective inversion recovery fast spin echo (SIR-FSE) QMT has been discussed in previous chapters; the theory of DTI and MET2 measurements is addressed in Appendix A and Appendix B, respectively. In our experiments, T_2 weighted fast spin echo images were used to determine sample geometry and to select a roughly axial imaging slice (perpendicular to the corpus callosum) containing the needle track of the injection and symmetric with respect to the brain geometry. For this imaging slice, a fast spin echo sequence with a 1 ms hard inversion pulse was used for the QMT experiments. 22 images with the inversion times ranging from 4 ms to 6 s were obtained with 2.5 s constant pre-delay, 2 averages, 8 echoes, 10 ms echo spacing time, 35 mm by 35 mm field of view, 1 mm thick slice, and 128x128 data matrix zero-filled to 256x256. The total imaging time was about half an hour. Data were fitted to the bi-exponential function of the inversion times (equation [2.4]) to determine QMT parameters pixel by pixel.

A diffusion weighted spin echo pulse sequence with 1.2 s repetition time, 2 averages, 29 ms echo time, 15 ms time between gradient pulses, 6 ms diffusion gradient duration, b value of 1.3398 $ms/\mu m^2$, diffusion sensitizing gradients along twelve directions (1,1,0), (-1,-1,0), (0,1,1), (0,-1,-1), (1,0,1), (-1,0,-1), (-1,1,0), (1,-1,0), (0,-1,1), (0,1,-1), (1,0,-1), (-1,0,1) plus a normalizing image with no diffusion gradients, and the same spatial resolution as in the QMT experiments was used to acquire data (the scan time was about 50 minutes). Respiration gating was applied if there was obvious motion artifact. On a pixel-by-pixel basis, the axial diffusivity ($\lambda_{\parallel}$), radial diffusivity ($\lambda_{\perp}$), and relative anisotropy (RA), as defined by equations [A.3]-[A.5], were derived by Matlab.

A multiple spin echo pulse sequence was used to acquire data for MET2 measurements. The same resolution and imaging slice position was chosen, but the slice thickness was set to 2 mm to increase the SNR. 8 averages, 3 s repetition time, 32 echoes with echo times linearly distributed between 10 ms and 320 ms were used. The total scan time was about 50 minutes. The signal intensity of regions of interest (ROI) in the acquired 32 images were used to fit to a multiple exponential function to determine T_2 spectrums.

Histological Studies

Histological studies for the LPS rats were performed by the collaborating research group led by Dr. Subramaniam Sriram in the Neurology Department of Vanderbilt University. After the rats were scanned in the MRI scanner, they were sacrificed immediately. Each rat was perfused by 100 ml 4% paraformaldehyde/sucrose. The rat head was decapitated

and the brain was taken out and stored in 10% formalin solution for three days for fixation. Then the brain was cut to 4 mm thick blocks and embedded in paraffin before sectioning. The sectioning was performed by the Neuropathology Lab of Vanderbilt University. 10 μm thick slices were obtained and mounted on plates for staining. Luxol fast blue (LFB) immunostainings were performed to detect the myelin content in the rat brain, primarily in the corpus callosum. LFB is widely used for staining of myelin/myelinated axons on formalin-fixed, paraffin-embedded brain and spinal cord tissue sections, as well as frozen sections. The myelin, including phospholipids, will be stained blue to green, and the neurons will be stained violet.

6.3 Results and Discussions

Due to the limited sample size and insufficient histological results at this time, indicative but not conclusive results have been obtained for this project. The results will be presented here in three categories, classified by the time duration between injection and imaging of the LPS and Control rats.

Rats at 7 days after injection

The needle track of the injection was visible for all rats. Two ROIs were chosen: one in the left side of corpus callosum, right beneath the injection, with a length of about 2 mm, which contains about 20-30 pixels; the other ROI is located at the corresponding position of the right side corpus callosum, with similar size (Example ROIs are shown in figure

6.2). The QMT and DTI parameters for each ROI were averaged from the generated parameter maps; the MET2 spectrum for the ROI was also computed and the myelin water fraction was calculated. The QMT and DTI parameter maps for the pool size ratio, radial diffusivity, axial diffusivity, and relative anisotropy for one LPS rat are shown in figure 6.1; the MET2 spectrum for this rat is shown in figure 6.2; the quantitative results for the parameters in the control and LPS rats are listed in table 6.1.

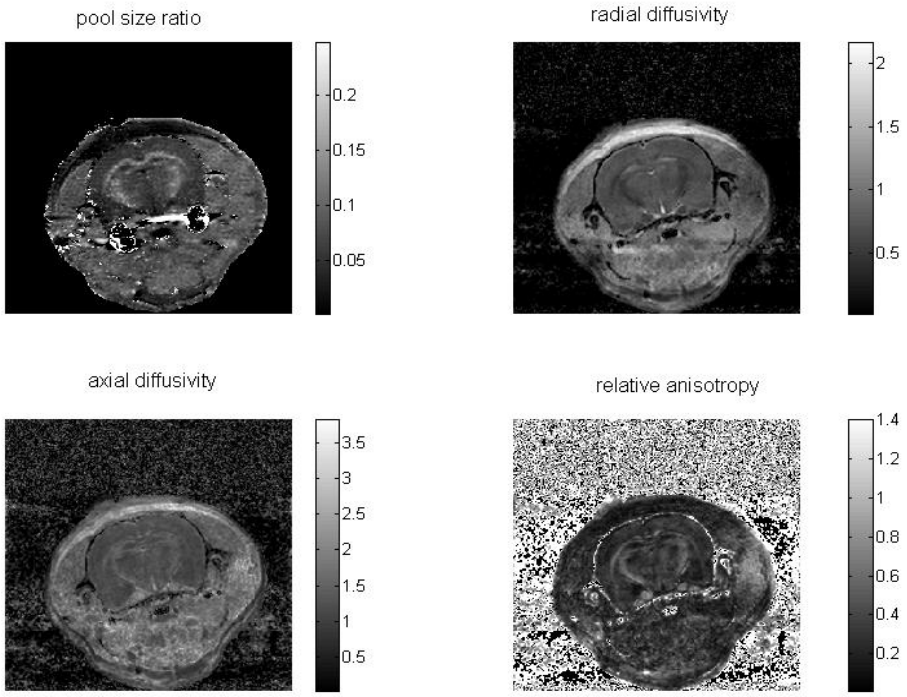

Figure 6.1: The calculated QMT and DTI parameter maps for one LPS rat.

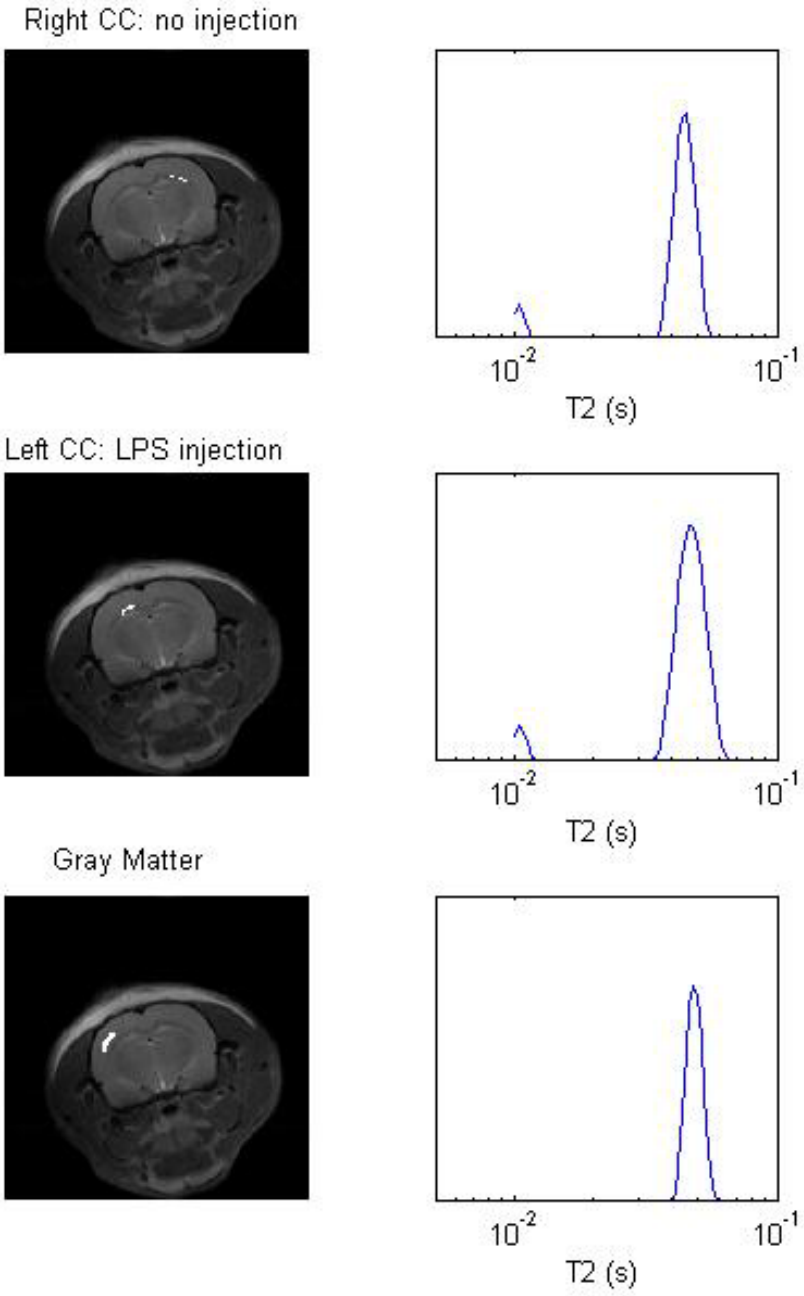

Figure 6.2: The multiple exponential T_2 spectrum (right column) for different ROIs (white regions in left column).

Table 6.1: The measured QMT, DTI, and MET2 parameters for ROIs in both sides of the corpus callosum for one control and two LPS rats at 7 days after injection. F: pool size ratio; RD: radial diffusivity; AD: axial diffusivity; RA: relative anisotropy; MWF: myelin water fraction.

	F	**RD($\mu m^2/ms$)**	**AD($\mu m^2/ms$)**	**RA**	**MWF**
LPS: Injection	0.1091±0.0164	0.5039±0.0346	1.3081±0.1015	0.5015±0.0612	0.0724
Contralateral	0.1274±0.0142	0.5809±0.0232	1.3295±0.1353	0.4563±0.0479	0.0971
LPS: Injection	0.1106±0.0184	0.6775±0.0485	1.3099±0.0913	0.4204±0.0771	0.0512
Contralateral	0.1341±0.0198	0.5980±0.0579	1.5611±0.1491	0.4958±0.0972	0.0588
Ctrl: Injection	0.0959±0.0225	0.5197±0.0557	1.0863±0.1144	0.4038±0.0805	0.0620
Contralateral	0.0882±0.0258	0.4667±0.0869	1.0971±0.0919	0.4865±0.1405	0.0734

The QMT results correspond to expected demyelination when comparing left to right for each rat. Both LPS rats have a smaller pool size ratio in the injection area than in the non-injection area. On the other hand, the injection of saline in one side of the corpus callosum in the control rat did not induce a significant pool size ratio difference. The DTI results for the two LPS rats are conflicting to some degree. The first LPS rat has slightly lower radial diffusivity and slightly higher relative anisotropy but with similar axial diffusivity when comparing left to right, the reason for this diffusivities change is unknown. The DTI results of the second LPS rat show typical demyelination and axonal degeneration, with higher radial diffusivity and lower axial diffusivity and relative

anisotropy in the left comparing to the right. The MET2 measured myelin water fraction is slightly lower in the injection side compared to the non-injection side in the corpus callosum of each rat. Though limited by sample size, these initial results indicate greater pathological changes from LPS than from saline injected rats, as expected. The pathological change in the first LPS rat might be a combination of demyelination and/or inflammation (and possibly slight edema, too), and the pathological change in the second rat might be a combination of demyelination and axonal degeneration (and possibly slight inflammation), though a clear determination of the underlying pathology is not possible without corresponding histological results.

Rats at 14 days after injection

QMT, DTI, and MET2 results are available for one control and two LPS rats at 14 days after the injection; in addition, QMT and DTI results are available for another one control and two LPS rats which were prepared by different injection methods (the injection time was 1 minute instead of 10 minutes). The quantitative MRI parameter maps for these six rats are very similar to the images in figure 6.1, and are therefore not shown. ROIs in left and right side of the corpus callosum in each rat were chosen in the same way as were those in 7 days rats. Parameter values at each ROI were listed in table 6.2 and table 6.3, respectively, for the first sets of rats (10 minutes injection time) and the second sets of rats (1 minute injection time).

Table 6.2: The measured QMT, DTI, and MET2 parameters for ROIs in both sides of the corpus callosum for one control and two LPS rats at 14 days after injection (needle stayed in the brain for 10 minutes during the injection). F: pool size ratio; RD: radial diffusivity; AD: axial diffusivity; RA: relative anisotropy; MWF: myelin water fraction.

	F	**RD($\mu m^2 / ms$)**	**AD($\mu m^2 / ms$)**	**RA**	**MWF**
LPS 1: injection	0.0998±0.0191	0.4934±0.0870	1.3813±0.2603	0.5359±0.0697	0.0276
contralateral	0.1001±0.0150	0.4552±0.0370	1.5971±0.0540	0.6490±0.0344	0.0248
LPS 2: injection	0.1011±0.0105	0.6371±0.0357	1.3119±0.0728	0.4008±0.0448	0.1154
contralateral	0.1341±0.0198	0.6887±0.0548	1.1570±0.0606	0.2732±0.0386	0.1075
Ctrl 1: injection	0.0797±0.0247	0.6622±0.1493	1.2811±0.1730	0.3817±0.1519	0
contralateral	0.1211±0.0390	0.5742±0.0467	1.0745±0.0663	0.3501±0.0571	0.0865

Table 6.3: The measured QMT and DTI parameters for ROIs in both sides of the corpus callosum for additional one control and two LPS rats at 14 days after injection (the time for injection was 1 minute). F: pool size ratio; RD: radial diffusivity; AD: axial diffusivity; RA: relative anisotropy.

	F	**RD($\mu m^2 / ms$)**	**AD($\mu m^2 / ms$)**	**RA**
LPS 3: injection	0.1219±0.0123	0.5139±0.0518	1.2297±0.1301	0.4664±0.0873
contralateral	0.1141±0.0145	0.4722±0.0702	1.1607±0.1786	0.4859±0.1343
LPS 4: injection	0.1373±0.0350	0.6118±0.1841	1.2777±0.2603	0.4145±0.0923
contralateral	0.1569±0.0231	0.4946±0.1387	1.5898±0.1638	0.6179±0.1586
Ctrl 2: injection	0.1455±0.0227	0.4674±0.1099	1.1864±0.1365	0.5141±0.1320
contralateral	0.1612±0.0228	0.5664±0.1206	1.5034±0.3104	0.5190±0.1831

The results for rat LPS1 and LPS4 (when comparing left to right) can be explained by demyelination and axonal degeneration caused by LPS injection; however, the QMT and DTI results for LPS2 and LPS3 were not as expected, especially the increase of axial diffusivity in both rats and the increase of relative anisotropy in LPS2 (when comparing left to right), which might be caused by edema. There were obvious parameter changes in the Ctrl1 rat in the injection side of the corpus callosum; however, this change was likely not caused by demyelination. This change can be well explained by severe edema in the injection area, since the pool size ratio is largely decreased, both the radial diffusivity and axial diffusivity are increased, and the myelin water fraction is nearly zero. This edema is

confirmed by abnormally high signal intensity in T_2 weighted images in this area, as shown in figure 6.3.

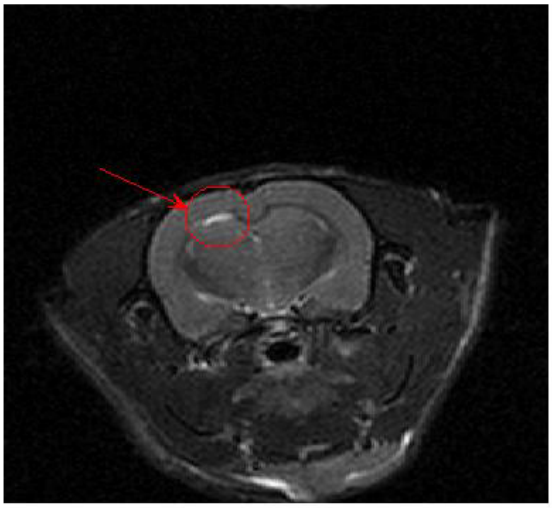

Figure 6.3: edema (inside the read circle) at the saline injection site in a control rat.

The inconclusive results in table 6.2 and table 6.3 might be due to both variations in animal preparation and insufficient sample size. The results for two control rats (exclude the edema ROI) were combined, as well as the results for four LPS rats, in spite of the different animal preparation methods used. Figure 6.4 shows the comparison of left side (injection) to right side (contralateral) parameters for control and LPS rats, and the direct comparison of control to LPS if averaging the parameters in both sides. The left to right comparison results for the contral rats are difficult to interpret, which is not surprising given it is the average of only two animals, one with clear indication of edema and the other with unclear pathology. The results for the LPS rats, however, are consistent with

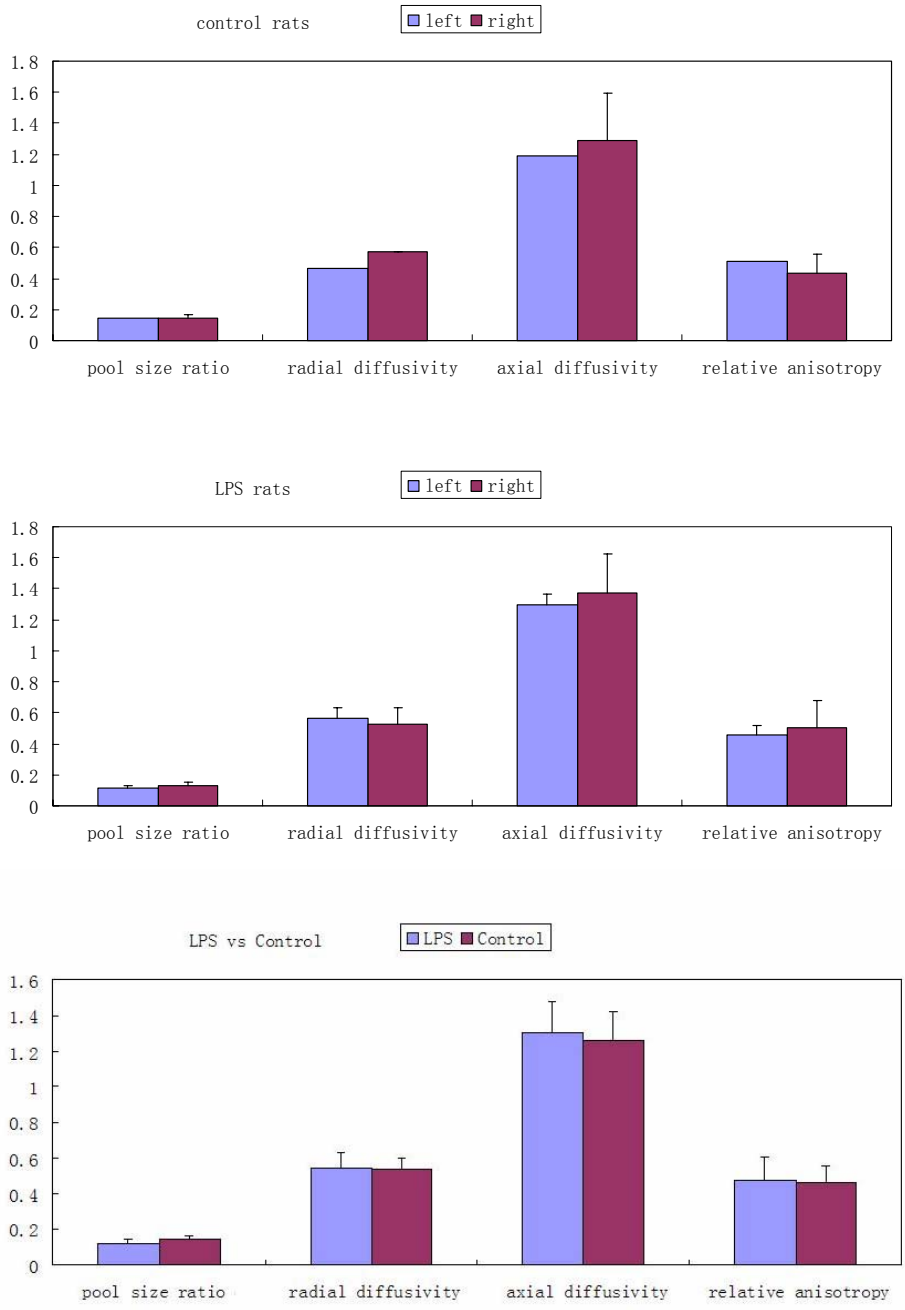

Figure 6.4: from top to bottom: parameters comparison between left corpus callosum and right corpus callosum for 14 days control rats; parameter comparison between left and right for 14 days LPS rats; parameter comparison between 14 days control and LPS rats. The y axes are unitless numbers for the pool size ratio and the relative anisotropy, and have units of $\mu m^2 / ms$ for the radial and axial diffusivity.

demyelination and possibly axonal damage, with decreased pool size ratio, increased radial diffusivity, decreased axial diffusivity, and decreased relative anisotropy. The final plot of LPS vs Control shows no significant changes at this number of samples. While all the measures will benefit from increased numbers of animals, the comparison of an LPS injection to the contralateral area gives the best preliminary indication of correlations.

Rats at 28 days after injection

4 control and 11 LPS rats were scanned at 28 days after injection. The injection time (the time that the needle stayed in the brain) was 10 minutes for 1 control and 3 LPS rats, and 1 minute for the remaining 3 control and 8 LPS rats. For statistic consideration, the data from these two different injection processes are combined, and their average values and standard derivations were calculated. The quantitative MRI results (QMT and DTI only. MET2 results are not available) for these rats are listed in table 6.4.

Figure 6.5 shows the comparison of parameter differences from different aspects. It was found that there is no obvious difference between left (injection) and right (contralateral) corpus callosum for the control rats. The comparison between the left and right for the LPS rats (the second plot in figure 6.5) gives unclear results, since the lower pool size ratio in the injection site (left side) indicating possible demyelination, but the slight lower radial diffusivity in the same ROI indicating possible remyelination. However, when we compare the control rats to the LPS rats (the third plot in figure 6.5), the QMT results agree with DTI results, as both the slightly decreased pool size ratio and the increased

radial diffusivity in the corpus callosum reveals demyelination.

Table 6.4: measured QMT and DTI parameters for the 4 control and 11 LPS rats at 28 days after injection. F: pool size ratio; RD: radial diffusivity; AD: axial diffusivity; RA: relative anisotropy.

	F	**RD($\mu m^2 / ms$)**	**AD($\mu m^2 / ms$)**	**RA**
LPS: injection	0.1145±0.0094	0.6064±0.0557	1.1587±0.1928	0.3617±0.0761
contralateral	0.1377±0.0139	0.6309±0.0748	1.2458±0.0571	0.3827±0.0653
Ctrl : injection	0.1255±0.0070	0.5030±0.0478	1.4194±0.2593	0.5725±0.1133
contralateral	0.1333±0.0255	0.5234±0.0538	1.3536±0.2217	0.5433±0.0828

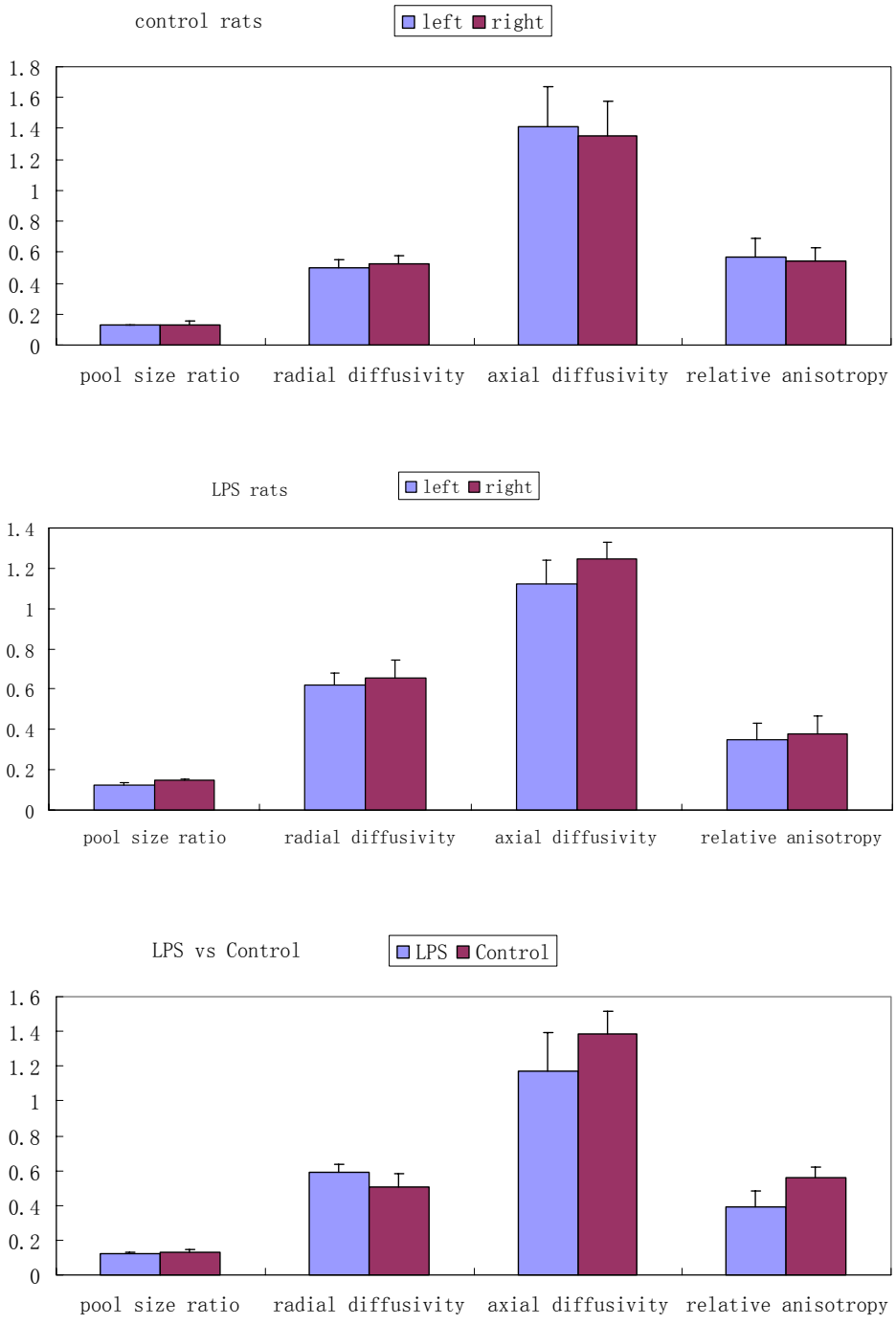

Figure 6.5: from top to bottom: parameters comparison between left corpus callosum and right corpus callosum for 28 days control rats; parameter comparison between left and right for 28 days LPS rats; parameter comparison between 28 days control and LPS rats.

Histological results

Figure 6.6 show the LFB staining results for a rat at 7 days after the LPS injection. There is clear myelin loss in the corpus callosum under the needle track in the left side of the brain. The demyelinated region is relatively small, with a length in the order of 1 μm. Also the 10x zoomed picture shows a number of inflammatory cells in this region. There is no myelin loss in the contralateral region (right side of the corpus callosum).

Figure 6.7 show the LFB staining results for a rat at 14 days after the LPS injection. The demyelination in the 14 days rat is severe than that in the 7 days rat, with a larger demyelination region (in the left side of corpus callosum) which has the tendency of extending to the contralateral side. Inflammatory cells in the demyelination region are obvious, more than that in the 7 days rat.

Figure 6.8 shows LFB staining results for a rat at 28 days after the LPS injection. The demyelination region clearly extends to the contralateral side, and inflammatory cells are less than that in 14 days rat.

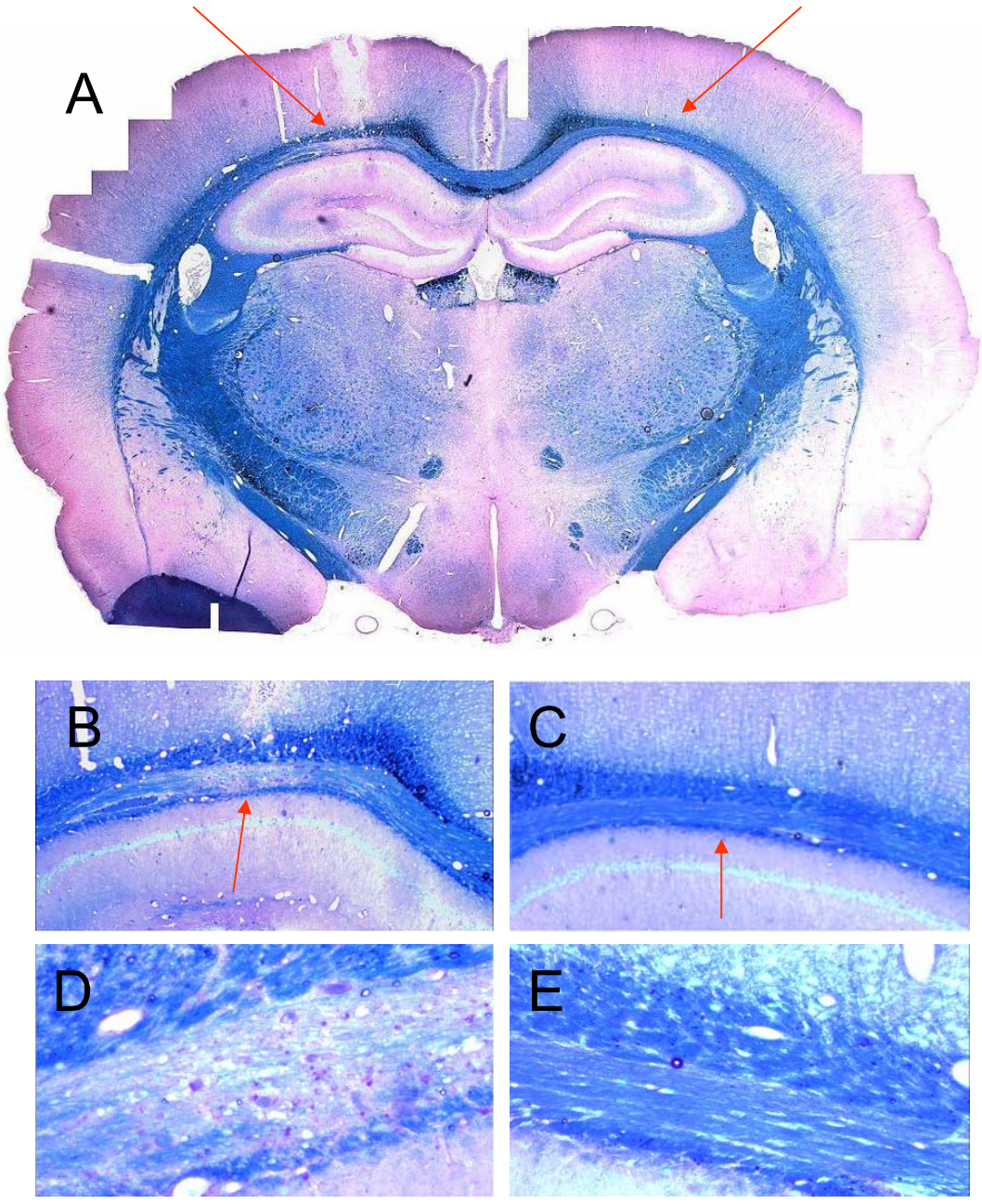

Figure 6.6: The LFB staining result (7 days after the injection) for a rat with LPS injection on the left side of brain. The red arrows point to the injection and contralateral regions. A is a picture for the whole brain; B and C are the 2x zoomed pictures for the injection and contralateral regions, respectively; D and E are the 10x zoomed pictures.

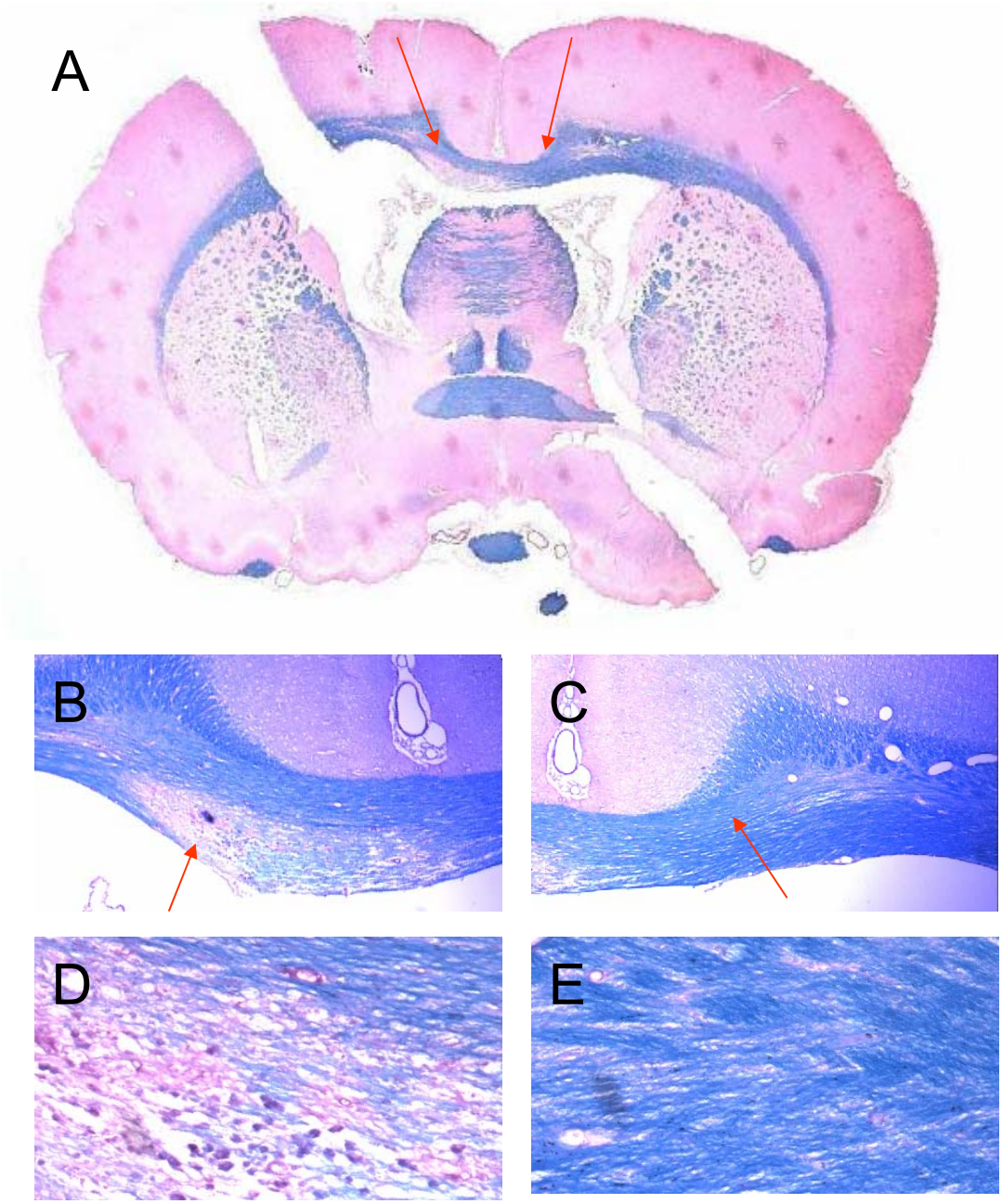

Figure 6.7: The LFB staining result (14 days after the injection) for a rat with LPS injection on the left side of brain. The red arrows point to the injection and contralateral regions. A is a picture for the whole brain; B and C are the 2x zoomed pictures for the injection and contralateral regions, respectively; D and E are the 10x zoomed pictures.

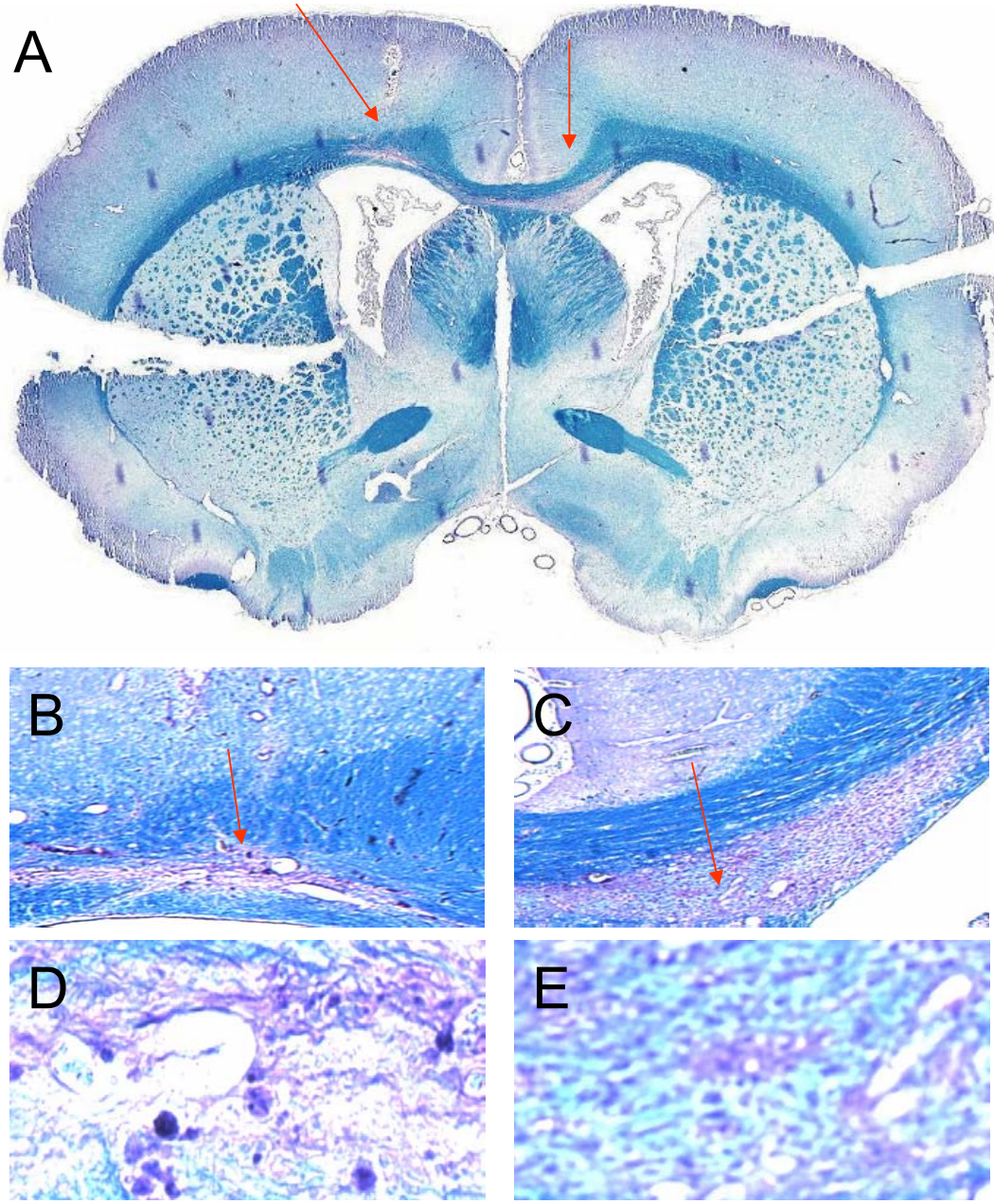

Figure 6.8: The LFB staining result (28 days after the injection) for a rat with LPS injection on the left side of brain. The red arrows point to the injection and contralateral regions. A is a picture for the whole brain; B and C are the 2x zoomed pictures for the injection and contralateral regions, respectively; D and E are the 10x zoomed pictures.

6.4 Conclusions

The injection of LPS to rat brain induces pathological changes in the corpus callosum. At 7 days after the LPS injection, there is slight demyelination with noticeable inflammatory cells in the injection side. At 14 days after the LPS injection, there is clear demyelination in the injection side, and the demyelinating region tends to extend to the contralateral side. Meanwhile, the number of inflammatory cells increased. The MRI results show QMT, DTI and MET2 parameter differences between left and right corpus callosum in the LPS rats, consistent with the LFB staining results which reveal myelin loss in the injection side but not the contralateral side. At 28 days after the LPS injection, the inflammation is much less, but the demyelination is more severe. The contralateral side in the corpus callosum has extensive myelin loss. The MRI results show QMT and DTI parameter differences between control and LPS rats, consistent with the LFB staining results which reveal myelin loss in both the injection and the contralateral sides of LPS rat.

In general MRI results agree with histology results in this study. However, only qualitative comparisons between these preliminary results are available. Future study includes quantitatively correlating MRI results to histology results. Specifically, quantitative histological study may provide additional information such as amount of demyelination, counts of inflammatory cells, etc; and rigid co-registration of MRI images to LFB images may enable optimized ROI choices for data analysis.

CHAPTER VII

CONCLUSIONS AND FUTURE DIRECTIONS

Since its discovery in late 1980's, magnetization transfer imaging has been widely used in research and clinical areas. Magnetization transfer ratio measurements are popular because the pulse sequence programming is easy to implement; the images are usually free of artifacts; the data analysis is simple; and most importantly, it gives a measure of myelin pathology unavailable in conventional MR imaging. However, the limitation of characterizing MT by only MTR is also clear. MTR is affected by both MT phenomenon and non-MT phenomenon, such as relaxation effects. Furthermore, MTR values also depend on pulse sequence details. In the mid 1990's, quantitative magnetization transfer (QMT) measurements were proposed. QMT completely characterizes the MT process by using six independent parameters, including two exchange terms and four relaxation terms, possibly increasing the specificity of pathology sensitivity. While an increasing number of groups have adopted QMT methods over the last decades, MTR imaging, with its simplicity, has remained the most utilized measure of MT.

The goal of any QMT technique is to determine QMT parameters. Unlike MTR, which is just a simple ratio of two signal intensities, QMT parameters are more difficult to compute. The general approach is to derive a signal equation (which contains all or a subset of those six QMT parameters) for a particular pulse sequence which is weighted

by MT effects, then fit the experimentally acquired data to this signal equation to determine the QMT parameters. Usually QMT techniques are categorized by either saturation technique (on-resonance/off-resonance) or acquisition method (transit/steady state). For example, the new spoiled gradient echo QMT technique introduced in this dissertation is an on-resonance steady state technique. There are several groups in the world developing different QMT techniques independently. Some of the most acknowledged techniques are already discussed in detail in Chapter 2. In general, each technique has its own strength and weakness. It is an interesting topic to compare different QMT techniques and to define an optimized one if possible. There are already some groups trying to compare different QMT methods. However, currently there are still very limited published literatures which provide extensive studies and careful comparisons of QMT techniques. Therefore, the further validation of each QMT technique and the eventual optimization of QMT measurements remain worthwhile topics.

The application of QMT has been suggested by many research groups and has been demonstrated in this dissertation by three examples. The sensitivity and specificity to myelin make QMT a promising method for the imaging of CNS diseases. However, the complexity of CNS pathologies may require more understanding of the connection between biological properties of tissue and physical properties measured by QMT imaging. Meanwhile, the correlation with other imaging methods such as DTI and MET2 might be useful to fully characterize CNS diseases. The LPS project is this dissertation is

intended to be a multiple dimension quantitative MRI study on an animal model with multiple phases of pathological changes. Though some intriguing preliminary results have been obtained in this study, more MRI measurements on a larger sample size, and most importantly, more immunohistological studies which can be used to interpret MRI results, are required to complete the two goals described in the introduction section of Chapter 6.

QMT has been already applied in studies *in vivo*. The QMT parameters in different regions in the brain of human subjects have been measured by a few groups (32,33,45,50). With the advancement of QMT techniques in terms of shortening scan time, and the availability of high field human MRI scanner which provides high SNR, it may be possible to use QMT parameters as non-invasive makers for the diagnosis of many human CNS diseases. Ideally, a combination of QMT, DTI, and MET2 parameters may be able to serve as quantitative MRI standards in a clinical setting to diagnose white matter/gray mater abnormalities and differentiate demyelination, inflammation, edema, and axonal degeneration in the brain of patients.

Appendix A: Diffusion Tensor Imaging

In this appendix, an important magnetic resonance imaging technique, diffusion tensor imaging (DTI), will be introduced. DTI enables the measurement of restricted water diffusion in tissue, and therefore provides a new imaging contrast. DTI is widely used in white matter imaging (95-97), in which the microstructure is characterized by axonal fibers and their surrounding myelin sheath. In general, the water diffusion ability along the axonal fibers is much higher than the water diffusion ability across the axonal fibers and myelin sheaths. Therefore, by measuring the water diffusion ability in different directions pixel-by-pixel, useful information can be obtained, such as the density of the myelin sheath, the integrity of the axonal tracts, and so on. For example, a very important application of DTI is fiber tracking (98), in which the location, orientation, and anisotropy of the axonal tracts are determined and presented by color images. The tractography performed by DTI is able to localize white matter lesions (97).

Diffusion tensor imaging is an extension of diffusion weighted imaging. Diffusion in MRI refers to the position change of water molecules. Diffusion weighted MRI utilize an additional linear gradient to break the homogeneity of the main magnetic field. Since the spin precession frequency is proportional to the magnetic field strength, protons within an imaging voxel begin to precess at different rates, resulting in dispersion of total phase in that voxel. Another linear gradient is then applied in the same direction but with opposite magnitude to rephase the spins in the voxel. However, the rephasing will not be perfect

since some proton spins have diffused to a new position. The imperfect rephasing of proton spins will cause reduction of the measured MRI signal. That is, the addition of a pair of gradient will make the measured signal weighted by diffusion. The diffusion weighted signal for an imaging voxel is:

$$S = S_0 e^{-\gamma^2 G^2 \delta^2 (\Delta - \delta/3) D} = S_0 e^{-bD} \quad \text{[A.1]}$$

In which S_0 is the signal intensity without diffusion weighting, γ is the gyromagnetic ratio, G is the strength of the linear gradient, δ is the length of the gradient, Δ is the time interval between the two gradients, and D is the diffusion constant. If we apply the diffusion weighted gradients in different combinations of phase encoding (x), readout(y), and slice selection (z) directions, then we will be able to calculate the diffusion tensor from:

$$S = S_0 e^{-b \mathbf{n} \mathbf{D} \mathbf{n}^T} \quad \text{[A.2]}$$

In which $\mathbf{D} = \begin{pmatrix} D_{xx} D_{xy} D_{xz} \\ D_{yx} D_{yy} D_{yz} \\ D_{zx} D_{zy} D_{zz} \end{pmatrix}$ is the diffusion tensor. $\mathbf{n}$ is the encoding direction (62).

The three eigenvalues of this diffusion tensor, $\lambda_1, \lambda_2, \lambda_3$, can be derived by matrix diagonalization, and DTI parameters can be calculated from those eigenvalues:

The radial diffusivity: $\lambda_\perp = (\lambda_1 + \lambda_2)/2$ [A.3]

The axial diffusivity: $\lambda_\parallel = \lambda_3$ (λ_3 is the largest eigenvalue) [A.4]

The relative anisotropy: $RA = \dfrac{\sqrt{(\lambda_1 - Tr/3)^2 + (\lambda_2 - Tr/3)^2 + (\lambda_3 - Tr/3)^2}}{Tr/\sqrt{3}}$ [A.5]

The trace: $Tr(D) = \lambda_1 + \lambda_2 + \lambda_3$ [A.6]

The fractional anisotropy: $$FA = \frac{\sqrt{3}\sqrt{(\lambda_1 - Tr/3)^2 + (\lambda_2 - Tr/3)^2 + (\lambda_3 - Tr/3)^2}}{\sqrt{2}\sqrt{\lambda_1^2 + \lambda_2^2 + \lambda_3^2}}$$ [A.7]

Different DTI related studies focus on different DTI parameters. In this dissertation, the radial diffusivity and axial diffusivity are the emphasis of our study, because of their capabilities to reflect the myelin integrity and axon integrity, respectively, as suggested by publications(54-58,64,76,99).

Appendix B: Multiple Exponential T_2 Spectrum Technique

In this appendix, another important magnetic resonance imaging technique, the multiple exponential T_2 spectrum technique, which has showed great potential in white matter imaging, will be introduced and discussed briefly.

The signal we measured in an MRI experiment is a sum of signals from different microstructure components. Though relatively small, the imaging voxel might still contain more than one component in the microstructure scale. These components usually have different T_1 and T_2 properties. Therefore it is possible to differentiate these microstructure components in MRI by investigating the details of relaxation times in a sub-voxel scale. One example is the multiple exponential T_2 (MET2) spectrum technique, which characterizes the multiple components of T_2 in a voxel by fitting the TE dependent signal to a sum of exponential functions.

The MET2 method is particularly interesting for white matter imaging, since it is capable of measuring the myelin contents (63,81,100-103). Figure B.1 (left) shows that the water in the myelin sheath is distinguished from the intra/extracellular water by shorter T_2 values. Figure B.1 (right) shows that if we perform a multiple-echo experiment by using echo times (TE) ranging from a few milliseconds to a few hundreds of milliseconds, we will get a T_2 decay curve for each imaging voxel, and the T_2 spectrum in that voxel can be obtained by fitting the T_2 decay curve to a function which consists of multiple exponential terms. The resulting T_2 spectrum will have two components: a short T_2

component which represents myelin, and a long T_2 component which represents intra/extracellular water. (If the imaging voxel also contains CSF water, then the T_2 spectrum will have another long T_2 component which represents free water). The short component usually has T_2 values ranging from 10 ms to 20 ms, and the long T_2 component usually has T_2 values ranging from 40 ms to 90 ms. The ratio of area under the short T_2 component to the area under the long T_2 component is called myelin water fraction (MWF), which can be used to quantify myelin content.

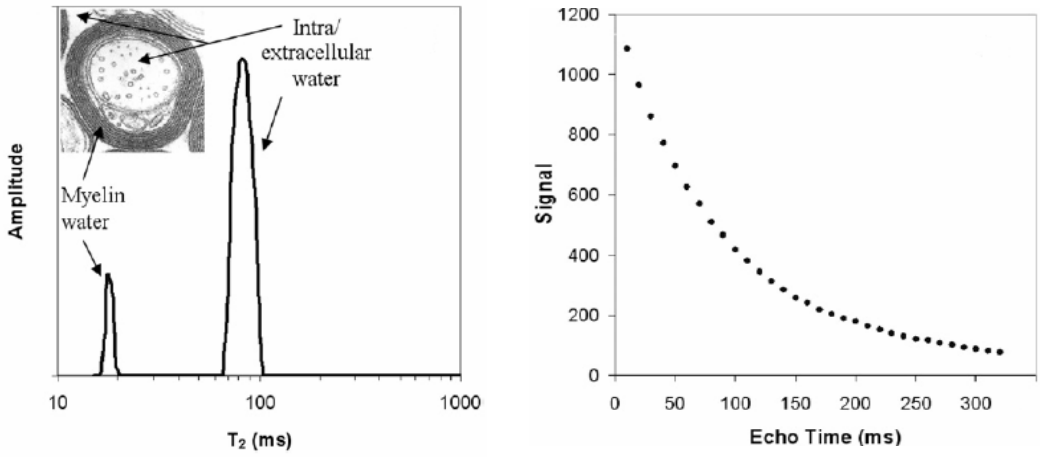

Figure B.1: Left: the myelin water component and Intra/extracellular water component in the T_2 spectrum (104). The picture on the top left is a microscope image of a myelinated axon. Right: the MRI signal in an imaging voxel for different echo times. This TE dependent T_2 decay curve can be used to derive the multiple exponential T_2 spectrum. (Note: this figure is from reference 104)

The MET2 technique is not only sensitive but also very specific to myelin. As an example, figure B.2 indicates that MET2 spectrum is capable of differentiating demyelination and

inflammation (63), which are two pathologies can be found in many white matter diseases and are difficult to differentiate by QMT techniques.

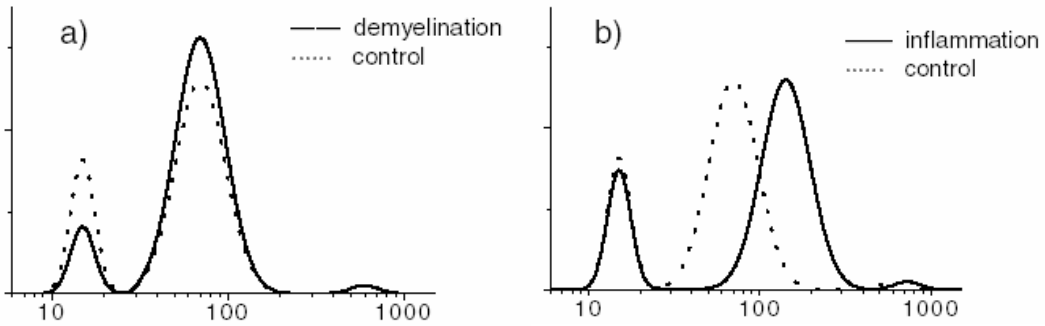

Figure B.2: The T_2 spectrum for demyelination is different from the T_2 spectrum for inflammation. A) In demyelination, the short T_2 component is depressed due to the loss of myelin; the long T_2 component has about the same T_2 since there is no change for the intra/extracellular water. B) In inflammation, the short T_2 component remains the same because there is no myelin loss; the long T_2 component has higher T_2 values because the swelling increases the extracellular volume and generates inflammatory cells. (Note: this figure is from reference 63)

REFERENCES

1. Bloch F, Hansen WW, Packard ME. Nuclear induction. Physics Review 1946;69:127.
2. Purcell EM, Torrey HC, Pound RV. Resonance absorption by nuclear magnetic moments in a solid. Physics Review 1946;69:37.
3. Andrew ER. A historical review of NMR and its clinical applications. Br Med Bull 1984;40(2):115-119.
4. Hahn EL. Spin echoes. Physics Review 1950;80:580.
5. Damadian R. Tumor detection by nuclear magnetic resonance. Science 1971;171(976):1151-1153.
6. Lauterbur PC. Image formation by induced local interactions - examples employing nuclear magnetic resonance. Nature 1973;242(5394):190-191.
7. Mansfield P, Grannell PK. NMR difraction in physics. Journal of Physics C: Solid State Physics 1973;6(22):L422-L426.
8. Mansfield P. Multi planar image formation using NMR spin echoes. Journal of Physics C: Solid State Physics 1977;10(3):L55-L58.
9. Wolff SD, Balaban RS. Magnetization transfer contrast (MTC) and tissue water proton relaxation in vivo. Magn Reson Med 1989;10(1):135-144.
10. Ogawa S, Lee TM, Kay AR, Tank DW. Brain magnetic resonance imaging with contrast dependent on blood oxygenation. Proc Natl Acad Sci U S A 1990;87(24):9868-9872.
11. Dixon WT, Engels H, Castillo M, Sardashti M. Incidental magnetization transfer contrast in standard multislice imaging. Magn Reson Imaging 1990;8(4):417-422.
12. Santyr GE. Magnetization transfer effects in multislice MR imaging. Magn Reson Imaging 1993;11(4):521-532.
13. Bieri O, Scheffler K. On the origin of apparent low tissue signals in balanced SSFP. Magn Reson Med 2006;56(5):1067-1074.
14. Ge Y, Grossman RI, Udupa JK, Babb JS, Kolson DL, McGowan JC. Magnetization transfer ratio histogram analysis of gray matter in relapsing-remitting multiple sclerosis. AJNR Am J Neuroradiol 2001;22(3):470-475.
15. Lizak MJ, Datiles MB, Aletras AH, Kador PF, Balaban RS. MRI of the human eye using magnetization transfer contrast enhancement. Invest Ophthalmol Vis Sci 2000;41(12):3878-3881.
16. Mehta RC, Pike GB, Enzmann DR. Magnetization transfer MR of the normal adult brain. AJNR Am J Neuroradiol 1995;16(10):2085-2091.
17. Wolff SD, Chesnick S, Frank JA, Lim KO, Balaban RS. Magnetization transfer contrast: MR imaging of the knee. Radiology 1991;179(3):623-628.
18. Bozzali M, Franceschi M, Falini A, Pontesilli S, Cercignani M, Magnani G, Scotti G, Comi G, Filippi M. Quantification of tissue damage in AD using diffusion tensor and magnetization transfer MRI. Neurology 2001;57(6):1135-1137.
19. Dousset V, Grossman RI, Ramer KN, Schnall MD, Young LH, Gonzalezscarano F, Lavi E, Cohen JA. Experimental allergic encephalomyelitis and multiple sclerosis - lesion characterization with

magnetization transfer imaging. Radiology 1992;182(2):483-491.
20. Foong J, Symms MR, Barker GJ, Maier M, Woermann FG, Miller DH, Ron MA. Neuropathological abnormalities in schizophrenia: evidence from magnetization transfer imaging. Brain 2001;124(Pt 5):882-892.
21. Pike GB, Hu BS, Glover GH, Enzmann DR. Magnetization transfer time-of-flight magnetic resonance angiography. Magn Reson Med 1992;25(2):372-379.
22. Henkelman RM, Stanisz GJ, Graham SJ. Magnetization transfer in MRI: a review. NMR Biomed 2001;14(2):57-64.
23. Koenig SH. Cholesterol of myelin is the determinant of gray-white contrast in MRI of brain. Magn Reson Med 1991;20(2):285-291.
24. Koenig SH, Brown RD, 3rd, Spiller M, Lundbom N. Relaxometry of brain: why white matter appears bright in MRI. Magn Reson Med 1990;14(3):482-495.
25. Gass A, Barker GJ, Kidd D, Thorpe JW, Macmanus D, Brennan A, Tofts PS, Thompson AJ, McDonald WI, Miller DH. Correlation of magnetization transfer ratio with clinical disability in multiple sclerosis. Annals of Neurology 1994;36(1):62-67.
26. van Buchem MA, McGowan JC, Kolson DL, Polansky M, Grossman RI. Quantitative volumetric magnetization transfer analysis in multiple sclerosis: estimation of macroscopic and microscopic disease burden. Magn Reson Med 1996;36(4):632-636.
27. Gareau PJ, Rutt BK, Karlik SJ, Mitchell JR. Magnetization transfer and multicomponent T2 relaxation measurements with histopathologic correlation in an experimental model of MS. Journal of Magnetic Resonance Imaging 2000;11(6):586-595.
28. Does MD, Beaulieu C, Allen PS, Snyder RE. Multi-component T-1 relaxation and magnetisation transfer in peripheral nerve. Magnetic Resonance Imaging 1998;16(9):1033-1041.
29. Schmierer K, Scaravilli F, Altmann DR, Barker GJ, Miller DH. Magnetization transfer ratio and myelin in postmortem multiple sclerosis brain. Ann Neurol 2004;56(3):407-415.
30. Berry I, Barker GJ, Barkhof F, Campi A, Dousset V, Franconi JM, Gass A, Schreiber W, Miller DH, Tofts PS. A multicenter measurement of magnetization transfer ratio in normal white matter. Journal of Magnetic Resonance Imaging 1999;9(3):441-446.
31. Henkelman RM, Huang XM, Xiang QS, Stanisz GJ, Swanson SD, Bronskill MJ. Quantitative interpretation of magnetization transfer. Magnetic Resonance in Medicine 1993;29(6):759-766.
32. Sled JG, Pike GB. Quantitative imaging of magnetization transfer exchange and relaxation properties in vivo using MRI. Magnetic Resonance in Medicine 2001;46(5):923-931.
33. Tozer D, Ramani A, Barker GJ, Davies GR, Miller DH, Tofts PS. Quantitative magnetization transfer mapping of bound protons in multiple sclerosis. Magnetic Resonance in Medicine 2003;50(1):83-91.
34. Chai JW, Chen C, Chen JH, Lee SK, Yeung HN. Estimation of in vivo proton intrinsic and cross-relaxation rate in human brain. Magn Reson Med 1996;36(1):147-152.
35. Gochberg DF, Gore JC. Quantitative imaging of magnetization transfer using an inversion recovery sequence. Magn Reson Med 2003;49(3):501-505.
36. Gochberg DF, Gore JC. Quantitative magnetization transfer imaging via selective inversion recovery with short repetition times. Magn Reson Med 2007;57(2):437-441.

37. Gochberg DF, Kennan RP, Gore JC. Quantitative studies of magnetization transfer by selective excitation and T-1 recovery. Magnetic Resonance in Medicine 1997;38(2):224-231.
38. Gochberg DF, Kennan RP, Robson MD, Gore JC. Quantitative imaging of magnetization transfer using multiple selective pulses. Magn Reson Med 1999;41(5):1065-1072.
39. Ramani A, Dalton C, Miller DH, Tofts PS, Barker GJ. Precise estimate of fundamental in-vivo MT parameters in human brain in clinically feasible times. Magnetic Resonance Imaging 2002;20(10):721-731.
40. Ropele S, Seifert T, Enzinger C, Fazekas F. Method for quantitative imaging of the macromolecular 1H fraction in tissues. Magn Reson Med 2003;49(5):864-871.
41. Sled JG, Pike GB. Quantitative interpretation of magnetization transfer in spoiled gradient echo MRI sequences. Journal of Magnetic Resonance 2000;145(1):24-36.
42. Yarnykh VL. Pulsed Z-spectroscopic imaging of cross-relaxation parameters in tissues for human MRI: theory and clinical applications. Magn Reson Med 2002;47(5):929-939.
43. Topp S, Adalsteinsson E, Spielman DM. Fast multislice B1 mapping. 1997. p 281.
44. Glover GH, Schneider E. Three-point Dixon technique for true water/fat decomposition with B0 inhomogeneity correction. Magn Reson Med 1991;18(2):371-383.
45. Yarnykh VL, Yuan C. Cross-relaxation imaging reveals detailed anatomy of white matter fiber tracts in the human brain. Neuroimage 2004;23(1):409-424.
46. Tyler DJ, Gowland PA. Rapid quantitation of magnetization transfer using pulsed off-resonance irradiation and echo planar imaging. Magn Reson Med 2005;53(1):103-109.
47. Lee RR, Dagher AP. Low power method for estimating the magnetization transfer bound-pool macromolecular fraction. J Magn Reson Imaging 1997;7(5):913-917.
48. Graham SJ, Henkelman RM. Pulsed magnetization transfer imaging: evaluation of technique. Radiology 1999;212(3):903-910.
49. Haacke EM, Brown RW, Thompson MR, Venkateson R. Magnetic Resonance Imaging: Physical Principles and Sequnce Design: John Wiley & Sons, Inc.; 1999.
50. Sled JG, Levesque I, Santos AC, Francis SJ, Narayanan S, Brass SD, Arnold DL, Pike GB. Regional variations in normal brain shown by quantitative magnetization transfer imaging. Magn Reson Med 2004;51(2):299-303.
51. Horsfield MA, Lai M, Webb SL, Barker GJ, Tofts PS, Turner R, Rudge P, Miller DH. Apparent diffusion coefficients in benign and secondary progressive multiple sclerosis by nuclear magnetic resonance. Magnetic Resonance in Medicine 1996;36(3):393-400.
52. Horsfield MA, Jones DK. Applications of diffusion-weighted and diffusion tensor MRI to white matter diseases - a review. Nmr in Biomedicine 2002;15(7-8):570-577.
53. Filippi M, Cercignani M, Inglese M, Horsfield MA, Comi G. Diffusion tensor magnetic resonance imaging in multiple sclerosis. Neurology 2001;56(3):304-311.
54. Sun SW, Liang HF, Le TQ, Armstrong RC, Cross AH, Song SK. Differential sensitivity of in vivo and ex vivo diffusion tensor imaging to evolving optic nerve injury in mice with retinal ischemia. Neuroimage 2006;32(3):1195-1204.
55. Song SK, Yoshino J, Le TQ, Lin SJ, Sun SW, Cross AH, Armstrong RC. Demyelination increases radial diffusivity in corpus callosum of mouse brain. Neuroimage 2005;26(1):132-140.

56. Song SK, Sun SW, Ramsbottom MJ, Chang C, Russell J, Cross AH. Dysmyelination revealed through MRI as increased radial (but unchanged axial) diffusion of water. Neuroimage 2002;17(3):1429-1436.
57. Kim JH, Budde MD, Liang HF, Klein RS, Russell JH, Cross AH, Song SK. Detecting axon damage in spinal cord from a mouse model of multiple sclerosis. Neurobiol Dis 2006;21(3):626-632.
58. Song SK, Sun SW, Ju WK, Lin SJ, Cross AH, Neufeld AH. Diffusion tensor imaging detects and differentiates axon and myelin degeneration in mouse optic nerve after retinal ischemia. Neuroimage 2003;20(3):1714-1722.
59. Privat A, Jacque C, Bourre JM, Dupouey P, Baumann N. Absence of the major dense line in myelin of the mutant mouse shiverer. Neuroscience Letters 1979;12(1):107-112.
60. Inoue Y, Nakamura R, Mikoshiba K, Tsukada Y. Fine structure of the central myelin sheath in the myelin deficient mutant shiverer mouse, with special reference to the pattern of myelin formation by oligodendroglia. Brain Research 1981;219(1):85-94.
61. Griffiths I, Klugmann M, Anderson T, Yool D, Thomson C, Schwab MH, Schneider A, Zimmermann F, McCulloch M, Nadon N, Nave KA. Axonal swellings and degeneration in mice lacking the major proteolipid of myelin. Science 1998;280(5369):1610-1613.
62. Basser PJ, Pierpaoli C. Microstructural and physiological features of tissues elucidated by quantitative-diffusion-tensor MRI. J Magn Reson B 1996;111(3):209-219.
63. Odrobina EE, Lam TY, Pun T, Midha R, Stanisz GJ. MR properties of excised neural tissue following experimentally induced demyelination. NMR Biomed 2005;18(5):277-284.
64. Sun SW, Neil JJ, Song SK. Relative indices of water diffusion anisotropy are equivalent in live and formalin-fixed mouse brains. Magnetic Resonance in Medicine 2003;50(4):743-748.
65. Purea A, Webb AG. Reversible and irreversible effects of chemical fixation on the NMR properties of single cells. Magn Reson Med 2006;56(4):927-931.
66. Tovi M, Ericsson A. Measurements of T1 and T2 over time in formalin-fixed human whole-brain specimens. Acta Radiol 1992;33(5):400-404.
67. Merkler D, Boretius S, Stadelmann C, Ernsting T, Michaelis T, Frahm J, Bruck W. Multicontrast MRI of remyelination in the central nervous system. NMR Biomed 2005;18(6):395-403.
68. Tozer DJ, Davies GR, Altmann DR, Miller DH, Tofts PS. Correlation of apparent myelin measures obtained in multiple sclerosis patients and controls from magnetization transfer and multicompartmental T-2 analysis. Magnetic Resonance in Medicine 2005;53(6):1415-1422.
69. Stanisz GJ, Webb S, Munro CA, Pun T, Midha R. MR properties of excised neural tissue following experimentally induced inflammation. Magnetic Resonance in Medicine 2004;51(3):473-479.
70. Mottershead JP, Schmierer K, Clemence M, Thornton JS, Scaravilli F, Barker GJ, Tofts PS, Newcombe J, Cuzner ML, Ordidge RJ, McDonald WI, Miller DH. High field MRI correlates of myelin content and axonal density in multiple sclerosis--a post-mortem study of the spinal cord. J Neurol 2003;250(11):1293-1301.
71. Blezer EL, Bauer J, Brok HP, Nicolay K, t Hart BA. Quantitative MRI-pathology correlations of brain white matter lesions developing in a non-human primate model of multiple sclerosis. NMR Biomed 2007;20(2):90-103.

72. Hickman SJ, Toosy AT, Jones SJ, Altmann DR, Miszkiel KA, MacManus DG, Barker GJ, Plant GT, Thompson AJ, Miller DH. Serial magnetization transfer imaging in acute optic neuritis. Brain 2004;127(Pt 3):692-700.
73. Edzes HT, Samulski ET. Measurement of cross-relaxation effects in proton NMR spin-lattice relaxation of water in biological systems - hydrated collagen and muscle. Journal of Magnetic Resonance 1978;31(2):207-229.
74. Miller DH, Grossman RI, Reingold SC, McFarland HF. The role of magnetic resonance techniques in understanding and managing multiple sclerosis. Brain 1998;121:3-24.
75. Trapp BD, Bo L, Mork S, Chang A. Pathogenesis of tissue injury in MS lesions. J Neuroimmunol 1999;98(1):49-56.
76. Ou X, Sun SW, Liang HF, Gochberg DF, Song SK. QMT estimated pool size ratio and DTI derived radial diffusivity reflect the integrity of myelin sheath in mice. 2007.
77. Narayanan S, Francis SJ, Sled JG, Santos AC, Antel S, Levesque I, Brass S, Lapierre Y, Sappey-Marinier D, Pike GB, Arnold DL. Axonal injury in the cerebral normal-appearing white matter of patients with multiple sclerosis is related to concurrent demyelination in lesions but not to concurrent demyelination in normal-appearing white matter. Neuroimage 2006;29(2):637-642.
78. Stanisz GJ, Henkelman RM. Diffusional anisotropy of T2 components in bovine optic nerve. Magn Reson Med 1998;40(3):405-410.
79. Peled S, Cory DG, Raymond SA, Kirschner DA, Jolesz FA. Water diffusion, T(2), and compartmentation in frog sciatic nerve. Magn Reson Med 1999;42(5):911-918.
80. Andrews TJ, Osborne MT, Does MD. Diffusion of myelin water. Magn Reson Med 2006;56(2):381-385.
81. Stanisz GJ, Kecojevic A, Bronskill MJ, Henkelman RM. Characterizing white matter with magnetization transfer and T-2. Magnetic Resonance in Medicine 1999;42(6):1128-1136.
82. Bjarnason TA, Vavasour IM, Chia CL, MacKay AL. Characterization of the NMR behavior of white matter in bovine brain. Magn Reson Med 2005;54(5):1072-1081.
83. Lucchinetti C, Bruck W, Parisi J, Scheithauer B, Rodriguez M, Lassmann H. Heterogeneity of multiple sclerosis lesions: implications for the pathogenesis of demyelination. Ann Neurol 2000;47(6):707-717.
84. Noseworthy JH, Lucchinetti C, Rodriguez M, Weinshenker BG. Multiple sclerosis. N Engl J Med 2000;343(13):938-952.
85. Owens T, Sriram S. The immunology of multiple sclerosis and its animal model, experimental allergic encephalomyelitis. Neurol Clin 1995;13(1):51-73.
86. Floris S, Blezer EL, Schreibelt G, Dopp E, van der Pol SM, Schadee-Eestermans IL, Nicolay K, Dijkstra CD, de Vries HE. Blood-brain barrier permeability and monocyte infiltration in experimental allergic encephalomyelitis: a quantitative MRI study. Brain 2004;127(Pt 3):616-627.
87. Morrissey SP, Stodal H, Zettl U, Simonis C, Jung S, Kiefer R, Lassmann H, Hartung HP, Haase A, Toyka KV. In vivo MRI and its histological correlates in acute adoptive transfer experimental allergic encephalomyelitis. Quantification of inflammation and oedema. Brain 1996;119 (Pt 1):239-248.
88. Confavreux C, Vukusic S, Moreau T, Adeleine P. Relapses and progression of disability in

multiple sclerosis. N Engl J Med 2000;343(20):1430-1438.
89. Maggs FG, Palace J. The pathogenesis of multiple sclerosis: is it really a primary inflammatory process? Mult Scler 2004;10(3):326-329.
90. Rudick RA, Cutter GR, Baier M, Weinstock-Guttman B, Mass MK, Fisher E, Miller DM, Sandrock AW. Estimating long-term effects of disease-modifying drug therapy in multiple sclerosis patients. Mult Scler 2005;11(6):626-634.
91. Duncan JR, Cock ML, Suzuki K, Scheerlinck JP, Harding R, Rees SM. Chronic endotoxin exposure causes brain injury in the ovine fetus in the absence of hypoxemia. J Soc Gynecol Investig 2006;13(2):87-96.
92. Lehnardt S, Lachance C, Patrizi S, Lefebvre S, Follett PL, Jensen FE, Rosenberg PA, Volpe JJ, Vartanian T. The toll-like receptor TLR4 is necessary for lipopolysaccharide-induced oligodendrocyte injury in the CNS. J Neurosci 2002;22(7):2478-2486.
93. Lehnardt S, Massillon L, Follett P, Jensen FE, Ratan R, Rosenberg PA, Volpe JJ, Vartanian T. Activation of innate immunity in the CNS triggers neurodegeneration through a Toll-like receptor 4-dependent pathway. Proc Natl Acad Sci U S A 2003;100(14):8514-8519.
94. Felts PA, Woolston AM, Fernando HB, Asquith S, Gregson NA, Mizzi OJ, Smith KJ. Inflammation and primary demyelination induced by the intraspinal injection of lipopolysaccharide. Brain 2005;128(Pt 7):1649-1666.
95. Beaulieu C. The basis of anisotropic water diffusion in the nervous system - a technical review. NMR Biomed 2002;15(7-8):435-455.
96. Le Bihan D, Mangin JF, Poupon C, Clark CA, Pappata S, Molko N, Chabriat H. Diffusion tensor imaging: concepts and applications. J Magn Reson Imaging 2001;13(4):534-546.
97. Werring DJ, Clark CA, Barker GJ, Thompson AJ, Miller DH. Diffusion tensor imaging of lesions and normal-appearing white matter in multiple sclerosis. Neurology 1999;52(8):1626-1632.
98. Basser PJ, Pajevic S, Pierpaoli C, Duda J, Aldroubi A. In vivo fiber tractography using DT-MRI data. Magn Reson Med 2000;44(4):625-632.
99. Ou X, Sun SW, Gochberg DF, Song SK. QMT is specifically sensitive to myelin and not axonal injury in optic nerve from mice undergoing transient retinal ischemia. 2007.
100. Does MD, Snyder RE. Multiexponential T-2 relaxation in degenerating peripheral nerve. Magnetic Resonance in Medicine 1996;35(2):207-213.
101. Laule C, Vavasour IM, Moore GRW, Oger J, Li DKB, Paty DW, MacKay AL. Water content and myelin water fraction in multiple sclerosis - A T-2 relaxation study. Journal of Neurology 2004;251(3):284-293.
102. Mackay A, Whittall K, Adler J, Li D, Paty D, Graeb D. In-vivo visualization of myelin water in brain by magnetic resonance. Magnetic Resonance in Medicine 1994;31(6):673-677.
103. Whittall KP, MacKay AL, Graeb DA, Nugent RA, Li DK, Paty DW. In vivo measurement of T2 distributions and water contents in normal human brain. Magn Reson Med 1997;37(1):34-43.
104. Laule C, Vavasour IM, Kolind SH, Li DK, Traboulsee TL, Moore GR, MacKay AL. Magnetic resonance imaging of myelin. Neurotherapeutics 2007;4(3):460-484.